Survey of Deep Learning and Physics-Based Approaches in Computational Wave Imaging

Youzuo Lin, Shihang Feng, James Theiler, Yinpeng Chen, Umberto Villa, Jing Rao, John Greenhall, Cristian Pantea, Mark A. Anastasio, and Brendt Wohlberg

arXiv:2410.08329v2 [cs.LG] 24 Sep 2025

***Abstract*—Computational wave imaging (CWI) extracts hidden structure and physical properties of a volume of material by analyzing wave signals that traverse that volume. Applications include seismic exploration of the Earth's subsurface, acoustic imaging and non-destructive testing in material science, and ultrasound computed tomography in medicine. Current approaches for solving CWI problems can be divided into two categories: those rooted in traditional physics, and those based on deep learning. Physics-based methods stand out for their ability to provide high-resolution and quantitatively accurate estimates of acoustic properties within the medium. However, they can be computationally intensive and are susceptible to ill-posedness and nonconvexity typical of CWI problems. Machine learning-based computational methods have recently emerged, offering a different perspective to address these challenges. Diverse scientific communities have independently pursued the integration of deep learning in CWI. This review discusses how contemporary scientific machine-learning (ML) techniques, and deep neural networks in particular, have been developed to enhance and integrate with traditional physics-based methods for solving CWI problems. We present a structured framework that consolidates existing research spanning multiple domains, including computational imaging, wave physics, and data science. This study concludes with important lessons learned from existing ML-based methods and identifies technical hurdles and emerging trends through a systematic analysis of the extensive literature on this topic.**

***Index Terms*—Computational Wave Imaging, Deep Learning, Wave Physics, Full Waveform Inversion, Ultrasound Computed Tomography, Non-Destructive Testing**

I. Introduction

Waves are ubiquitous in our world; prominent examples include the transmission of sound through the atmosphere, the motion of water on the surface of the ocean, and the traveling of seismic vibrations through the earth. Well-established physical models provide detailed descriptions of how these waves are influenced by the materials through which they propagate. Computational wave imaging (CWI) aims to invert these models, and to extract detailed information about these materials, including properties such as density and bulk modulus, using measurements of wave signals (amplitudes, phases, and travel-times) taken on the outer boundaries of these spaces.

Y. Lin and S. Feng are with the University of North Carolina at Chapel Hill, Chapel Hill, NC 27599, USA. (E-mail: **yzlin@unc.edu**).

J. Theiler, J. Greenhall, C. Pantea, and B. Wohlberg are with Los Alamos National Laboratory, Los Alamos, NM, 87545, USA.

Y. Chen is with Google DeepMind, Seattle, WA, 98103, USA.

U. Villa is with the University of Texas at Austin, Austin, TX, 78712, USA.

J. Rao is with University of New South Wales, Canberra, ACT 2600, Australia.

M. Anastasio is with University of Illinois Urbana Champaign, Champaign, IL, 61820, USA.

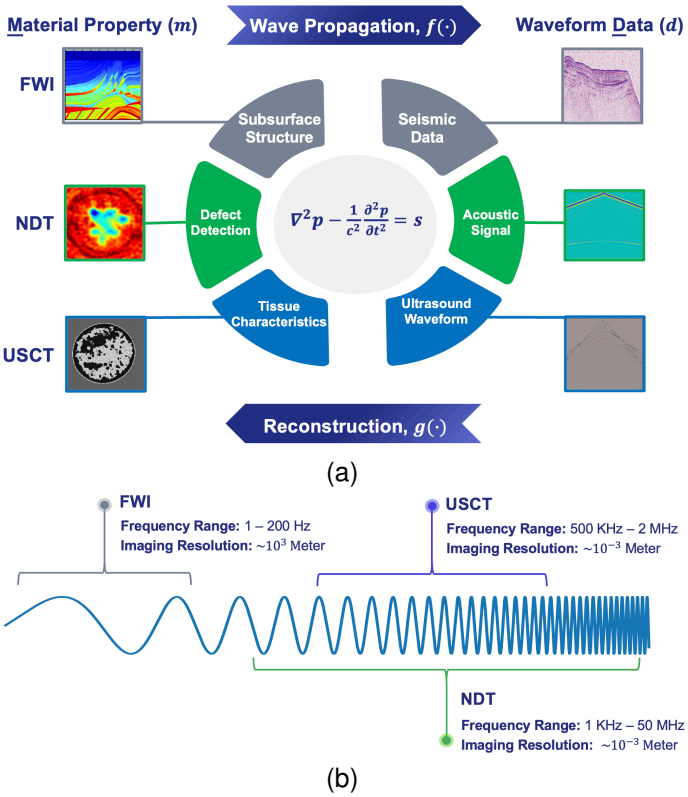


Fig. 1. An illustration of (a) CWI problems covered in this paper and (b) specific CWI applications differentiated by their source spectrum. The common feature is the forward wave equation, and the common goal is the reconstruction of physical properties from wave measurements. We will discuss various approaches for achieving this reconstruction in the context of three application areas: seismic Full-Waveform Inversion (FWI), acoustic and industrial ultrasound including Non-Destructive Testing (NDT), and medical Ultrasound Computed Tomography (USCT).

This review will focus on the three distinct application areas shown in Fig. IV-B3: seismic Full-Waveform Inversion (FWI), acoustic and industrial ultrasound imaging (encompassing Non-Destructive Testing, or NDT), and medical Ultrasound Computed Tomography (USCT). Despite the differences in the frequency of the propagating wave (Fig. 1b), and the scale of the imaging volumes, these applications share several common underlying physical processes. Each involves both a forward wave propagation model and an inverse imaging or reconstruction problem, as depicted in Fig. IV-B3. "Wave Propagation" is described by the governing wave equation, and is generally the more straightforward problem; it often requires the use of numerical methods to simulate waves in

complex media, as analytical solutions to wave equations are only attainable in idealized conditions. Conversely, the more challenging "reconstruction" task is to estimate the properties of the intervening medium based on measurements (*e.g.*, of acoustic pressure) taken outside the region of interest. We have observed the great potential of machine learning (ML) to enhance the accuracy and efficiency of solutions to CWI problem in various fields, such as subsurface energy applications [1]–[3], material characterization [4]–[6], and medical ultrasound imaging [7]–[9]. Such improvements to CWI can be impactful, as these techniques are not only tools for problem-solving but also catalysts for scientific discovery and engineering innovation. Indeed, they can even lead to the discovery of new physical insights [10]. Furthermore, we have found that integrating physics into ML models contributes to improved model generalization and robustness, and makes more effective use of limited training data [11], [12]. Our objective is to provide an overview of data science and ML techniques used for CWI challenges, and to underscore the significant advantages of incorporating the fundamental underlying physics into the design of ML models.

A common set of computational challenges emerges from the shared foundation of wave physics across diverse imaging problems. One prominent challenge is the pervasive ill-posedness encountered in CWI problems, arising from the inherently limited data coverage; *i.e.*, attempting to characterize a 3D volume with measurements confined to its 2D surface. To mitigate ill-posedness, conventional physics-based methods introduce techniques such as regularization, but selecting an appropriate regularization term can be a non-trivial task. Additionally, numerical optimization methods for solving CWI problems have their own difficulties: (1) the accuracy of the solution can be highly contingent on the initial guess; and (2) the computational cost can be prohibitive. Traditional physics-based CWI solvers often require many evaluations of the forward model before achieving convergence, presenting substantial computational burden. Furthermore, cycle-skipping is a well-documented issue in CWI [13] that occurs when the timing of the modeled waveform (predicted by the inverted solution) deviates by more than half a cycle from that of the observed waveform. The goal of this paper is to provide a review of contemporary methods in CWI, with a focus on common challenges and methods. In particular, we explore both the opportunities and difficulties inherent in the application of ML to enhance and expedite the solution of CWI problems.

ML has significantly influenced the evolution of CWI techniques. This synergy is particularly evident in the emerging trend of integrating fundamental physics principles with ML algorithms to advance CWI methods. Here we have compiled over 200 papers from three CWI communities, and have observed a clear and consistent upward trend in the volume of publications dedicated to ML within this domain (as shown in Fig. 15 in the Appendix). Furthermore, each of these scientific communities has produced high-quality review papers, a selection of which is presented in Table B of the Appendix. These reviews can be categorized into three primary groups: physics-based methods, machine-learning approaches, and hybrid methods that integrate data-driven techniques with fundamental physics principles.

II. Governing Wave Physics

Wave-based imaging relies on partial differential equations (PDEs) to describe the propagation of mechanical waves through physical media. The choice of wave model varies across application domains and is dictated by the properties of the medium and the nature of the wave. In Earth sciences, the acoustic wave equation is commonly used in seismic exploration [14], while elastic models are essential for simulating earthquake processes [15]. In medical imaging, acoustic wave models are standard for ultrasound computed tomography [16], with elastic or viscoelastic models employed in applications such as elastography and transcranial ultrasound [17]. In nondestructive testing (NDT), both acoustic and elastic wave equations are used, depending on the geometry and material complexity of the structures being interrogated [6].

A. Acoustic Wave Equation

The acoustic wave equation models the propagation of compressional (P) waves through fluid-like media, where shear stresses are negligible. It is widely used in seismic exploration [14], ultrasound imaging [16], and NDT [6] scenarios involving air or water. This model also serves as the default choice in many learning-based CWI frameworks due to its mathematical simplicity and computational efficiency.

The constant density form of the acoustic wave equation is:

$$\nabla^2 p(\boldsymbol{r},t) - \frac{1}{V_P^2(\boldsymbol{r})}\frac{\partial^2 p(\boldsymbol{r},t)}{\partial t^2} = s(\boldsymbol{r},t), \tag{1}$$

where $p(\boldsymbol{r},t)$ denotes the pressure field, $V_P(\boldsymbol{r})$ is the P-wave velocity, $\boldsymbol{r}$ represents spatial coordinates, and $s(\boldsymbol{r},t)$ specifies the spatiotemporal source. This form assumes uniform density, simplifying numerical treatment but neglecting key physical effects in heterogeneous media.

The variable-density acoustic wave equation introduces spatial variability in density $\rho(\boldsymbol{r})$ [18], [19]:

$$\nabla \cdot \left(\frac{1}{\rho(\boldsymbol{r})}\nabla p\right) - \frac{1}{\rho(\boldsymbol{r})V_P^2(\boldsymbol{r})}\frac{\partial^2 p}{\partial t^2} = s(\boldsymbol{r},t). \tag{2}$$

This model offers a more accurate description of wave propagation in complex environments such as sedimentary basins or soft tissues. While computationally more demanding, it remains widely used due to its flexibility and compatibility with both inversion and learning-based algorithms.

Overall, the acoustic wave equation plays a foundational role in CWI. It supports synthetic data generation, enables physics-informed learning, and offers a physically grounded framework for designing loss functions and priors in modern deep learning pipelines. Unless otherwise noted, the remainder of this paper adopts the constant density formulation without loss of generality.

B. Extensions to Complex Wave Physics

Although the acoustic wave equation provides a foundational model widely used across many CWI applications, real-world propagation environments often involve more complex physical phenomena. These complexities arise from material anisotropy, energy dissipation, and the presence of both compressional and shear wave modes. To address these effects, various extensions to the acoustic model have been developed and are employed in geophysics, medical imaging, and non-destructive testing [20]–[22].

Elastic Wave Equation. In solid media, wave propagation involves both compressional (P) and shear (S) waves. The elastic wave equation models this behavior by jointly solving for velocity and stress tensors, using Lamé parameters to describe the materials elastic properties. It is essential in applications such as earthquake seismology and materials characterization [15].

Viscoacoustic Wave Equation. To model attenuation in lossy or dissipative media, viscoacoustic formulations introduce memory variables and relaxation mechanisms that simulate the frequency-dependent absorption of wave energy [23]. These models are critical in biomedical and seismic contexts where wave dispersion and amplitude decay significantly impact image resolution and accuracy.

Anisotropic Wave Equation. Many materials exhibit directionally dependent wave speeds due to internal structure or stress fields. Anisotropic wave equations, including simplified pseudo-acoustic forms such as Vertical Transverse Isotropy (VTI), enable modeling of wave propagation in these directionally varying environments [21], [24]. Such models are widely used in layered earth models and anisotropic composites.

Other Variants. Additional extensions include poroelastic models for fluid-solid interactions and coupled elastic-acoustic systems [25]. These formulations offer greater fidelity but also introduce increased complexity in both numerical simulation and learning-based inversion.

While this review focuses on the acoustic wave equation for clarity and broad applicability, many of the learning methods described in the following sections can be extended to handle these more complex wave physics. Readers are referred to Appendix A for detailed mathematical formulations of these advanced wave equations.

III. Computational Wave Imaging and Physics-based Methods

A. Forward Modeling

Physics-based methods are broadly implemented in various CWI applications. Generally speaking, these methods are computationally expensive, and require careful regularization. However, they tend to be more generalizable and robust to measurements contaminated with noise than data-driven methods. The forward modeling of CWI can be written

$$\boldsymbol{d} = f(\boldsymbol{m}) + \boldsymbol{\eta}\,, \tag{3}$$

where $\boldsymbol{d}$ represents the observed data, $f(\cdot)$ is the forward model, $\boldsymbol{m}$ represents the material properties we wish to infer, and η represents measurement noise.

Particularly for acoustic wave modeling, which is the focus of this manuscript, the observed data $\boldsymbol{d}$ typically consists of time traces of the pressure wavefield $p(\boldsymbol{r}, t)$ recorded at discrete receiver locations $\boldsymbol{r}$, while $\boldsymbol{m}$ corresponds to the spatially varying velocity map $V_P(\boldsymbol{r})$. In many practical settings, the forward model also depends on additional physical or algorithmic nuisance parametersquantities that influence the data but are not the primary inversion targets. Common examples include the source location, source time function, boundary conditions, or sensor calibration parameters. While not the primary focus of CWI, these factors must be carefully handled to ensure accurate reconstruction.

A variety of numerical techniques have been employed for forward modeling. Finite difference methods [26], [27], which discretize the domain into regular grids and approximate derivatives using difference formulas, work well for simple geometries. Staggered-grid finite difference methods [28]–[30] can enhance numerical stability and reduce numerical dispersion. Finite element methods [31]–[33] are well suited to irregular geometries and complex material properties. Pseudospectral methods [34]–[38] have proven effective for problems that require high precision in spatial derivatives. Finally, spectral element methods [39]–[42] combine the advantages of spectral methods and finite elements, offering both high accuracy and flexibility in complex scenarios.

B. Physics-based Wave Imaging

Computatioanl wave imaging aims to estimate the material property $\boldsymbol{m}$ from the observed data $\boldsymbol{d}$; that is, it aims to find an inversion operator g so that $\widehat{\boldsymbol{m}} = g(\boldsymbol{d})$ approximates the actual property. A minimal requirement for this approximate model is that the forward propagation based on this model should approximate the observed data; that is, $f(\widehat{\boldsymbol{m}}) \approx \boldsymbol{d}$. This implies that $f(g(\boldsymbol{d})) \approx \boldsymbol{d}$ and for this reason, g is informally referred to as the *inverse* of f. But directly inverting f is generally infeasible due to the ill-posed nature of CWI. To address these challenges, CWI is often formulated as the solution to an optimization problem. The unknown material properties are then estimated as the minimizers $\widehat{\boldsymbol{m}}$ of a penalized nonlinear least squares problem and can be written

$$\widehat{\boldsymbol{m}} = \underset{\boldsymbol{m}}{\operatorname{argmin}} \left[\|\boldsymbol{d} - f(\boldsymbol{m})\|_2^2 + \gamma\, r(\boldsymbol{m}) \right], \tag{4}$$

where the first term enforces data fidelity and the second term, weighted by γ, incorporates prior information with a regularization function $r(\boldsymbol{m})$, which encodes assumptions about the underlying medium [43]–[46]. Classical choices include Tikhonov regularization, $r(\boldsymbol{m}) = \|H\boldsymbol{m}\|_2^2$, which promotes smoothness via a high-pass filter H, and total variation (TV) regularization, $r(\boldsymbol{m}) = \|\nabla \boldsymbol{m}\|_1$, which encourages piecewise smooth structures and preserves edges [47].

Beyond these, many advanced regularization strategies have been developed to better adapt to specific medium structures and improve reconstruction quality. For instance, modified TV formulations have been used to enhance the delineation of high-contrast interfaces [45]; adaptive schemes such as the proximal NewtonADMM framework with pretrained denoisers allow dynamic balancing between smooth and blocky

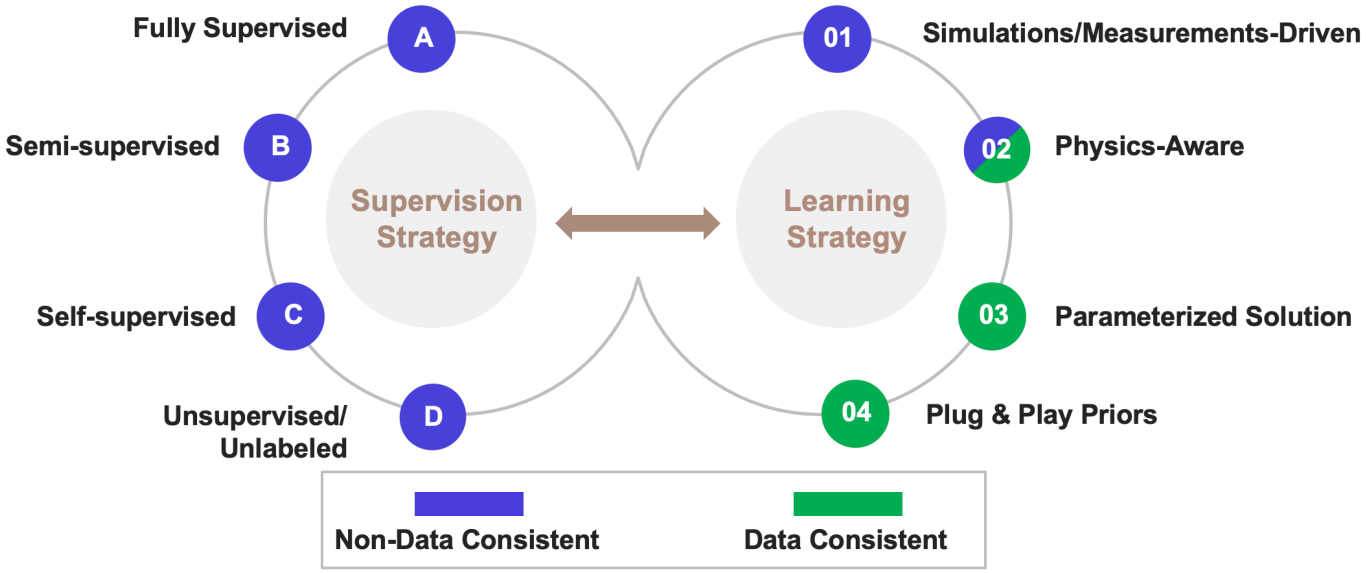


Fig. 2. A taxonomy of ML methods for CWI, based on two categorizations. Under supervision strategy, we distinguish fully supervised, semi-supervised, self-supervised, and unsupervised/unlabeled. Under learning strategy, we categorize methods as simulations/measurements-driven, physics-aware, parameterized solutions, and plug-and-play priors. We further differentiate these methods by "Data Consistent" (in green) and "Non-Data Consistent" (in blue) based on their adherence to data fidelity consistency. In Appendix B, we offer visualizations illustrating trends in ML methods for CWI, along with a breakdown categorizing over 200 papers into eight method groups. This section also includes a curated table highlighting selected papers from each category.

regions [48]; and constraint-based approaches like salt flooding techniques have proven effective in complex subsurface environments [49]. Recently, hybrid strategies that decompose the model into smooth and blocky components, such as the adaptive TikhonovTV regularization method [50], demonstrated strong robustness across varying realistic settings.

IV. Deep Learning for Computational Wave Imaging Problems

In this section, we discuss ML-based methods for CWI, categorizing them by supervision and learning strategies as illustrated in Fig. 2. Supervision strategy pertains to the use of labels and data, while learning strategy involves integrating physics into ML model design. Techniques are typically classified by supervision strategy in computer vision and ML, and by learning strategy in computational imaging and physics. We present these categorizations side-by-side for a comprehensive understanding across different communities. Additionally, we classify methods based on data fidelity consistency: data-consistent methods ensure model outputs closely align with actual measurements, enhancing trustworthiness and generalizability, while non-data consistent methods may produce quantitatively incorrect yet realistic estimates.

A. Machine Learning Methods by Supervision Strategy

Here, we categorize ML methods for solving CWI problems by supervision strategy as shown in Fig. 2. In what follows, *samples* are instances of waveform data $\boldsymbol{d}$, and *labels* are the corresponding models of the medium $\boldsymbol{m}$.

- **Fully Supervised.** Both samples and associated labels are available, and all labels are used to supervise the training of the models.

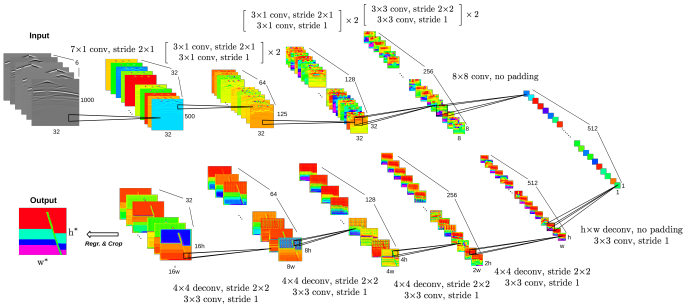


Fig. 3. Network architecture of InversionNet, a fully-supervised method [51].

- **Semi-Supervised.** Some labeled samples are available, but there are additional unlabeled samples as well. Models are trained using both labeled and unlabeled samples.
- **Self-Supervised.** Labels are not provided, but label-like supervision signals (pseudo labels) are generated from the samples.
- **Unsupervised/Unlabeled.** Training is performed using only input samples, without explicit labels. This category includes both data-driven methods that learn latent structure (*e.g.*, autoencoders, contrastive learning), as well as learning approaches that infer velocity parameters by enforcing consistency with simulated or observed measurements.

1) Fully Supervised Methods: Fully supervised methods are among the most straightforward and widely used approaches in solving CWI problems [1], [51]–[53]. The basic idea is to obtain a large training set $\boldsymbol{\Phi}$ of pairs $(\boldsymbol{d}_i, \boldsymbol{m}_i)$ and to use that data to train a deep neural network that instantiates the inversion operator $g_\theta(\cdot)$. Here, we employ the "InversionNet" method, developed by [51], as an example to illustrate how to

solve CWI problems using a fully supervised learning strategy. Mathematically, InversionNet can be expressed as

$$\widehat{\boldsymbol{m}} = g_{\boldsymbol{\theta}^*}(\boldsymbol{d}) \qquad (5)$$
$$\text{where } \boldsymbol{\theta}^* = \arg\min_{\boldsymbol{\theta}} \sum_{(\boldsymbol{d}_i, \boldsymbol{m}_i)\in\boldsymbol{\Phi}} \mathcal{L}(g_{\boldsymbol{\theta}}(\boldsymbol{d}_i), \boldsymbol{m}_i)\,,$$

where $\boldsymbol{m}$ is the predicted velocity map, $\boldsymbol{\theta}$ represents the trainable weights in the inversion network, $g_{\boldsymbol{\theta}}(\cdot)$ corresponds to the network itself, $\boldsymbol{\Phi}$ is the training dataset with paired samples of $(\boldsymbol{d}_i, \boldsymbol{m}_i)$, and the loss function $\mathcal{L}(\cdot,\cdot)$ is commonly defined in terms of the ℓ_1 or ℓ_2 norm, comparing the difference of $\boldsymbol{m}_i$ with $\widehat{\boldsymbol{m}}$. As shown in Fig. 3, InversionNet utilizes an encoder-decoder structure, processing both input waveform data and output velocity maps as images. The labeled samples (*i.e.*, $\boldsymbol{d}, \boldsymbol{m}$ pairs) are typically synthetically generated to reflect realistic medium profiles, often numbering in the tens of thousands. Various methods, such as the geostatistical approaches detailed by [54], are used to create geologically significant $\boldsymbol{m}_i$-images for seismic inversion. Each waveform $\boldsymbol{d}$ is computed using the forward operator f, as outlined in Eq. (3). While training requires a large number of labeled samples, a fully trained network can quickly evaluate the inverse operator $g_{\boldsymbol{\theta}^*}(\cdot)$, an advantage in monitoring scenarios requiring frequent assessments. However, inference on out-of-distribution data remains challenging, and the network tends to generate solutions that closely mirror the training data, thus limiting generalization.

In addition to InversionNet, several other works build on the concept of fully supervised learning strategies, employing various backbone networks. [1] utilizes fully connected networks, while [53] develops an encoder-decoder network structure similar to InversionNet to enhance acoustic imaging. [52] implements a specific type of encoder-decoder network known as U-net [55], which includes skip connections linking the encoder and decoder paths, to facilitate learning. The choice of backbone network architecture can significantly impact the network's properties. Generally, convolution-based networks are more parameter-efficient due to weight sharing, making them particularly suitable for processing high-dimensional waveform data and velocity maps while reducing the size of the required training dataset. In contrast, fully connected networks, due to their high parameter count, may become impractical for large-scale applications.

2) Semi-supervised Methods: Fully supervised learning provides a direct means to apply machine learning to CWI, but its utility is limited by the scarcity of labeled data. Acquiring velocity models as labels can be costly and time-consuming, whereas collecting unlabeled waveform data is typically much more feasible. For example, in seismic FWI, distributed acoustic sensing (DAS) [57] allows efficient acquisition of large volumes of unlabeled seismic data. To address the imbalance between labeled and unlabeled data availability, various semi-supervised learning approaches have been developed [56], [58]–[60].

Among these, [56] proposes a CycleGAN-based SSL framework designed to extrapolate missing low-frequency content in field seismic data. The method is trained using unpaired data

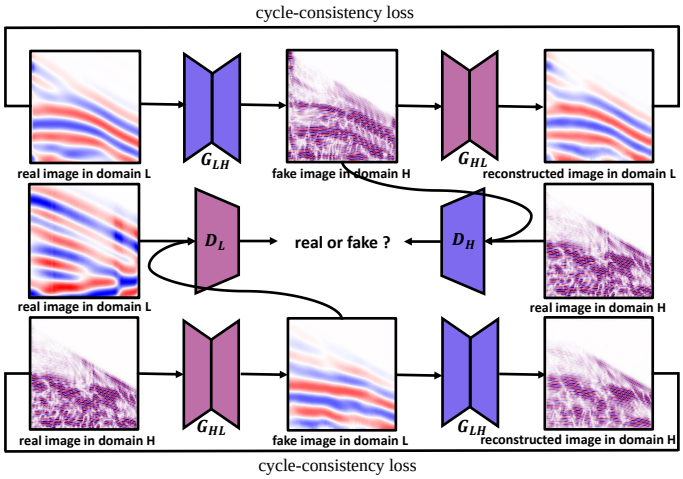


Fig. 4. Schematic illustration of semi-supervised learning strategies in CWI. In the CycleGAN-based low-frequency extrapolation method [56], the network learns to translate between unpaired high-frequency field data and synthetic low-frequency data using adversarial and cycle-consistency losses. Image courtesy of the authors of [56].

from two domains: band-limited field shot gathers (typically 4–10 Hz), denoted $h \in \mathcal{H}$, and synthetic low-frequency data (0–4 Hz), denoted $l \in \mathcal{L}$, derived from known subsurface models. Rather than relying on paired training data, the model learns mappings between domain distributions using adversarial learning and cycle-consistency constraints. The architecture comprises two generators, $G_{HL} : \mathcal{H} \to \mathcal{L}$ and $G_{LH} : \mathcal{L} \to \mathcal{H}$, along with two discriminators, D_L and D_H, trained jointly with adversarial, identity, and cycle-consistency losses. Waveform structure is preserved by enforcing the cycle-consistency conditions:

$$G_{LH}(G_{HL}(h)) \approx h \quad \text{and} \quad G_{HL}(G_{LH}(l)) \approx l,$$

allowing the network to produce plausible low-frequency extrapolations even in the absence of ground-truth labels. Once trained, G_{HL} is applied to real field data to generate low-frequency components, which are then used to enhance inversion quality in a subsequent two-stage full-waveform inversion (FWI) pipeline. The method is successfully validated on both synthetic and real marine field datasets.

An alternative strategy in semi-supervised learning is to generate "pseudo-labels" from unlabeled data or auxiliary measurements. For instance, [58] uses physics-based models to infer velocity maps from raw waveform data, effectively creating supervision signals for a downstream learning task. Similarly, [60] utilizes available well-log data to construct pseudo-labels for velocity profiles. [61] also generates pseudo-labels from waveform data but incorporates a CycleGAN architecture to improve the fidelity of the inferred labels. Together, these methods highlight the flexibility of SSL in balancing data availability and model generalization in CWI.

3) Self-Supervised Methods: Self-supervised learning (SSL) involves the model generating its own supervision signals from unlabeled data. The model creates tasks, such as predicting parts of the data from other parts, where labels are implicitly generated through the data itself.

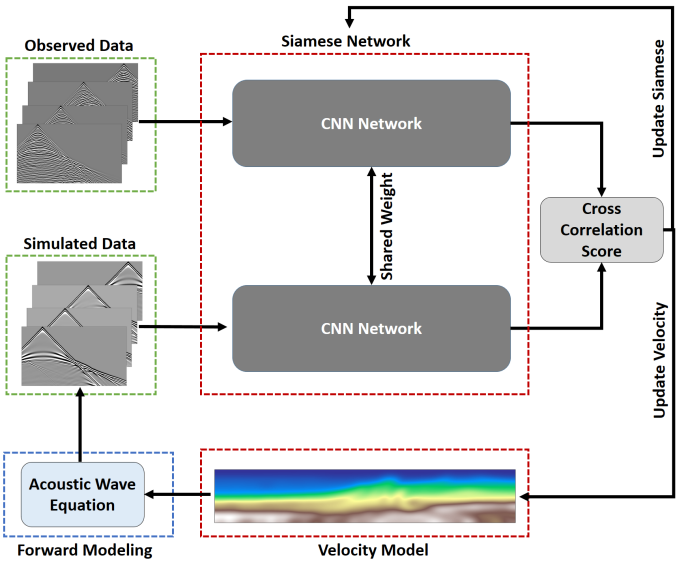


Fig. 5. Schematic illustration of the network architecture of SiameseFWI [62], a self-supervised learning framework for full waveform inversion. The model uses a Siamese neural network to compare simulated and observed seismic data in a shared latent space, enhancing sensitivity to key structural features. Image courtesy of the authors of [62].

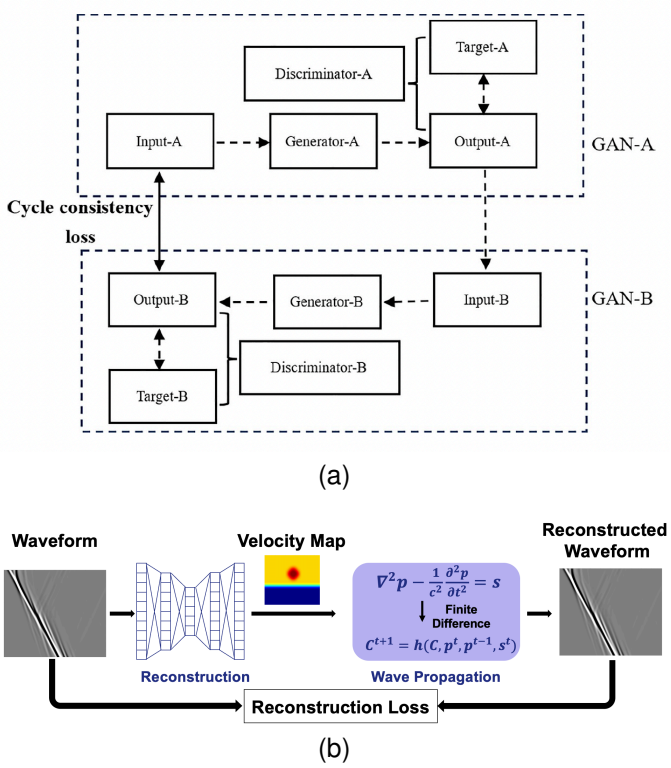


Fig. 6. Schematic overview of two representative unsupervised/unlabeled methods. (a) A CycleGAN-based unsupervised framework for low-frequency reconstruction in FWI, which learns to map high-frequency inputs to low-frequency components without paired labels [65]. (b) The UPFWI architecture, a physics-informed unlabeled method that maps waveform data to velocity models by minimizing the mismatch between observed and simulated waveforms via a differentiable wave equation [11]. Image (a) courtesy of the authors of [65].

Its key idea is to allow models to learn from measurements themselves without the need for a vast amount of labels. As an example, SiameseFWI [62] has been proposed as a novel self-supervised framework for FWI that uses a Siamese neural network to enhance the comparison between simulated and observed seismic data. Unlike traditional pixel-wise loss functions such as the ℓ_2 norm, SiameseFWI transforms both data types into a shared latent space via two identical convolutional neural networks with shared weights. This design enables the network to focus on meaningful features (*e.g.*, P-wave arrivals), and it minimizes the Euclidean distance between the learned representations to guide velocity model updates. The method achieves robust inversion performance on synthetic benchmarks and field data from Western Australia, demonstrating greater accuracy and resilience to noise, poor initial models, and unknown source wavelets.

SSL remains an emerging area within CWI, with growing interest in its application to low-frequency extrapolation, which is an essential step in overcoming the lack of low-frequency content in seismic data that limits FWI performance [14]. One early effort [63] introduces an SSL method that trains a neural network using paired seismic datasets with shared high-frequency content but varying low-frequency components. The model learns to reconstruct missing low-frequency information, although its performance is inherently constrained by the frequency range present in the original data. Furthermore, the required downsampling can degrade high-frequency resolution, limiting time precision. To address these challenges, [64] proposes a more effective two-stage SSL framework for low-frequency extrapolation. The warm-up stage initializes training using high-pass filtered inputs and original data as pseudo-labels. In the subsequent iterative data refinement stage, the model refines its predictions by using outputs from the previous epoch as pseudo-labels, with their high-pass filtered versions serving as new inputs. This iterative refinement progressively closes the gap between predictions and the ideal low-frequency content, enhancing extrapolation accuracy and robustness.

4) Unsupervised/Unlabeled Methods: This category encompasses methods that operate without paired supervision; *i.e.*, where only waveform samples are available and no velocity labels are required. It includes both *unsupervised learning* techniques that extract structure or features from data distributions, and *unlabeled inversion methods* that reconstruct medium properties by enforcing data consistency through physical models.

Unsupervised learning methods typically involve training neural networks on tasks defined from the data itself, allowing them to uncover latent structure or reconstruct missing information. For example, [65] proposes an unsupervised learning framework for low-frequency reconstruction in FWI using cycle-consistent adversarial networks (CycleGAN) as shown in Fig. 6a. Their method aims to infer large-scale low-frequency content from high-frequency seismic inputs, recovering information often absent in real field data. Unlike supervised methods that require labeled training pairs, CycleGAN enables training directly on unpaired seismic data, which is

more practical for real-world applications. To address training instability and enhance output quality, the authors constructed synthetic targets combining high-, mid-, and low-frequency components, and incorporated additional loss functions to improve reconstruction performance. This design allows the model to supply critical low-frequency components for more robust downstream inversion.

In contrast, unlabeled methods focus on mapping waveform data to velocity models by directly minimizing the mismatch between observed and simulated waveforms, using the full wave equation as a physical constraint. A representative example is the *Unsupervised Physics-informed Full-Waveform Inversion (UPFWI)* framework (shown in Fig. 6b) developed in [11]. UPFWI couples a neural encoder-decoder architecture with a differentiable wave-equation simulator, enabling end-to-end training with a loss defined in the data space:

$$\widehat{\boldsymbol{m}} = g_{\boldsymbol{\theta}^*}(\boldsymbol{d}) \,, \qquad (6)$$
$$\text{where } \boldsymbol{\theta}^* = \arg\min_{\boldsymbol{\theta}} \sum_{\boldsymbol{d}_i \in \boldsymbol{\Phi}_u} \mathcal{L}(f(g_{\boldsymbol{\theta}}(\boldsymbol{d}_i)), \boldsymbol{d}_i) \,.$$

Here, $\boldsymbol{\Phi}_u$ denotes a dataset of unlabeled waveform measurements, g_θ is the network mapping waveforms to velocity models, and f represents the forward modeling operator. The simulated waveforms are compared to the observed data to guide the network's learning. Methods in this category can be further divided into two subtypes:

- **Per-sample methods**, such as those in [66] and [67], reparameterize the model and optimize its parameters individually for each input, mimicking traditional inversion routines.
- **Per-domain methods**, like UPFWI [11] and [68], train a single model across a dataset and apply it to similar examples, enabling faster inference but possibly inheriting dataset-specific biases.

Together, these unsupervised and unlabeled strategies reflect a growing effort to decouple learning-based inversion from the need for explicit supervision, while still leveraging physical constraints and inductive priors to achieve accurate reconstructions.

5) Comparative Overview of Supervising Strategies for CWI: **Fully Supervised Learning.** Fully supervised learning provides the most direct application of machine learning to CWI by training models on datasets composed of paired waveform measurements and corresponding physical property maps. This strategy has been explored across various domains—including geophysics, medical imaging, and materials characterization—to approximate complex mappings from time-domain signals to spatial distributions of physical parameters such as velocity, impedance, or elastic moduli. Its appeal lies in its conceptual simplicity and fast inference: once trained, these models can generate real-time predictions without iterative solvers or numerical simulations.

However, the theoretical appeal of this approach belies practical challenges. The need to implicitly learn the underlying physics from data alone makes these models highly data-intensive. They often require orders of magnitude more labeled examples than physics-informed or hybrid approaches to achieve comparable generalization. Label acquisition is especially difficult in CWI contexts, where high-fidelity ground-truth models are either unavailable (as in seismic exploration), invasive to obtain (as in biomedical applications), or destructive (as in nondestructive testing of materials). Moreover, supervised models are vulnerable to domain shift: models trained on synthetic or idealized data may not transfer well to field conditions unless the training data closely mimics real-world complexity.

Despite these limitations, there are notable cases where fully supervised learning has achieved success, typically under carefully designed conditions. For example, [6] demonstrates accurate ultrasonic defect reconstruction in multilayered materials by tailoring the synthetic training data to match the sensor setup and propagation environment used in experiments. Similarly, [69] trains a Transformer-based network on over 20 million examples from a curated dataset of velocity models, enabling their model to generalize across diverse geophysical structures. These successes underscore that fully supervised approaches can work when domain fidelity and data scale are carefully managed—but they also highlight the inherent difficulty of deploying such methods directly in practical scenarios.

Ultimately, while fully supervised learning serves as a foundational paradigm for data-driven CWI, its dependency on exhaustive labeled datasets and lack of embedded physics limits its standalone applicability. These limitations have led to increased interest in semi-supervised, self-supervised, and physics-informed frameworks that can leverage unlabeled data or incorporate domain knowledge to improve generalization and interpretability.

Semi-Supervised Learning (SSL). Semi-supervised learning represents a pragmatic approach to bridging the gap between the data efficiency of supervised learning and the flexibility of unlabeled methods. It is particularly suited for CWI applications, where waveform measurements are abundant but reliable ground-truth velocity models are difficult to obtain. The key strength of SSL lies in its ability to exploit the information embedded in unlabeled data to guide or regularize model training, thereby enhancing generalization with limited supervision. Unlike fully supervised methods, SSL frameworks can be designed to integrate physics-based constraints or exploit structural relationships within the data to generate pseudo-labels or consistent feature mappings. In CWI, this enables networks to extract meaningful representations even in the absence of dense annotations. When properly configured, SSL methods can achieve performance close to their fully supervised counterparts, while being more robust to overfitting and more scalable to large, real-world datasets. By accommodating both labeled and unlabeled sources, SSL provides a flexible and data-efficient strategy for learning in complex wave-based imaging tasks.

Self-Supervised Learning. Self-supervised learning is an emerging paradigm that enables models to learn meaningful representations directly from unlabeled data by formulating surrogate tasks in which the labels are derived from the data itself. In the context of CWI, self-supervised learning offers a powerful means to exploit the inherent structure and

redundancy in waveform measurements, without relying on explicit supervision. Recent advances have demonstrated its potential in tasks such as low-frequency extrapolation and feature embedding. For example, the SiameseFWI framework [62] introduces a contrastive learning setup where pairs of simulated and observed waveforms are mapped into a shared latent space using a Siamese neural network, enabling robust misfit evaluation without the need for pixel-wise loss functions. Other approaches leverage signal masking or predictive reconstruction tasks to derive supervisory signals, allowing the network to learn frequency-domain or spatial-temporal patterns directly from the input data. The core advantage of self-supervised methods lies in their ability to harness large-scale unlabeled datasets for pretraining, which can subsequently enhance performance on downstream inversion tasks, particularly when labeled data is scarce. However, the success of self-supervised learning depends heavily on the design of pretext tasks and alignment with the physics of wave propagation, making it an active and promising area for further exploration in CWI.

Unsupervised/Unlabeled Methods. Unsupervised/unlabeled learning strategies provide a label-efficient alternative for tackling CWI problems by either extracting latent patterns directly from data or leveraging physics-based constraints to supervise the learning process. In unsupervised approaches, the goal is to uncover intrinsic structures within waveform data—such as temporal or frequency-domain features—that can facilitate inversion, without requiring paired velocity models. These methods are particularly effective when used for tasks like representation learning, data clustering, or generative modeling, and can serve as a powerful pretraining step for downstream inversion. In contrast, unlabeled physics-informed methods directly embed physical models, such as the wave equation, into the learning objective, allowing end-to-end inversion from measurements to physical parameters without explicit supervision. These techniques are especially advantageous in applications where unlabeled waveform data are abundant, but acquiring ground-truth models remains difficult. Despite the benefit of bypassing labeled data, these methods often require careful regularization, reliable forward modeling, and principled training strategies to ensure convergence and physical plausibility. Together, unsupervised and unlabeled methods offer a flexible and scalable paradigm for model training under realistic data constraints.

B. Machine Learning Methods by Learning Strategy

Computational wave imaging, unlike typical ML problems such as natural language processing, is governed by underlying physics. We are thus presented with an opportunity to incorporate critical physics and prior knowledge to potentially improve the performance of ML models in solving CWI problems [3]. As illustrated in Fig. 2, different approaches have been developed to incorporate physics into ML; we distinguish the following four:

- **Simulations/Measurements-Driven.** The method is built on a data-driven loss as in Eq. (5), and physics knowledge is implicitly represented via simulations and/or measurements.
- **Physics-Aware.** The method is built on a data-driven loss, but physics knowledge is introduced through explicit domain-aware regularization.
- **Parameterized Solution.** The method is built on a physics-based loss as in (Eq. 4) and ML is used to learn a parameterization of the physical property.
- **Plug and Play Priors.** The method typically makes use of a physics-based loss function, together with a generic denoising operator (possibly ML-based) that may not be designed/trained for the specific problem of interest.

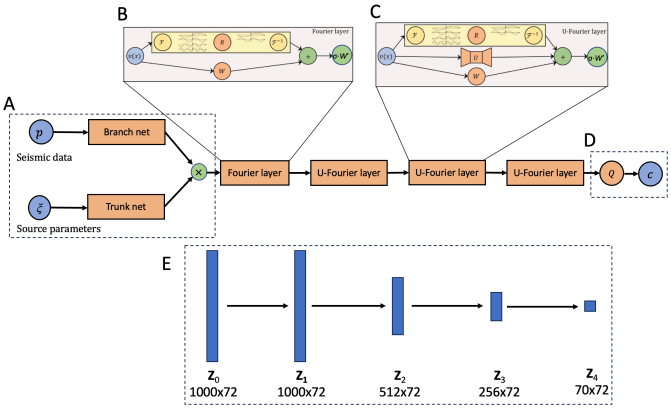


Fig. 7. Schematic illustration of Fourier-DeepONet, a simulations/measurements-driven method [70]. Image courtesy of the authors of [70].

1) Simulations/Measurements-Driven Methods: Full-physics simulations and measurements from experiments represent a major source of data for many ML methods for solving physics problems including CWI. Here, simulation data refers to synthetic waveforms generated by virtual imaging. This is achieved by applying the forward model in Eq. (1) to various realizations of the medium properties spanning the physical space of interest. The measurements are these data being acquired through lab or controlled experimental setup. Particularly, given the significant recent increase in available computing power, a very large number of pairwise realizations and waveforms becomes available, enabling fully supervised models as provided in Eq. (5). These simulation/measurement-driven methods learn the underlying physics indirectly through data, by observing how changes in physical parameters affect the resulting wavefields. In this way, they do not encode physics through explicit equations, but rather through exposure to physics-rich data generated via forward modeling.

Here, we use the model (called "Fourier-DeepONet") developed by [70] as an example to illustrate how simulations can be utilized to train ML models for solving CWI problems as shown in Fig. 7. Fourier-DeepONet is a representative example of this class because it explicitly leverages frequency-domain information embedded in simulation data to drive learning. It was developed to enhance the generalization ability of waveform sources including both frequency range and source locations. It builds on two major components: DeepONet

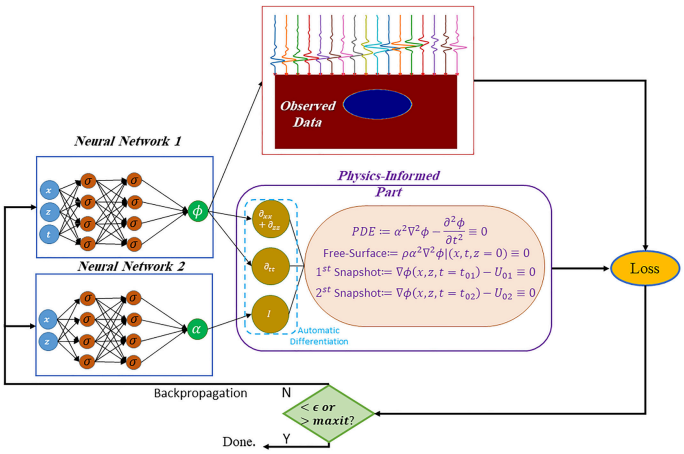


Fig. 8. Schematic illustration of a physics-informed neural network (PINN) [84], a physics-aware method for CWI that jointly learns the wavefield and velocity model by embedding the acoustic wave equation into the networks loss function. Image courtesy of the authors of [84].

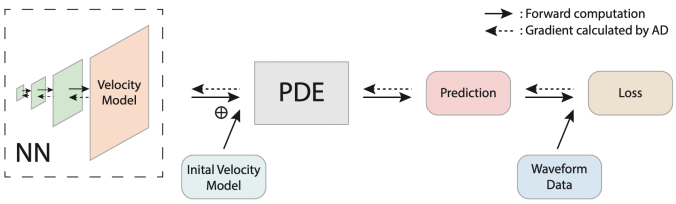


Fig. 9. Schematic illustration of parameterization-based method [92]. Image courtesy of the authors of [92].

(deep operator networks) [71] and U-FNO (a block combining Fourier neural operator and U-net) [72]. Particularly, source parameters (*i.e.*, frequencies and source locations) are employed as the inputs of the trunk net to facilitate the data-driven model with varying source frequencies and locations. The branch net and trunk net encode the waveform data and source parameters, respectively. They are linear transformations lifting inputs to high dimensional space. A few U-FNO blocks were then utilized as decoders to produce high-resolution imaging output. This use of frequency-domain learning makes Fourier-DeepONet particularly well-suited to handle variability in waveform sources, thus exemplifying how simulation-driven approaches can exploit structured physics knowledge implicitly embedded in data.

Fully supervised learning strategies, as discussed in the section on **Fully Supervised Methods**, prove highly effective in utilizing the large volume of simulation-data pairs. Beyond the above-mentioned method, a substantial body of research has explored simulation/measurement driven methods for FWI [1], [51], [52], [73], [74], USCT [9], [75]–[78], and NDT [53], [79], [80]. However, a common issue with these approaches is their limited generalization ability; that is, the models' suboptimal predictability when faced with unseen data significantly different from those in the training set. Thus, additional effort (such as transfer learning, active learning, etc.) [58], [81], [82] may be required to overcome the distribution shift between simulations and real-world measurements. Another method that has proven effective in enhancing generalization is the "CNN Correction after Direct Inversion" approach, as proposed by [83]. This method initially applies model-based inversion to closely approximate the physics model of the system, producing an estimate near the true solution. Subsequently, a CNN utilizes this estimate along with high-quality labels to learn how to eliminate artifacts and thus improve reconstruction quality. [78] implement a similar strategy to address the USCT problem.

2) Physics-Aware Methods: This category of methods integrates physical principlesmost notably, the wave equationdirectly into the learning framework through explicit constraints or regularization. A growing body of work has shown that enforcing the wave equation can significantly enhance inversion quality and physical interpretability in CWI [11], [84]–[89].

A representative example [84] is the physics-informed neural network (PINN) approach [90], shown in Fig. 8. This model jointly performs wave propagation and inversion by embedding the governing wave equation into the loss function of a neural network. The architecture includes two neural networks: the first learns the wavefield $\phi(x, z, t)$ as a function of space and time, and the second learns the velocity model $\alpha(x, z)$, which serves as a key physical parameter in the wave equation.

The Physics-Informed Part imposes the 2D acoustic wave equation $\alpha^2\nabla^2\phi - \partial^2\phi/\partial t^2 = 0$, along with free-surface boundary conditions and snapshot constraints that align predicted wavefields with observed data at specific times. All differential operators are computed via *automatic differentiation*, allowing the model to enforce physical constraints without requiring meshing or numerical solvers. The total loss function combines the wave equation residual, boundary losses, and waveform mismatch, and is minimized via backpropagation until convergence. This mesh-free framework provides a flexible and differentiable solution for solving inverse problems, particularly in settings with limited prior information or complex subsurface structures.

Beyond PINNs, several physics-aware models adopt alternative network structures and optimization schemes. For instance, [85] introduces SWINet, a waveform inversion model that integrates wave equation solvers as differentiable layers and treats the velocity map as a trainable parameter. Similarly, [88] proposes FWIGAN, which fuses the wave equation with a Wasserstein GAN formulation to recover subsurface models in a generative framework. While these methods effectively embed physical constraints, they often rely on good initializations and face scalability challenges due to the high computational cost of solving wave equations, especially in 3D settings.

Physics-based regularization has also been incorporated into end-to-end learning pipelines. [11], [86], [89], [91] propose encoderdecoder networks that embed physical constraints to guide learning. [86], in particular, develops a framework that jointly performs forward modeling and inversion using an invertible neural network. These approaches strike a balance between physical interpretability and computational tractability, and are promising for tackling multiparameter and elastic wave imaging tasks.

3) Parameterization Solution Methods: Physics knowledge can be represented by the parameter space of the neural networks. [93] develops the deep image prior, a type of convolutional neural network, to learn useful prior knowledge via re-parameterization. A similar idea has been developed to solve CWI problems as shown in Fig. 9. In particular, velocity maps are parameterized while the forward model is used to calculate the associated waveform and obtain the data misfit. Mathematically, parameterization can be posed as

$$\widehat{\boldsymbol{m}} = g_{\boldsymbol{\theta}^*(\boldsymbol{d})}(\boldsymbol{\beta}), \text{ where } \boldsymbol{\theta}^*(\boldsymbol{d}) = \arg\min_{\boldsymbol{\theta}} \mathcal{L}(f(g_{\boldsymbol{\theta}}(\boldsymbol{\beta})), \boldsymbol{d}), \tag{7}$$

where $\boldsymbol{\beta}$ is a random tensor drawn from a normal distribution; *i.e.*, $\boldsymbol{\beta} \sim \mathcal{N}(0, \sigma^2)$ and $g_{\boldsymbol{\theta}^*}(\cdot)$ is a network model used to parameterize the velocity maps. Unlike conventional physics-based methods that optimize velocity models directly in a high-dimensional voxel space, parameterization solution methods use a neural network to implicitly represent the velocity field. This has two key advantages. First, the network architecture acts as a strong implicit prior, promoting spatial smoothness, continuity, and structural plausibilitythereby regularizing the ill-posed inverse problem. Second, although the total number of network parameters can be large, the optimization is carried out over a lower-dimensional latent space (*e.g.*, via $\boldsymbol{\beta}$ or a compact representation), and the network maps this to a structured velocity model. This effectively restricts the solution space to a subset of physically plausible models, improving convergence stability and robustness to noise.

Parameterization solution methods, building on conventional physics-based approaches, inherit similar challenges. Typically, these methods require a well-defined initial velocity map, and factors like regularization and optimization techniques (*e.g.*, gradients and step sizes) significantly influence their convergence. Specifically, crucial to Eq. (7) are the selection of $\boldsymbol{\beta}$ and the network structure as in $g_{\boldsymbol{\theta}^*}(\cdot)$. Early work by [94] samples $\boldsymbol{\beta}$ from noise and used CNNs. [67] adopts a similar approach but with a deeper theoretical focus. Both methods involve a two-step process: network pre-training with a specific initial guess, followed by fine-tuning. The discretization assumption limits the output to fixed sizes, restricting transferability. These limitations have motivated recent developments to improve flexibility and physical fidelity. Overcoming these drawbacks, [92] develops a new strategy that integrates the wave equation for regularization, eliminating the pre-training step and addressing the ill-posed nature of CWI problems. More recently, [66] introduces an approach that employs a continuous implicit function via neural networks to represent velocity maps, accommodating arbitrary sizes.

4) Plug and Play Priors Methods: The Plug-and-Play Priors (PPP) framework, initially developed in the computational imaging community [96]–[98], provides a flexible and powerful approach for solving inverse problems by integrating advanced image denoisers into iterative optimization algorithms. Originally designed to incorporate classical denoisers such as BM3D [99], PPP has since evolved to support modern learning-based models like DnCNN [100], enabling the use of expressive neural network priors without requiring problem-specific retraining.

PPP is rooted in proximal optimization techniques [101], particularly the Alternating Direction Method of Multipliers (ADMM) [102]–[104], which solves inverse problems of the form:

$$\min_{\mathbf{m}} \; h(\mathbf{m}) + r(\mathbf{m}),$$

where $h(\cdot)$ typically represents a data fidelity term and $r(\cdot)$ serves as a regularization prior. The proximal operator, defined in [105, Ch. 6], is interpreted as a maximum a posteriori (MAP) estimator. This interpretation allows replacing it with advanced denoisers, including learned networks, while preserving algorithmic structure. Although this substitution breaks the strict optimization interpretation, it has been shown to converge under certain conditions [97], [106], [107].

In CWI, PPP has been adapted to handle the challenges of ill-posedness and data inconsistency. A representative framework, PPP-CWI [95], proceeds in two stages (shown in Fig. 10): an initial estimate is obtained from low-frequency data, followed by iterative refinement via a PPP-based scheme. The objective is:

$$\min_{\boldsymbol{m}} \; g(\boldsymbol{m}) + r(\boldsymbol{m}), \text{with } g(\mathbf{m}) = \frac{1}{2}\|f(\boldsymbol{m}) - \boldsymbol{d}\|_2^2,$$

where $f(\cdot)$ is the forward modeling operator and $\boldsymbol{d}$ denotes observed data.

The PPP-CWI algorithm iterates over three steps:

1) Model update (physics-consistent step):

$$\mathbf{m}^{(k+1)} = \arg\min_{\mathbf{m}} \; g(\mathbf{m}) + \frac{\rho}{2}\left\|\mathbf{m} - \mathbf{y}^{(k)} + \mathbf{u}^{(k)}\right\|_2^2, \tag{8}$$

typically solved using a first-order update:

$$\mathbf{m}^{(k+1)} = \mathbf{m}^{(k)} - \eta\left(\nabla g(\mathbf{m}^{(k)}) + \rho(\mathbf{m}^{(k)} - \mathbf{y}^{(k)} + \mathbf{u}^{(k)})\right), \tag{9}$$

where η is the learning rate and $\nabla g(\mathbf{m})$ is computed using the adjoint-state method.

2) Denoising update (prior-consistent step):

$$\mathbf{y}^{(k+1)} = \mathcal{D}_\theta\left(\mathbf{m}^{(k+1)} + \mathbf{u}^{(k)}\right), \tag{10}$$

where $\mathcal{D}_\theta$ is a pretrained denoising network (*e.g.*, DRUNet [108] or DnCNN [100]).

3) Dual update:

$$\mathbf{u}^{(k+1)} = \mathbf{u}^{(k)} + \mathbf{m}^{(k+1)} - \mathbf{y}^{(k+1)}. \tag{11}$$

This iterative scheme decouples the enforcement of physical consistency from the enforcement of prior knowledge, allowing both to be handled in a modular and flexible manner. Such decoupling is particularly valuable in CWI applications, where the forward model is highly complex, and the inversion problem is severely ill-posed. Traditional physics-based CWI methods often suffer from poor convergence due to non-convexity, high sensitivity to the initial model, and instability in the presence of noise or incomplete data. PPP mitigates these issues by incorporating powerful, data-driven priors, which is often learned from large datasets, directly into the inversion loop. These priors guide the solution toward physically

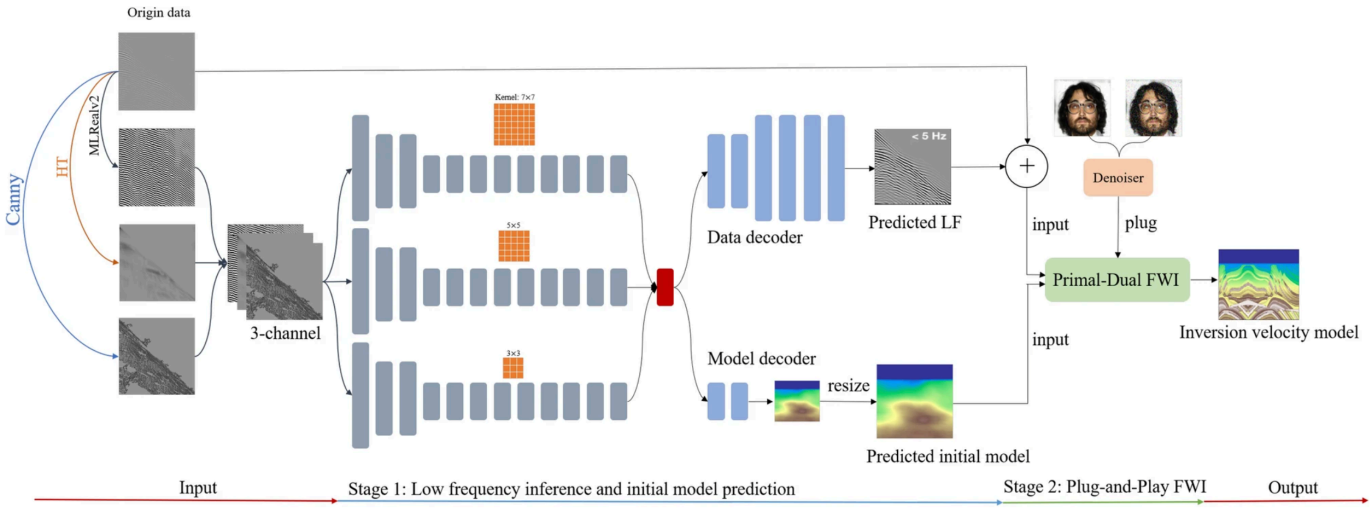


Fig. 10. Schematic illustration of the network architecture of PPP-CWI [95], a Plug-and-Play Priors framework for CWI that alternates between physics-consistent updates and learned prior denoising. Image adapted from [95].

plausible reconstructions, reduce reliance on handcrafted regularization terms, and improve robustness to data imperfections. Furthermore, by leveraging pretrained denoisers, PPP methods enhance generalization across different domains while reducing the need for extensive manual tuning. This makes them a promising and scalable alternative to conventional CWI, especially in large-scale or real-time imaging scenarios.

Several recent works have successfully applied PPP in CWI. [109] combines BM3D regularization with a proximal Newton solver to improve robustness in FWI, although performance degrades under complex noise. Learning-based alternatives have shown promise: [110] demonstrates that deep CNN priors outperform handcrafted regularization such as total variation, and [111] introduces a CNN-driven posterior sampling scheme to enhance uncertainty quantification in CWI.

5) Comparative Overview of Learning Strategies for CWI: This subsection provides a concise synthesis of the four learning strategies discussed in this section, namely, *Simulations/Measurements-Driven*, *Physics-Aware*, *Parameterized Solution*, and *Plug-and-Play Priors*. Each of these approaches brings distinct advantages and challenges. Summarizing their characteristics helps guide practitioners in selecting or combining appropriate strategies for specific CWI tasks.

Simulations/Measurements-Driven. These methods rely on supervised learning with paired data obtained from simulations or experimental measurements. Their primary strength lies in their ability to directly learn complex mappings from waveforms to physical properties when a large, diverse training dataset is available. However, their performance can degrade significantly under distribution shifts, particularly when real-world data differ from synthetic training conditions. These methods are most effective in well-controlled environments where high-quality paired data can be curated.

Physics-Aware. Physics-aware approaches incorporate physical knowledge, such as wave equations, either as soft constraints (*e.g.*, through loss functions) or embedded in the architecture itself. By doing so, they reduce reliance on labeled data and improve generalization to unseen scenarios. However, these methods often involve more complex optimization procedures and may incur higher computational costs. They are particularly advantageous when physical models are well established, but labeled data are limited or expensive to obtain.

Parameterized Solution. In this strategy, a neural network is used to parameterize the velocity model, which is then optimized through a physics-based loss involving the forward model. The network acts as an implicit prior, constraining the inversion process to a lower-dimensional, structured space. This can improve convergence and regularization. Nonetheless, the approach is sensitive to the choice of network architecture, initialization, and training dynamics. It is well-suited for applications where capturing global structure or enforcing smoothness is critical.

Plug-and-Play Priors. Plug-and-play methods decouple the physics and data-driven components, allowing for the use of pretrained denoisers or generative models as implicit priors within iterative solvers. This modularity enables flexible integration and leverages powerful priors without altering the physics simulator. The trade-off, however, lies in computational overhead and the need to carefully balance the influence of priors and data consistency. These methods are promising in scenarios where data priors are rich, but direct supervision is limited.

Toward Strategy Selection and Integration. Each learning strategy offers a distinct balance among generalization ability, interpretability, data efficiency, and computational cost. Selecting an appropriate strategy depends not only on theoretical considerations but also on the practical constraints of the specific CWI application. For instance, in data-rich but poorly modeled environments, simulation-driven methods may suffice. Conversely, in data-sparse domains with reliable physics, physics-aware or parameterized methods are often more effective.

Recent trends suggest that hybrid approaches can leverage the strengths of multiple strategies. For example, plug-and-

play frameworks can incorporate physics-aware denoisers or generative priors, such as score-based diffusion models, to improve inversion robustness without retraining the entire pipeline. Similarly, parameterized solvers can benefit from pretraining on synthetic data followed by fine-tuning with physics-constrained optimization, improving generalization while maintaining physical consistency.

Ultimately, strategy selection should consider factors such as the availability and quality of labeled data, the fidelity and computational cost of the forward model, the required level of interpretability, and tolerance to distribution shift. Designing adaptive systems that can switch between or combine strategies during training or inference remains an open but promising area for future research in CWI.

C. Emerging Trends in Machine Learning Techniques for Computational Wave Imaging

In this section, we examine two important advancements in ML-enhanced CWI methods: Uncertainty Quantification (UQ) and Generative AI (GenAI) Models. These developments offer significant opportunities to further enhance CWI techniques.

1) Uncertainty Quantification (UQ): Uncertainty is a fundamental feature of CWI and of inverse problems at-large: not only do we wish to infer the model-parameters, but we also want to quantify the uncertainty associated with this inference, reflecting the degree of confidence we have in the inversion. CWI problems are typically ill-posed and non-convex, often yielding non-unique or suboptimal solutions. Furthermore, real-world waveform measurements are generally compromised by acquisition noise from equipment, environmental disturbances, and other sources. These uncertainties are often categorized as epistemic (model-related) and aleatoric (data-related) uncertainties [112]. Epistemic uncertainty arises from unknown or unmodeled physics, such as the excitation pulse, detector characteristics, acoustic attenuation, density variations, and nonlinear effects. In contrast, aleatoric uncertainty reflects the inherent variability in the data itself. UQ mitigates these issues by providing predictive distributions and assessing prediction confidence.

In recent years, the Bayesian inverse problem has emerged as the most comprehensive and systematic framework for formulating and solving inverse problems with quantified uncertainties [113]–[117]. However, the solution of Bayesian inverse problems is extremely challenging; when the forward model is complex and the parameter dimension is large, Bayesian inversion becomes prohibitive with standard methods. Exploration of the posterior distribution using Markov chain Monte Carlo (MCMC) sampling is often computationally infeasible for CWI and often requires advanced sampling algorithms that leverage curvature information (geometric MCMC) [118]–[121]. Variational inference approaches introduce a parametrized approximation of the posterior distribution and solve a high dimensional optimization problem to minimize the Kullback-Leibler (KL) divergence between the approximated and true posterior [122]. However, in the context of CWI, variational inference approaches have been limited to two-dimensional synthetic problems [123] and entail significant computational cost due to the "curse of dimensionality" in approximating a probability distribution and its expectations for a high-dimensional parameter space.

ML offers new opportunities to enable UQ for CWI by use of novel network architectures and approaches, such as normalizing flows [124], [125], deep probabilistic imaging [126], and generative AI (see next section), that can help to break the curse of dimensionality and enable high-dimensional UQ. Here, we explore UQ estimation using neural networks, specifically through a method known as InvNet_UQ [127]. This approach focuses on aleatoric uncertainty and incorporates Simultaneous Quantile Regression (SQR) within a CNN framework [112]. InvNet_UQ employs a novel joint quantile regression loss function to enhance CWI by improving model reliability and quantifying prediction confidence. The network parameters of InvNet_UQ are obtained through the following optimization

$$\boldsymbol{\theta}^* \in \arg\min_{\theta} \left\{ \frac{1}{pqr} \sum_{k=1}^{p} \sum_{i=1}^{q} \sum_{j=1}^{r} E_{\tau \approx U[0,1]} [\mathcal{L}_\tau(g_{\boldsymbol{\theta}}(\mathbf{d}_k, \tau)(i,j), \mathbf{m}_k(i,j))] \right\}, \tag{12}$$

where k denotes kth sample in the dataset, (i,j) denotes the pixel location, and the pinball (quantile) loss $\mathcal{L}_\tau$, defined below, is designed to capture the discrepancy between predicted and actual values across different quantile levels of $0 \leq \tau \leq 1$.

$$\mathcal{L}_\tau(\mathbf{m}(i,j), \hat{\mathbf{m}}(i,j)) = \begin{cases} \tau(\mathbf{m}(i, & j) - \hat{\mathbf{m}}(i,j)) \\ & \text{if } \mathbf{m}(i,j) - \hat{\mathbf{m}}(i,j)) \geq 0 \\ (1-\tau) & (\hat{\mathbf{m}}(i,j) - \mathbf{m}(i,j)) \\ & \text{else.} \end{cases}, \tag{13}$$

Provided with a significance level α, the estimated imaging uncertainty can be computed from the $(1-\alpha)$ prediction interval around the median

$$u_\alpha(\mathbf{d}) := \hat{g}\left(\mathbf{d}, 1 - \frac{\alpha}{2}\right) - \hat{g}\left(\mathbf{d}, \frac{\alpha}{2}\right). \tag{14}$$

[127] shows that data-driven models with UQ excel in handling contaminated data, including noisy or erroneous measurements. Their approach not only boosts confidence in inversion tasks but also refines training sets, enhancing model performance. Unlike Bayesian neural networks, InvNet_UQ does not necessarily require the image prior to be a Gaussian distribution, potentially providing more accurate uncertainty bounds compared to other methods. Beyond the use of quantile regression for UQ, Monte Carlo dropout—a technique favored for its simplicity—is also widely used in CWI. [92] implements it by adding dropout layers to their network. Similarly, [128] uses a U-net architecture, employing both Monte Carlo dropout and bootstrap aggregating for uncertainty estimation. [129] uses a multi-layer fully connected network and Monte Carlo simulations to estimate uncertainties.

2) Generative AI (GenAI): GenAI models excel in representing probability distributions across diverse data domains and present new opportunities for CWI, and computational imaging in general. By learning an accurate characterization of the model parameter prior distribution, GenAI can 1) enhance

the solution of the Bayesian inverse problem and UQ [130]–[133]; 2) reduce ill-posedness of CWI by constraining the model parameter to belong to a high-probability manifold [81], [134], [135]; and 3) boost the performance of learning methods by generating synthetic data to augment training sets [74].

GenAI approaches can be broken down into two broad categories: sample-based approaches and score-based approaches. Sample-based approaches, such as Variational Auto-Encoders [136] (VAEs) and Generative Adversarial Models [137] (GANs) learn the push forward from an easy-to-sample latent distribution (*e.g.*, a multivariate *i.i.d.* Gaussian) to the data distribution. Once trained, they allow for *direct* (and computationally efficient) sampling. GANs, for example, were successfully employed to reduce the ill-posedness of CWI in the work of [81] and [134] by leveraging the GAN latent space as a nonlinear dimension reduction technique, while VAEs were successfully employed in [74] for data augmentation. However, it is worth noticing that GAN and VAE approaches are generally limited to small/medium scale problems and may suffer from the so-called *mode collapse* phenomenon [138]–[140], which prevents them from fully capturing the distribution of the data. Score-based approaches overcome this by directly learning the Stein score of the data distribution (*i.e.*, the gradient of the logarithm of the probability distribution function), which can be used in iterative sampling algorithms such as MCMC [141]. In particular, diffusion models [142]–[144] are now recognized as state-of-the-art in GenAI because of their high-quality sample generation, scalability to high-dimensional distributions, stability, and simplicity.

[132] uses a diffusion model for solving CWI problems with quantified uncertainties. This method extends [144] for solving linear inverse problems (like CT and MRI image reconstruction) using diffusion models to the more challenging CWI problem, which is governed by a highly non-linear forward model. In this approach, a diffusion model is first constructed from velocity model data. Diffusion models consist of two components: a *forward* diffusion process that uses a stochastic ordinary differential equation (SDE) to map the data distribution to a fixed noise distribution, and a *reverse* diffusion process that maps the noise distribution to the data distribution. In particular, [132] adopts the variance preserving (VP) SDE [145] for the forward diffusion process, which can be written as

$$d\mathbf{m}_t = -\frac{\beta_t}{2}\mathbf{m}_t dt + \sqrt{\beta_t} d\mathbf{w}_t, \quad t \in (0,T) \tag{15}$$

where the parameter β_t controls the noise variance, the initial condition $\mathbf{m}_0$ of the SDE is the velocity model, and $d\mathbf{w}_t$ is the noise introduced. The corresponding reverse diffusion process depends on the Stein score of the probability density of $\mathbf{m}_t$, which can be approximated by training the parameters θ of a vector-valued neural network $s_\theta(\mathbf{m}_t, t)$ using the cost function

$$\frac{1}{T}\int_0^T \lambda(t)\mathbb{E}_{\mathbf{m}_t|\mathbf{m}_0}\mathbb{E}_{\mathbf{m}_0}\left[\left\| s_\theta(\mathbf{m}_t,t) + \frac{\mathbf{m}_t - e^{-\frac{1}{2}\int_0^t \beta(s)ds}\mathbf{m}_0}{1-e^{-\int_0^t \beta(s)ds}}\right\|_2^2\right] dt, \tag{16}$$

where λ is a positive weighting function. Once trained, the network can generate new samples from the prior distribution of the model parameter, as the solution of another SDE (reverse diffusion process) as

$$d\mathbf{m}_t = \left(-\frac{\beta_t}{2}\mathbf{m}_t - \beta_t s_\theta(\mathbf{m}_t, T-t)\right)dt + \sqrt{\beta_t}d\mathbf{w}_t, \quad t \in (0,T), \tag{17}$$

using white noise at the initial condition. To condition the sample generation to the measurement data, [132] include an FWI update after each step of discretized SDE solver to enhance data consistency.

V. Computational Wave Imaging Applications

CWI is widely used in various scientific and engineering fields. This section provides examples of employing these methods to solve real-world problems. Appendix D includes source codes, packages, and training datasets, offering practical examples and a foundation for readers to address their own CWI challenges.

A. Seismic Full-Waveform Inversion

Seismic inversion, a tool for visualizing subsurface structures, is crucial in identifying and characterizing underground reservoirs. It also aids in diverse geological and environmental studies. This method involves creating precise velocity maps, which are essential for advanced post-processing techniques like reverse-time migration, to extract high-resolution details from subsurface data.

1) Leakage Detection for Carbon Sequestration: Geologic carbon sequestration (GCS), crucial in climate change mitigation, involves capturing and storing CO_2. Seismic imaging is key for early detection of CO_2 leakage, essential for project success. Effective leakage detection hinges on identifying leak presence, location, and magnitude. While traditional seismic methods are commonly used, they often lack early detection precision. Deep learning has brought significant improvements. [148] develops a method for direct CO_2 leakage quantification from seismic data. [58] introduces a semi-supervised approach targeting small leaks and imbalanced data scenarios. [74] employs a generative model to enhance rare event detectability. Moving beyond indirect inference from seismic data, [149] uses a generative adversarial network for mapping dynamic saturation changes. [150] create a network for direct CO_2 saturation mapping from seismic data. [128], [151] combine seismic, electromagnetic, and gravity data for a comprehensive saturation model with uncertainty estimation. [60] links seismic and electromagnetic data for improved CO_2 saturation modeling.

The Kimberlina dataset, generated by the National Risk Assessment Partnership project of the U.S. Department of Energy, is based on the geologic structure of a commercial-scale GCS reservoir at the Kimberlina site in the southern San Joaquin Basin, CA, USA. The simulation includes four modules: a CO_2 storage reservoir model (Fig. 11(a)), a wellbore leakage model (Fig. 11(b)), multi-phase flow and reactive transport models of CO_2/brine migration in aquifers (Fig. 11(c)), and a geophysical model.

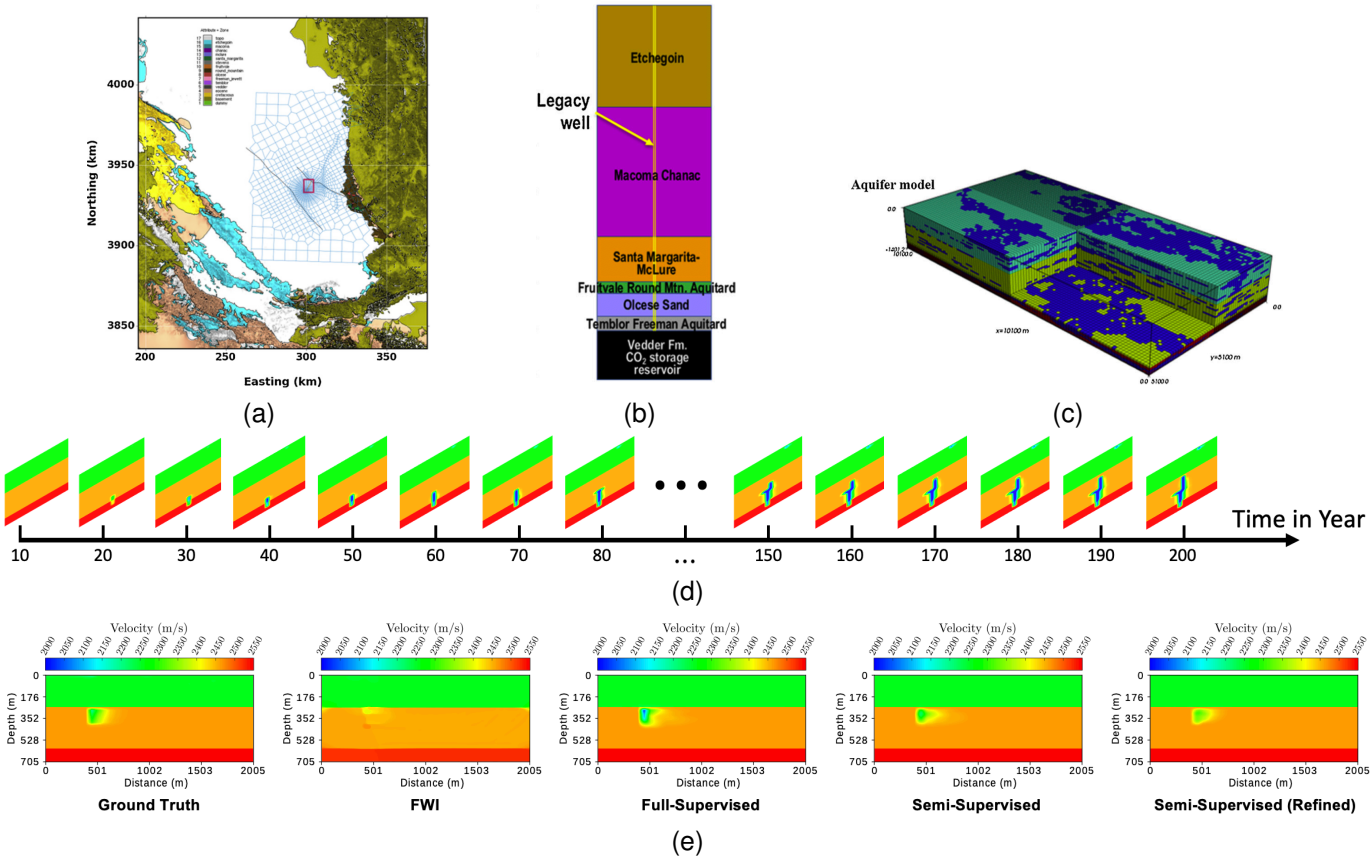


Fig. 11. Illustration of the Kimberlina dataset and three modeling modules used to generate the simulated velocity maps. (a) CO_2 storage reservoir model, (b) wellbore leakage model, (c) multi-phase flow and reactive transport models of CO_2 migration in aquifers [146], [147], and (d) Illustration of a set of simulation with 20 velocity maps for 200 years. A CO_2 leakage will result in a decrease in the velocity value in the location where the leak happens. (e) Visualizations of the early CO_2 leakage plume (from left to right): ground truth, results of physics-based FWI, fully-supervised model [51], semi-supervised model [58], and a refined semi-supervised model [58].

The P-wave velocity maps used in this study, which form part of the geophysical model, are constructed from the stratigraphic and lithologic information at the Kimberlina GCS site (Fig. 11(b)) [146], [147]. Fig. 11(d) shows a set of simulated velocity maps across 20 time steps spanning 200 years. To assess different inversion strategies, Fig. 11(e) compares the reconstructed velocity fields using three methods: physics-based seismic full waveform inversion (FWI) [45], a fully supervised learning approach [51], and a semi-supervised learning method incorporating adaptive data augmentation [58].

The results highlight the benefits of the adaptive augmentation strategy, which can be applied iteratively to refine CWI reconstructions. In each iteration, the current model generates approximate velocity maps from the measured waveform data, which are then used to synthesize new labeled waveform-velocity pairs via forward modeling. These new samples are added to the training set, and the model is retrained. This cycle is repeated, with each round progressively tailoring the training data to the target recorded waveform, thereby improving inversion accuracy. As shown in Fig. 11(e), this process helps better localize and delineate the CO_2 leakage plume, particularly in its early stages. Additional implementation details of the adaptive augmentation procedure are provided in Appendix C. In summary, the physics-based FWI lacks the resolution to capture small-scale leakage features; the fully supervised method suffers from shape distortion; whereas the semi-supervised approach delivers more accurate and physically consistent reconstructions.

2) Seismic Full-Waveform Inversion with Uncertainty Quantification: Robustness to noise is essential for CWI and broader inversion methods. It is important to distinguish "adversarial noise"—deliberate perturbations meant to deceive ML models—from "measurement noise," which naturally occurs during data collection. Since the latter is far more relevant to CWI, we consider adversarial scenarios to be beyond the scope of this review. In our second seismic FWI example, we specifically address measurement noise. To improve ML models' resistance to this, researchers have developed strategies such as UQ [127], advanced physics-guided regularization [11], and training with noisy data. We focus on the UQ method InvNet_UQ by [127].

The effectiveness of InvNet_UQ is demonstrated in Fig. 12, where it is applied to data contaminated with noise at a Signal-to-Noise Ratio (SNR) of 10. This is compared to results from InversionNet [51], revealing a significant performance decline for InversionNet under noisy conditions. In contrast, InvNet_UQ maintains higher accuracy in its predictions, showcasing its superior robustness to noise.

In addition to improved prediction quality, InvNet_UQ also generates uncertainty maps, as shown in the bottom row of

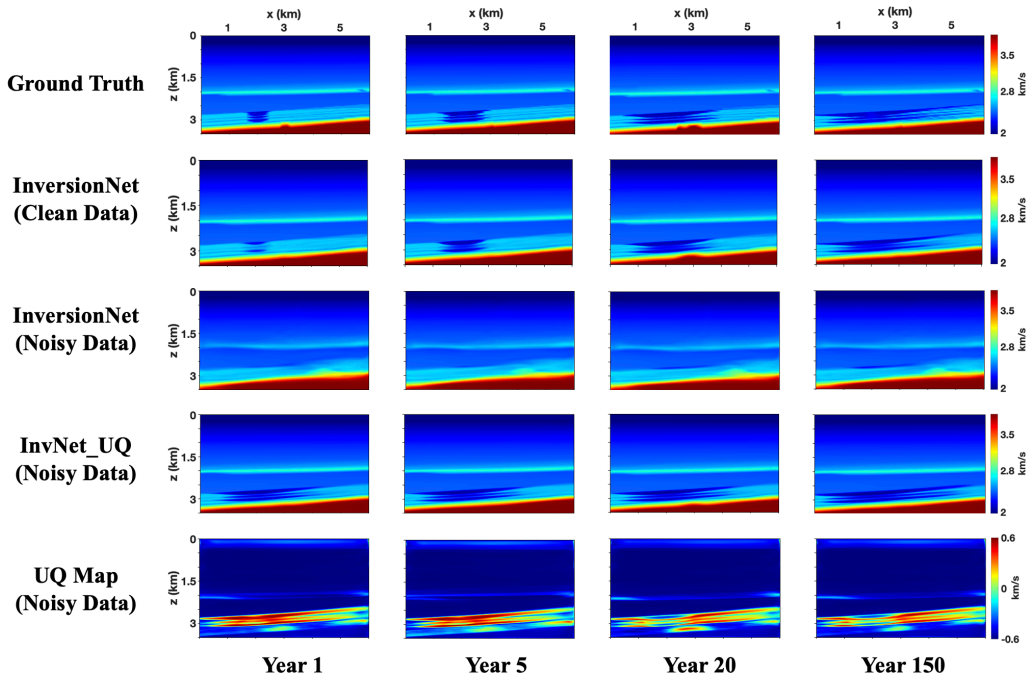


Fig. 12. Illustration of seismic full-waveform inversion with uncertainty quantification applying to noisy data. Ground Truth (Row 1); Results obtained using InversionNet [51] on clean data (Row 2); Results obtained using InversionNet [51] on noisy data with SNR=10 (Row 3); Results obtained using InvNet_UQ [127] on noisy data with SNR=10 (Row 4); Uncertainty map obtained using [127] (Row 5).

Fig. 12. These maps quantify the spatial confidence of the inversion output and serve multiple purposes. They can help practitioners identify regions of high uncertainty, informing risk-aware decision-making in geophysical and subsurface applications. Furthermore, these uncertainty estimates can guide the adaptive selection of training data or even act as a supervisory signal to train auxiliary models. Beyond interpretability, the ability to model predictive uncertainty also contributes directly to more robust inversion results. By estimating a conditional distribution over possible outputs, rather than a single point estimate, InvNet_UQ mitigates the risk of overfitting to noise or making overconfident errors in ill-posed regions. This allows the model to hedge its predictions in ambiguous areas, producing smoother and more stable reconstructions. The uncertainty maps shown in Fig. 12, calculated using Eq. (14), thus provide not only interpretability but also a mechanism to improve the inversion pipeline itself. As [127] have shown, this uncertainty information can be leveraged to enrich training data, potentially using generative AI models, thereby improving overall model performance.

B. Acoustic and Industrial Ultrasonic Imaging

Acoustic and industrial ultrasonic imaging is widely used for inspecting and monitoring engineered structures. Its applications range from detecting small defects in 3D printed materials to identifying structural issues in large airplane wings and locating pipeline leaks. The process involves using transmitters to emit signals and receivers to capture these waves post-propagation through the structure. Analyzing signal characteristics like arrival time, amplitude, and distortion through computed tomography helps create images representing structural properties such as sound speed, density, and temperature.

1) Acoustic and Industrial Ultrasonic Imaging for Defect Detection and Characterisation: As industry moves towards digitization, the resulting large datasets make ML-based inspection techniques increasingly relevant. Although useful and cost-effective for automating routine NDT processes, the use of ML is nascent in key industrial areas. Notably, in industrial ultrasonic inspection, most ML methods prioritize data-driven over physics-based models [79], [80]. In the NDT supervised method, [5] proposes a regression-based multilayer perceptron, which was formulated to estimate the plastic properties (*e.g.*, yield strength) of aluminum alloys, utilizing data from ultrasonic tests. [152] utilizes CNN for an ultrasonic framework to accurately pinpoint corrosion damage dimensions and locations, despite some forecasting inaccuracies. They also suggested reconstructing sparse signals from limited transducers through compressed sensing and CNN-based deep learning [4]. In addition, a semi-supervised anomaly detection model was introduced to establish a baseline anomaly detection score for the ultrasonic testing dataset [153]. Authors made adjustments to these networks to enhance their efficiency in addressing specific challenges. [154] presents a physics-informed neural network (PINN) to detect surface-breaking cracks in metal plates based on ultrasonic data. Compared with supervised methods, there is very limited literature available on semi-supervised and unsupervised methods for NDT. [155] uses a self-supervised denoiser to develop a method for flexible ultrasonic data acquisition, enhancing speed while preserving image quality.

While numerous studies in ML-based NDT have focused on defect detection, [6] develops a novel approach. Their study

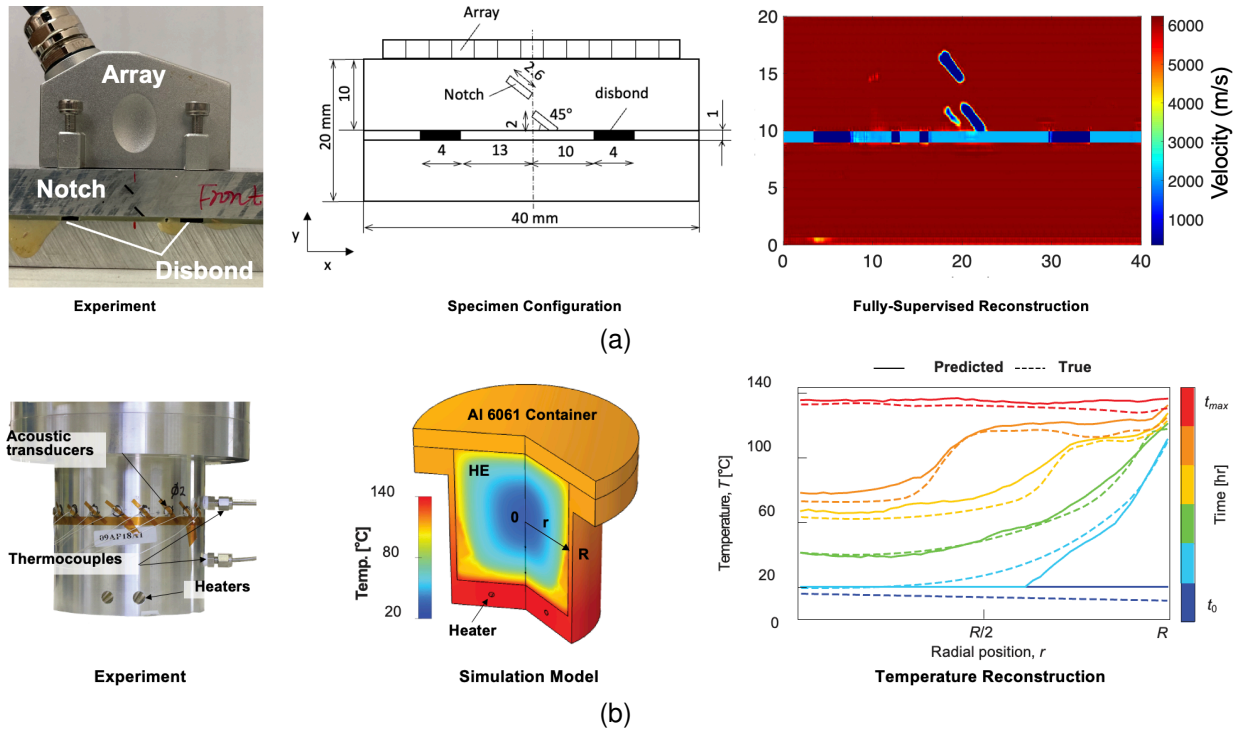


Fig. 13. Illustration of (a) ultrasonic imaging to identify high-contrast defects in multi-layered bonded structures and (b) Noninvasive acoustic temperature imaging. In (a), (Left Panel): Experimental setup consists of a CTS-PA322T portable ultrasonic phased array flaw detector, a linear phased array and a specimen; (Central Panel): Configuration of the specimen with two notches in the top layer and two disbonds in the 1 mm-thick adhesive layer; (Right Panel): FCN-based reconstruction (Colour bar shows the magnitude of velocity (m/s)). In (b), hybrid data collection with (Left Panel) experimental acoustic measurements and (Central Panel) simulated temperature profiles were used to train a CNN to compute the temperature profile within a container filled with high explosives (HE). In (b), (Right Panel) the predicted and true radial temperature profiles at several different times as the HE is heated from ambient (blue) to detonation (red).

introduces a quantitative ultrasonic imaging technique using a fully-supervised network to identify high-contrast defects in multi-layered bonded structures. This technique employs the fully-connected network (FCN) to convert ultrasonic data into longitudinal wave velocity models, which are then used to reconstruct defects in new data sets. In their experimental setup, as shown in the left panel of Fig. 13(a), a CTS-PA322T portable ultrasonic phased array flaw detector was utilized alongside a linear phased array. The phased array had a central frequency of 5 MHz and a pitch of 0.6 mm. The specimen design is detailed in the central panel of Fig. 13(a). The right panel of the same figure displays the reconstruction of this specimen using experimental data. The results demonstrate a high degree of accuracy in identifying the locations and shapes of two notches and disbonds. The reconstructed quantitative information closely matches the known specimen configuration, with artifacts being nearly undetectable.

2) Acoustic temperature imaging in high explosives: Acoustic waves are an attractive choice for noninvasive measurement of internal temperature for a range of applications such as monitoring chemical reactions or metal/plastic casting operations, assessing thermal energy storage devices, identifying abnormal heating in batteries, or determining if high explosives (HE) are safe to handle.

[156] develops a fully-supervised, simulation/measurement-driven temperature imaging technique that measures temperature distribution directly from the acoustic measurements using a CNN and a hybrid experiment/simulation training process illustrated in Fig. 13(b). The temperature imaging technique was demonstrated on cylindrical containers filled with HE (pentolite 50/50) as they were heated externally from ambient until ignition. During heating, 16 acoustic transducers around the container circumference transmitted/received (Tx/Rx) acoustic bursts centered at 350 kHz and two thermocouples measured temperatures at the wall and center to collect temperatures for training data (Fig. 13(b, Left Panel)).

To acquire training data temperature profiles within the container without excessive thermocouples disrupting the heating, the HE melting process was simulated numerically using an axisymmetric finite element model (COMSOL) and a radial temperature profile $T(r)$ was measured (Fig. 13(b, Central Panel)). To account for modeling errors, the simulated temperatures were corrected to agree with experimental thermocouple measurements. Training/testing samples comprised of data: acoustic waveforms X measured from a single transmitter, by N_{Rx} receivers and a label: a radial temperature profile T. The samples (X, T) were then used to train/test a CNN (see [156] for details).

Data were acquired from three nominally identical experiments/simulations and used to train and test the temperature imaging technique. Fig. 13(b, Right Panel) shows the predicted (dashed lines) and simulated "true" radial temperature profiles (solid lines) at various times as the cylinder was heated from approximately 20řC at t_0 (dark blue) until ignition temperature

of approximately 138řC was reached at $t_{max} \approx 3.5$ hr (red). Good agreement was observed between the predicted and true temperatures. From repeated training/testing (10 times), they measured a mean error of 14řC, which is approximately 12% of the range of temperatures throughout the experiments.

The temperature imaging technique based on a CNN and hybrid data provides considerable benefits over traditional temperature measurement techniques. CNN temperature imaging is noninvasive and does not require penetrating the container, unlike thermocouples and thermistors; [157] provides an internal temperature profile, unlike infrared thermography, which is limited to surface temperatures; [158] works for multi-phase, attenuating materials, unlike existing physics-based acoustic temperature imaging techniques, which require mounting transducers on the container interior and/or are limited to single-phase materials with low acoustic attenuation [159]–[164].

C. Medical Ultrasound Computed Tomography

USCT is an imaging method that uses tomographic principles for quantitative assessment of acoustic properties like sound speed, density, and acoustic attenuation [165]–[169]. It has become widely adopted, especially in breast imaging applications [165], [167], [170]–[180], which involves submersion of the patient's breast in water, surrounded by ultrasound transducers that emit and receive acoustic pulses, allowing full breast insonification.

USCT offers several advantages over traditional breast imaging methods like mammography, such as higher sensitivity to invasive cancer, cost-effectiveness, and being non-radiative and compression-free [181], [182]. Recently approved by the U.S. FDA for breast cancer screening in women with dense breasts and as a general diagnostic tool, USCT still faces significant algorithmic challenges. Key among these is improving image quality and reducing the lengthy image reconstruction times, which currently require high-performance, possibly GPU-accelerated computers [183], [184]. This computational demand not only limits USCT's clinical deployment but also raises costs, hindering its adoption in resource-limited settings. To overcome these challenges, innovative ML methods are being explored. [185] proposes a primal-dual gradient descent method for efficient data mapping, [8] employs loop unrolling for wave equation modeling, and [7] utilizes physics-informed neural networks to determine sound speed.

1) Ultrasound Tomography for Breast Cancer Detection using ring-array systems: In this section, we briefly describe three learning approaches tailored to ring-array USCT breast imaging. This practical system employs a circular ring array of elevation-focused ultrasonic transducers to achieve volumetric imaging by translating the array orthogonally to the imaging plane. Image reconstruction utilizes a slice-by-slice (SBS) method, reconstructing the three-dimensional (3D) volume by stacking two-dimensional (2D) images for each ring array position.

The cited works [75]–[78] explore a fully supervised simulation/measurement-driven approach, where a post-processing network learns to map preliminary velocity model estimates to high-resolution versions. These studies are distinguished by their use of anatomically and physiologically realistic numerical breast phantoms to train and assess the methods [76] (refer to Appendix D for more details). Two methods [75], [76] use an early-stopped USCT-derived velocity model as input for a U-net architecture, producing visually enhanced yet potentially inaccurate models. Conversely, [77], [78] show that using diverse input maps like travel time estimates and reflectivity maps leads to more accurate and reliable velocity models, although some fine structures may be erroneously introduced, as the authors acknowledge [186]. [187] and [188] demonstrate a fully supervised approach that addresses image reconstruction artifacts and inaccuracies arising from the mismatch between 3D wave propagation in the physical system and the simpler 2D imaging model often employed in breast USCT imaging.

Here we highlight the work of [9] on enhancing USCT (as shown in Fig. 14). They address the training and assessment of learned USCT methods using task-based measurements of image quality. In this work, a fully supervised physics-aware approach is proposed where a CNN mapping measurement data to the corresponding velocity is trained to minimize a specifically designed loss function that incorporates information specific to the clinical task for which the image was taken. To incorporate task-specific information, a weighted sum of the mean square error loss (MSE) in the image domain and a novel task-informed objective was proposed based on features extracted by a CNN-based numerical observer that was pre-trained on a tumor detection-localization task using the reference velocity models and tumor segmentation maps. Computer simulation studies using an idealized 2D USCT imaging system demonstrate that the proposed learning method can achieve a similar visual appearance to the velocity model estimated by USCT but also provide more reliable detection and localization of tumors.

VI. Lessons Learned

Traditional physics-based CWI methods face three challenges: (1) non-unique solutions, (2) multiple local minima, and (3) high computational demands. In this section, we aim to provide lessons learned and analyses concerning these crucial issues.

A. Ill-posedness and Non-uniqueness Solution

The challenge of ill-posedness, primarily caused by incomplete acquisition coverage and the vast dimensionality of the solution space, is a fundamental aspect of CWI problems. Traditional methods, such as regularization or preconditioning, can be effective, but usually require careful design of the penalty function to encode the user's preferences for which of the non-unique solutions to the unregularized problem to favor. Thus, selecting and optimizing the right regularization function to balance data fidelity and regularization terms, as in Eq. (4), can be challenging. In contrast, emerging ML-based methods offer alternative strategies to mitigate ill-posedness. Among the opportunities enabled by ML-based methods, we highlight the following approaches.

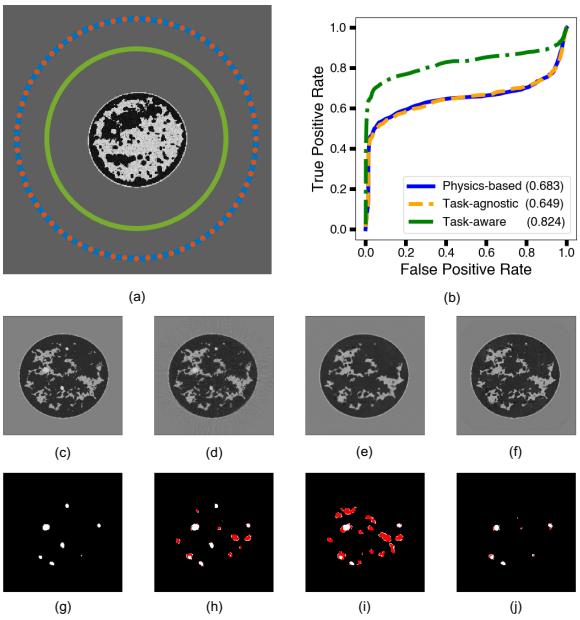


Fig. 14. (a) Geometry of the idealized 2D USCT imaging system in [9] with blue dots indicating emitter locations, red dots receivers, and green circle the field of view. (b) Receiver operating curve (ROC) for a tumor detection and localization task; area under the curve (AUC) values reported in the legend. The true speed of sound map (c) and estimates obtained by physics-based USCT (d), task-agnostic learned USCT (e), and the task-informed learned USCT method (f) in [9]. Tumor segmentation maps of the object (g), and segmentation maps estimated from reconstructed images with the three methods (h,i,j). True detection/localization is indicated in white and false detection in red. Speed of sound images produced by the task-informed method have similar visual or superior appearance (second rows) and provide more reliable lesion localization and detection compared to that achieved with physics-based or task-agnostic learned USCT. In particular, The ROC curve plot shows that the task-informed method can achieve over 20% higher AUC than physics-based USCT or other task-agnostic learned methods.

- **Learning the Null-Space Component of the Image from Labeled Data.** To address the challenge of non-uniqueness in CWI solutions, fully supervised models trained on carefully curated datasets are effective. A typical example of this is InversionNet [51], which uses training datasets constructed in a pairwise way to ensure a direct one-to-one correspondence between velocity maps and waveform data. This strategy confines the model's predictive capabilities to the data distribution of the training set, thereby alleviating the ill-posedness of CWI problems. However, a potential drawback is the models tendency to overfit to its training dataset, which can limit its generalization ability. These issues, along with computational cost and generalization capability, will be further discussed in subsequent sections.
- **Learning a Low-Dimensional Embedding of the Model Parameter Space.** An alternative strategy for reducing the null space involves transitioning the learning process to a lower-dimensional space. [189] provides a compelling illustration of this approach. Instead of performing inversion within the original, high-dimensional solution space, their method employs a sophisticated encoder-decoder framework to navigate a significantly reduced solution space (*i.e.*, the latent space). This projection technique not only mitigates the inherent ill-posedness associated with CWI but also uncovers intriguing relationships between data and labels, such as an unexpected near-linearity [10], [189].
- **Plug and Play Priors.** This particular regularization approach, rooted in the traditional CWI framework, is elaborated upon in the section on **Plug and Play Methods**. Its key distinction lies in its ability to derive the regularization term directly from data, moving away from the conventional practice of employing a predefined analytical regularization term. This data-driven approach substantially amplifies the efficacy of the regularization, offering a notable improvement and flexibility in addressing the challenges inherent in CWI.
- **Implicit Regularization through Neural Network Parameterization.** As discussed in the earlier section on **Parameterization Solution Methods**, the choice of a neural network for parameterizing solutions has a significant impact on the structure and exploration of the solution space. Following a similar idea, in the context of CWI, [92] finds that reparameterizing the velocity map using neural networks implicitly introduces a form of regularization. This regularization can improve CWI's effectiveness by shaping the solution space in a way that is informed by the neural network's architecture, leading to more robust imaging results.

B. Nonlinearity and Nonconvexity: Conventional vs. Data-driven CWI

Computational wave imaging is inherently nonlinear and nonconvex due to the physics of wave propagation and the limited information available in measured data. Nonlinearity arises from the sensitivity of wavefields to changes in material properties, particularly in heterogeneous or high-contrast media. Nonconvexity is further exacerbated by incomplete frequency content, which introduces ambiguity into the inversion and increases the likelihood of convergence to suboptimal solutions.

These challenges manifest differently across application domains. In geophysical FWI, the absence of low-frequency components is a primary limitation. These frequencies are essential for recovering large-scale background structures and for guiding the inversion toward global minima. Their absence results in a phenomenon known as *stratigraphic filtering*, where the recorded high-frequency wavefields predominantly reflect small-scale structures, suppressing information about the smooth, large-scale features. This effect contributes significantly to the cycle-skipping problem. In contrast, in USCT and NDT, the primary difficulties stem from strong acoustic contrasts and the need for high spatial resolution. Here, the lack of high-frequency data limits the ability to resolve fine structural details. In both settings, incomplete spectral information reduces gradient accuracy and increases instability in optimization.

These issues make optimization difficult for conventional CWI methods, such as the one shown in Eq. (4), which rely on first-order local optimization techniques like accelerated

TABLE I
COMPUTATIONAL AND MEMORY COST COMPARISON OF DATA-DRIVEN INVERSION METHODS. †: FOR AUGMENTATION METHOD [58], WE AMORTIZE THE COST OF PRETRAINING INVERSIONNET ON THE NON-AUGMENTED DATASET. SUBSEQUENT FINE-TUNING COSTS (δ) VARY WITH THE AUGMENTED DATASET SIZE.

Techniques		Computational Cost		Memory Cost	
		FLOPs (M)	Time (hr)	Parameter Number (M)	Max Memory (G)
Data-driven Inversion Methods	InversionNet [51]	$2,908$	4	24.5	11.4
	Augmentation [58]	$(2,908+\delta)^{\dagger}$	$(4+\delta)^{\dagger}$	24.5	$(11.4+\delta)^{\dagger}$
	Auto-Linear [10]	305.2	8	12.2	2.2
	UPFWI [11]	3,229	60	24.5	27.9
	Fourier-DeepONet [70]	3,664	15.3	15.5	29.2
	Invertible Network [86]	4,180	33.8	26.1	37.9

gradient or nonlinear conjugate gradient methods. Such methods often struggle to escape local minima and are particularly vulnerable to the cycle-skipping phenomenon, especially when reconstructing smooth, long-wavelength features. To address this, several strategies have been developed. Frequency continuation [190] is a multiscale approach that leverages the low-frequency information content in the waveform data to build an initial guess of the sought-after material properties and then sequentially refine them using higher-frequency information. Adaptive FWI [191] defines a new data fidelity term that, by introducing a learnable convolutional filter mapping the predicted data into the measured data, can overcome the cycle-skipping phenomenon. Optimal transport-based FWI [192] defines a new data fidelity term based on the quadratic Wasserstein metric to correctly correct for cycle-skipping.

Despite these advances, most "Data Consistent" learning-based methods (see Fig. 2) continue to adopt standard ℓ_2-based losses and remain susceptible to similar limitations, particularly in the presence of missing low-frequency content. Some recent studies (*e.g.*, [193]) have explored alternative loss formulations or implicit regularization schemes, but such methods remain relatively limited. More recently, a set of emerging methods [64], [194]–[196] has proposed learning-based strategies to reconstruct missing low-frequency components directly from high-frequency measurements. This approach uses a neural network to synthesize low-frequency wavefields, which are then used to augment the inversion process. By recovering this missing information, the method helps reduce cycle-skipping and improve convergence in bandwidth-limited scenarios. Such strategies highlight promising directions for integrating physics-informed modeling with data-driven learning to address fundamental limitations in practical imaging systems.

C. Computational Cost Analysis

Computational efficiency plays a critical role in the practical adoption of CWI methods. While algorithmic accuracy and generalization are essential, their real-world utility is ultimately constrained by available computing resources, problem scale, and application requirements. In this section, we outline key factors that influence computational costs and compare representative methods across a common benchmark to provide actionable insight.

- **Training vs. Inference Trade-off.** ML-based CWI methods generally separate computation into an intensive *training* phase and a typically lightweight *inference* phase. Once trained, these models can produce reconstructions rapidly, making them attractive for high-throughput or real-time applications. In contrast, physics-based methods, such as traditional adjoint-state methods, do not involve training but incur substantial cost during *inference*, as each reconstruction requires iterative PDE solves. Consequently, ML approaches are often advantageous in monitoring settings (*e.g.*, CO_2 storage or seismic hazard warning), where a single trained model supports repeated inferences across time or space.
- **Problem Size and Application Demands.** The feasibility of deploying a given method also depends on the scale and fidelity required by the application. For example, large-scale 3D seismic inversion demands high-resolution imaging over complex domains, often requiring terabyte-scale memory and extended runtime. Conversely, safety-critical systems such as tsunami warning or industrial inspection prioritize low-latency response, imposing strict time and compute budgets. While ML models offer efficient inference, they may struggle with generalization in out-of-distribution settings. Physics-based solvers offer more interpretability and robustness but are often prohibitively slow for time-sensitive tasks.
- **Hardware and Software Considerations.** Modern ML models are typically optimized for GPUs and can benefit from data-parallel processing on multi-GPU systems or HPC clusters. However, inference performance on CPU-only environments or edge devices can degrade significantly. Physics-based solvers, while more general in terms of platform compatibility, scale poorly with increasing problem complexity unless deployed on distributed-memory systems. Emerging architectures (*e.g.*, TPUs or

TABLE II
COMPUTATIONAL AND MEMORY COST COMPARISON OF A CONVENTIONAL PHYSICS METHOD [197] AND INVERSIONNET [51]. THIS COMPARISON IS BASED ON VARYING THE TRAINING-TO-TEST RATIO BY INCREMENTALLY ENLARGING THE TRAINING SET WHILE KEEPING THE TEST SET SIZE CONSTANT AS ONE SAMPLE. HERE THE COMPUTATIONAL COST FOR INVERSIONNET INCLUDES BOTH THE TRAINING AND INFERENCE IN TOTAL, WHILE THE PHYSICS METHOD ONLY INVOLVES INFERENCE.

Training/Test Ratio	Computational Cost		Memory Cost	
	Conventional Physics Method	InversionNet	Conventional Physics Method	InversionNet
10	113 s	0.3 s	0.4 G	5.2 G
100		3 s		12.1 G
1,000		30 s		80.3 G
10,000		300 s		762.4 G

hybrid CPU-GPU clusters) and frameworks (*e.g.*, JAX, TensorFlow, PyTorch) continue to shape how different methods perform across platforms.

To concretely compare computational profiles, we benchmarked several representative models on the OpenFWI Fault Family dataset [198]. Each model transforms input waveform data of size $5 \times 1,000 \times 70$ into a 70×70 velocity map. Performance metrics include floating point operations (FLOPs), training and inference runtime, memory usage, and parameter counts. Measurements were collected using the `ptflops` package on an NVIDIA Tesla V100 GPU, with all models trained over 120 epochs using mini-batch parallelism.

Table I summarizes results for ML-based approaches. InversionNet achieves rapid inference but exhibits increasing training cost as dataset size grows. Physics-aware methods like UPFWI [11] and invertible networks [86] incur additional computational overhead due to repeated forward modeling. For comparison, Table II reports the computational demands of a time-domain FWI solver [197], highlighting its high per-inference cost even with multiscale acceleration strategies.

While ML-based methods can reduce per-inference cost by orders of magnitude, they often require large volumes of high-quality training data and may not generalize beyond synthetic domains without careful domain adaptation. Physics-based methods, although more robust to unseen configurations, are less scalable in large or real-time scenarios. Hybrid frameworks, such as physics-informed networks and plug-and-play priors, offer promising compromises by combining inductive biases from wave physics with learning-based flexibility.

VII. LIMITATIONS, CHALLENGES, AND OUTLOOK

We summarize the aforementioned methods in Table III, outlining their advantages, limitations, and optimal use cases. As research in this field progresses, new challenges emerge. Below, we identify key challenges and suggest directions for future work that could significantly advance CWI.

Challenges in Generalization of Learning-Based Methods. A fundamental impediment to the deployment of learning-based CWI methods lies in their limited generalization capacity across heterogeneous acquisition conditions, physical media, and experimental setups. This challenge originates from the domain shift between the training environmentstypically synthetic and idealizedand real-world application scenarios, which are far more complex and variable.

Unlike in computer vision or natural language processing, where large-scale datasets are acquired from naturally occurring sources, training datasets in CWI are almost exclusively generated via numerical forward modeling on procedurally designed velocity models. These datasets, although grounded in physical principles, often fail to capture the full complexity of measurement noise, structural heterogeneity, and wavefield dynamics observed in practice. To understand the origins of this generalization breakdown, we decompose the problem into three interdependent components:

a) Input Discrepancy – Measurement Domain Gap: Wavefield measurements used for training are generated through forward simulations under idealized conditionscomplete acquisition coverage, deterministic source functions, and noise-free environments. In contrast, empirical measurements are corrupted by aleatoric noise, temporal jitter, sensor-specific distortions, and limited aperture effects. These discrepancies alter the spectral and statistical structure of the data, resulting in covariate shift at inference time and degraded model performance.

b) Output Discrepancy – Velocity Model Prior Gap: Ground-truth velocity maps in supervised training regimes are typically drawn from procedurally defined priors*e.g.*, Gaussian random fields, rule-based geological models, or anatomical templatesthat provide limited coverage of real-world variability. Such priors often lack high-order spatial statistics, anisotropy, or multiscale heterogeneity that characterize actual subsurface or biological structures. Consequently, the trained inverse operator becomes biased toward synthetic regularities and may fail to recover critical structural features in out-of-distribution domains.

c) Forward Model Discrepancy – Simulator Fidelity Gap: A third and subtler source of generalization error stems from discrepancies between the physical processes simulated during training and those present during deployment. Training-time simulations often assume simplified physicssuch as constant density acoustics, perfect boundary conditions, or linear propagation. These assumptions may not hold in real-world scenarios involving viscoelastic attenuation, scattering, mode conversion, or nonlinear effects. As a result, the learned mappings do not generalize well when faced with data governed by richer, unmodeled dynamics.

Together, these three sources form a framework for understanding generalization limits in CWI. They emphasize that robustness cannot be achieved by improving data priors

or network architectures alone: the fidelity of the simulated environment and its alignment with real-world physics is equally critical.

Looking forward, advancing the generalization and applicability of learning-based CWI methods will require the development of tightly coupled frameworks that integrate data-driven models with high-fidelity physics solvers. Recent progress in differentiable programming and operator learning presents an opportunity to embed wave physics more deeply into learning pipelines, enabling inversion models to account for complex propagation phenomena such as anisotropy, viscoelasticity, and mode conversion. Parallel to this, semi-supervised and self-supervised learning strategies offer a path toward harnessing large volumes of unlabeled field data, thereby improving model robustness while reducing reliance on synthetic priors. Another important direction lies in the co-design of acquisition and inference—jointly optimizing transducer placement, source design, and learning objectives to improve imaging resolution under practical constraints. Finally, there is a growing need to incorporate principled uncertainty quantification into learning-based frameworks to assess model confidence and guide decision-making in safety-critical applications such as medical imaging and subsurface monitoring.

Model Interpretability. The topic of model interpretability is of particular significance for deep neural networks known for their "black box" nature. In CWI, understanding the rationale behind a model's predictions can be as helpful as the predictions themselves. Interpretability enables us to grasp why certain predictions are made, making it an invaluable tool for debugging, improving model performance, and identifying biases. While tools like UQ, as mentioned earlier, can aid in interpreting deep models, extensive research on this aspect has been conducted in the broader ML/AI community [199], [200]. Surprisingly, the CWI field has seen relatively little exploration in this area, pointing to a promising direction for future research and the potential for significant advancements in CWI through enhanced interpretability.

Imaging Quality Assessment. Implementing effective quality control plays a crucial role in evaluating successful applications of CWI. Ultimately, image quality should be assessed based on the utility of the image to perform a specific task. For example, in the context of carbon sequestration, CWI may allow the detection of an underground gas plume; in medical USCT, CWI can support breast cancer screening and diagnostics tasks; and, in industrial ultrasonic CWI, can allow the non-destructive detection of defects. However, a growing body of evidence is showing that, while ML-based approaches can improve conventional metrics of image accuracy (such as mean square error, MSE; mean absolute error, MAE; or structural similarity, SSIM), they can result in diminished task performance [201]–[203]. In fact, these metrics do not always correlate with the usefulness of a reconstructed image for performing a task of interest [204], [205]. Due to this discrepancy, there is a growing interest in assessing the task performance of proposed image reconstruction methods by use of statistical signal detection theory and numerical observer methods [9], [201], [206], [207].

VIII. Acknowledgements

Y. Lin acknowledges support from the University of North Carolina's School of Data Science and Society through a faculty start-up grant. Y. Lin and S. Feng also acknowledge support from the U.S. Department of Energy (DOE) Office of Fossil Energys Carbon Storage Research Program, under the Science-Informed Machine Learning to Accelerate Real-Time Decision Making for Carbon Storage (SMART-CS) Initiative. U. Villa and M. Anastasio acknowledge support from the National Institute of Biomedical Imaging and Bioengineering (NIBIB) of the U.S. National Institutes of Health (NIH) under awards EB028652, EB031585, and EB034261. U. Villa would also like to acknowledge Mr. Luke Lozenski for assisting with the generation of Fig. 14 and Mr. Evan Scope Crafts for the insightful discussion and suggestion regarding the Generative AI Section.

Appendix A
Wave Equations

This supplementary section provides detailed formulations for wave equations that extend beyond the acoustic models discussed in the main text. These include elastic, viscoacoustic, and anisotropic equations used to model more complex wave phenomena.

A. Elastic Wave Equation

Within a solid medium, as the material undergoes deformation caused by stress, this results in the transmission of both P-waves and secondary (S) waves. The elastic wave equation follows [20]:

$$\begin{aligned} \rho\frac{\partial \mathbf{u}}{\partial t} - \nabla\cdot\underline{\underline{\boldsymbol{\sigma}}} &= 0\,, \\ \frac{\partial \underline{\underline{\boldsymbol{\sigma}}}}{\partial t} - \mu\left(\nabla\mathbf{u} + (\nabla\mathbf{u})^T\right) - \lambda(\nabla\cdot\mathbf{u})\mathbf{I} &= \mathbf{S}, \end{aligned} \tag{18}$$

where $\mathbf{u} \in \mathbb{R}^d$ is the particle velocity, $\underline{\underline{\boldsymbol{\sigma}}} \in \mathbb{R}^{d\times d}$ is the stress tensor, $\mathbf{I}$ is the identity matrix, λ and μ are the Lamé parameters, and $\mathbf{S} \in \mathbb{R}^{d\times d}$ represents external sources. The P- and S-wave speeds are $V_P = \sqrt{(\lambda+2\mu)/\rho}$ and $V_S = \sqrt{\mu/\rho}$.

B. Viscoacoustic Wave Equation

The viscoacoustic wave equation models attenuation effects via a memory term [23]:

$$\begin{aligned} \frac{\partial p}{\partial t} + K\frac{\tau_\epsilon}{\tau_\sigma}\left(\nabla\cdot\mathbf{u} + r_p\right) &= \mathbf{S}\,, \\ \frac{\partial \mathbf{u}}{\partial t} + \frac{1}{\rho}\nabla p &= 0\,, \\ \frac{\partial r_p}{\partial t} + \frac{1}{\tau_\sigma}\left(r_p + K\left(\frac{\tau_\epsilon}{\tau_\sigma} - 1\right)(\nabla\cdot\mathbf{u})\right) &= 0\,. \end{aligned} \tag{19}$$

Here, K is the bulk modulus, τ_ϵ and τ_σ are relaxation times, and r_p is a memory variable.

TABLE III
A SUMMARY OF CWI METHODS. THOSE AFOREMENTIONED METHODS ARE CATEGORIZED INTO DATA-DRIVEN INVERSION METHODS AND PHYSICS-BASED METHODS. THEIR RESPECTIVE ADVANTAGES, LIMITATIONS, AND PREFERABLE APPLICATIONS ARE PROVIDED IN THE TABLE.

Techniques		Advantage	Limitations	Preferable Applications
Data-driven Inversion Methods	InversionNet [51]	• Directly extract physical principles from labeled data. • Achieve high accuracy in estimating in-distribution data.	• Depends significantly on the availability of ample labeled data. • Limited ability to generalize to out-of-distribution data.	• Optimal for problems with abundant pre-labeled data and target data similar to the training set, like in monitoring tasks.
	Augmentation [58]	• Decrease the model's dependence on labels. • Enhance the training set's representativeness by integrating underlying physics and incorporating unlabeled data.	• Increases computational costs for model fine-tuning.	• Ideal for tasks requiring a mix of pre-labeled and additional data, like unlabeled data, exemplified by multi-physics imaging.
	Auto-Linear [10]	• Train the encoder and decoder independently using self-supervised learning. • Boost model efficacy by utilizing unpaired data and labels in various applications.	• More samples would be needed to train the model. • Additional computational cost due to pre-training of the encoder and decoder.	• Adaptable to imaging tasks under diverse scenarios, including variable testing conditions.
	UPFWI [11]	• Eliminates the need for label information. • Enhanced generalization capability through the integration of physics.	• Requires more samples than supervised learning. • Increased computational costs due to extensive forward modeling.	• Ideal for label-free problems with ample waveform data, such as Distributed Acoustic Sensing (DAS) imaging.
	Fourier-DeepONet [70]	• Enhances the model's generalization capability for source and receiver locations. • Boosts the model's robustness regarding source frequency.	• Requires additional samples to encompass a broader range of source/receiver locations and source frequencies. • Results in higher computational costs.	• Optimal for applications involving diverse or uncertain source/receiver characteristics, such as central frequency and locations.
	Invertible Network [86]	• Boosts inversion performance through the integration of forward modeling. • Enables dual functionality for both inversion and forward modeling in the model.	• Significantly increased computational costs. • Necessitates a larger sample size.	• Ideal for applications lacking forward modeling, such as blind inversion scenarios.
Physics-Based Inversion	Conventional Physics-Method [14]	• Upon optimization, the inversion reliably conforms to the measurements. • Several computational techniques, such as advanced regularization and preconditioning, exist to alleviate the issue of ill-posedness.	• Computationally demanding when inverting multiple datasets. • Results in high sensitivity to initial guesses and susceptibility to cycle-skipping.	• Optimal for inverting baseline data during time-lapse monitoring.
	Parameterization [92]	• Inherits similar advantages as those found in conventional physics methods. • Further mitigates the effects of local minima and is more robust against noise in data.	• Requires retraining for new data adaptation. • Retains the limitations of physical inversion techniques, including sensitivity to initial guesses and cycle-skipping.	• Ideal for scenarios lacking training samples.
	Plug and Play [110]	• Analogous to the conventional physics methods. • Offers flexibility in eliminating artifacts and noise during inversion.	• Comparable to the aforementioned approach. • Choosing the denoising operator is challenging and demands domain expertise.	• Ideal for scenarios lacking training samples with known noise distribution.

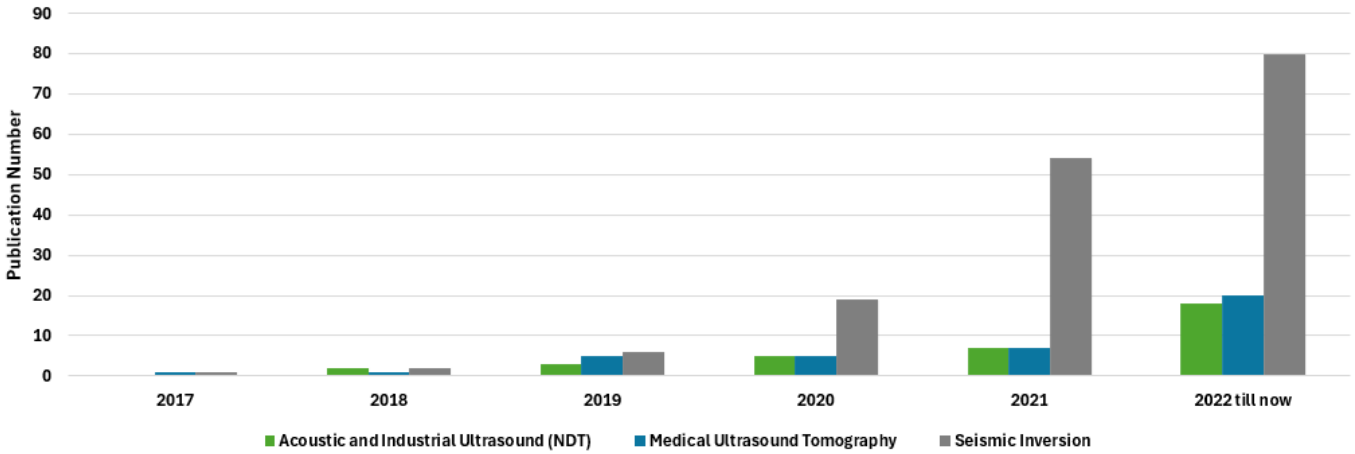


Fig. 15. The overall trends of the ML methods developed in computational wave imaging. The figures are plotted based on a collection of over 200 papers.

C. Anisotropic Wave Equation

The pseudo-acoustic approximation for vertically transverse isotropic (VTI) media is expressed as [21], [24]:

$$\begin{aligned} \frac{\partial u_x}{\partial t} - \frac{1}{\rho}\frac{\partial \sigma_{xx}}{\partial x} &= 0\,, \\ \frac{\partial u_z}{\partial t} - \frac{1}{\rho}\frac{\partial \sigma_{zz}}{\partial z} &= 0\,, \\ \frac{\partial \sigma_{xx}}{\partial t} - \rho v_p^2\left[(1+2\epsilon)\frac{\partial u_x}{\partial x} + \sqrt{1+2\delta}\frac{\partial u_z}{\partial z}\right] &= S_{xx}\,, \\ \frac{\partial \sigma_{zz}}{\partial t} - \rho v_p^2\left[\sqrt{1+2\delta}\frac{\partial u_x}{\partial x} + \frac{\partial u_z}{\partial z}\right] &= S_{zz} \end{aligned} \tag{20}$$

where u_x, u_z are particle velocities, σ_{xx}, σ_{zz} are stress components, ϵ, δ are Thomsen anisotropy parameters, and v_p is vertical P-wave velocity.

Appendix B
Research Trends and Existing Review Papers

Our review of the literature spans over 200 publications from diverse branches of the CWI, where a notable uptick in machine learning-centric studies is evident, as illustrated in Fig. 15. These ML-focused methodologies have been systematically categorized in two ways: one is based on the nature of their training sets (whether samples are labeled, whether samples and labels are associated, etc); the other is based on the learning strategy (physics-aware, parameterized, etc.). The proportional representation of each category, delineated by the method of supervision and learning strategy, is graphically summarized in Figs. 16(a) and 16(b), respectively.

Table B summarizes a selection of high-quality review papers, categorized into three primary groups: physics-based methods, machine-learning approaches, and hybrid methods combining data-driven techniques with fundamental physics principles. The descriptions of each category are provided below. Additionally, Table IV presents a curated collection of papers encompassing the full spectrum of categories and groups identified in our analysis.

- **Physics.** Seismic FWI, acoustic NDT, and USCT have extensively utilized physics-based methods. In seismic FWI, comprehensive insights into techniques for exploration geophysics can be found in the work of [14]. Additionally, [15] presents a distinct perspective tailored to global seismology challenges. [208] provides a valuable summary of physics-based methods applied across both seismic and medical imaging domains. [209] discusses the applications of acoustic imaging techniques, particularly in the realm of non-destructive flaw detection, localization, and sizing within materials.
- **Machine Learning.** [210] overviews the general topic of ML for computational imaging problems, mainly concentrating on general methodology development rather than a specific imaging problem. [211] provides an in-depth understanding of ML techniques tailored for seismic imaging challenges, with a specific focus on "pure" ML methods. [2] examines deep neural networks, exploring their diverse applications in geophysics, which encompass seismic imaging among others. [212] offers an extensive review of pure ML approaches, particularly for biomedical imaging, including USCT.
- **Hybrid.** There are several reviews on hybrid models for general inverse problems [213]–[215]. Both [216] and [217] explore ML methods for solving imaging inverse problems. Particularly, [216] explores methods and applications based on hybrid ML models, while [217] reviews the plug-and-play method and its applications. In the seismic FWI domain, [3] discusses hybrid ML methods with a focus on model development.

Appendix C
Adaptive Data Augmentation – A Semi-Supervised Method

This appendix describes an adaptive data augmentation strategy for CWI, originally proposed by [58], which is based on semi-supervised learning. The core idea is to iteratively refine the training dataset by generating new samples that are statistically closer to a given observed waveform $\boldsymbol{d}_{\text{obs}}$.

Conventional data augmentation techniques commonly used in image processing (*e.g.*, rotations, flips, scaling) are generally not applicable in wave-based imaging due to the underlying

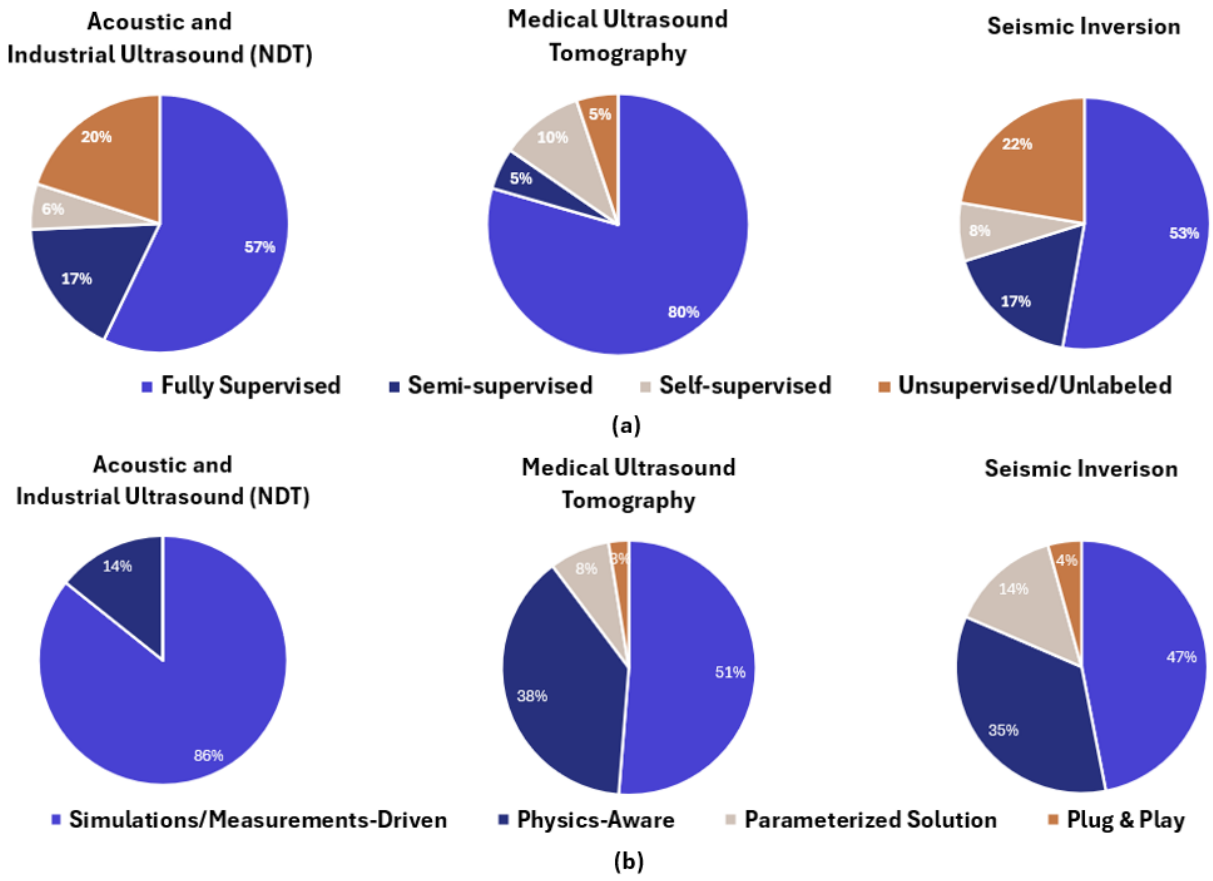


Fig. 16. Illustrations of (a) a breakdown of all the collected papers in four groups of methods under supervision strategy for acoustic imaging, ultrasound tomography, and seismic imaging, and (b) a breakdown of all the collected papers in four groups of methods under learning strategy for acoustic imaging, ultrasound tomography, and seismic imaging.

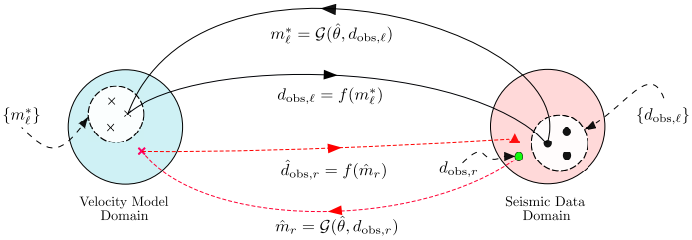


Fig. 17. Adaptive Data Augmentation: Approximate solver $\mathcal{G}(\hat{\theta}, \boldsymbol{d}_{\text{obs}})$ is fully-trained over labeled set $\{m_\ell^*, \boldsymbol{d}_{\text{obs},\ell}\}$, and applied to unlabeled seismic data $\boldsymbol{d}_{\text{obs},r}$ to generate new velocity maps $\hat{\boldsymbol{m}}_r$. Physically-coherent seismic data $\hat{\boldsymbol{d}}_{\text{obs},r}$ is then generated using the forward model f, producing a new labeled set $\{\hat{\boldsymbol{m}}_r, \hat{\boldsymbol{d}}_{\text{obs},r}\}$ which is added to the original training set.

physical constraints. In contrast, this adaptive strategy creates additional training samples that are both physically consistent and specific to the target inversion task. The method consists of the following steps (as illustrated in Fig. 17):

1) Estimate approximate solver $\mathcal{G}(\hat{\boldsymbol{\theta}}, \boldsymbol{d}_{\text{obs}})$;
2) Generate approximate velocity maps from unlabeled data $\hat{\boldsymbol{m}}_r = \mathcal{G}(\hat{\boldsymbol{\theta}}, \boldsymbol{d}_{\text{obs},r})$;
3) Create synthetic seismic data using forward model $\hat{\boldsymbol{d}}_{\text{obs},r} = f(\hat{\boldsymbol{m}}_r)$;
4) Add new pairs to the original training set.

This semi-supervised augmentation scheme enhances model accuracy by injecting physically meaningful and geologically relevant examples into the training data. The process can be repeated iteratively, with each round retraining the operator $\mathcal{G}$ using the expanded dataset. This iterative refinement helps improve the quality of the reconstructed velocity maps for the observed data $\boldsymbol{d}_{\text{obs}}$.

Appendix D
Open-Source Software and Data Availability

Accessible open data resources facilitate research on wave imaging challenges. Below, we provide a few open datasets for different wave imaging problems.

- **Seismic Full-Waveform Inversion.** We find two open accessible datasets: OpenFWI [198] and $\mathbb{E}^{\mathbf{FWI}}$ [220], of which OpenFWI was designed for seismic imaging through the application of acoustic wave equations, and $\mathbb{E}^{\mathbf{FWI}}$ was tailored for seismic imaging employing elastic wave equations. Particularly, OpenFWI comprises 12 datasets that have been synthesized from a variety of sources. These datasets span a wide range of geophysical domains, including interfaces, faults, CO_2 reservoirs, and more. They also encompass different geological subsurface structures, such as flat and curved formations, and offer varying amounts of data samples. Within the OpenFWI collection, you can find both P-wave velocity

Reference	Year	Application Domain	Physics	ML	Hybrid
Virieux and Operto [14]	2009	Seismic Inversion	✓		
Agudo [208]	2018	Medical Ultrasound	✓		
Felice and Fan [209]	2018	Acoustic & Industrial Ultrasound	✓		
Tromp [15]	2020	Seismic Inversion	✓		
Operto *et al.* [218]	2023	Seismic Inversion	✓		
Ongie *et al.* [210]	2020	Computational Imaging		✓	
Wang *et al.* [212]	2020	Medical Ultrasound		✓	
Adler *et al.* [211]	2021	Seismic Inversion		✓	
Yu and Ma [2]	2021	Seismic Inversion		✓	
Willard *et al.* [213]	2020	Inverse Problems			✓
Karniadakis *et al.* [214]	2021	Inverse Problems			✓
Cuomo *et al.* [215]	2022	Inverse Problems			✓
Yu *et al.* [164]	2022	Inverse Problems			✓
Banerjee *et al.* [216]	2023	Computational Imaging			✓
Kamilov *et al.* [217]	2023	Computational Imaging			✓
Lin *et al.* [3]	2023	Seismic Inversion			✓
Schuster *et al.* [219]	2024	Seismic Inversion			✓

models and seismic data. In contrast, $\mathbb{E}^{\mathbf{FWI}}$ encompasses 8 distinct datasets. Notably, the seismic dataset within $\mathbb{E}^{\mathbf{FWI}}$ includes both vertical and horizontal components, providing a more comprehensive view of the seismic information. Additionally, the velocity models in $\mathbb{E}^{\mathbf{FWI}}$ incorporate both P-wave and S-wave velocities, offering a richer dataset for waveform inversion studies. Both of these valuable datasets can be accessed through the following URLs: https://openfwi-lanl.github.io/ for OpenFWI and https://efwi-lanl.github.io/ for $\mathbb{E}^{\mathbf{FWI}}$. The source code for both InversionNet and VelocityGAN can be accessed on the GitHub repository at https://github.com/lanl/OpenFWI, and to facilitate researchers in their learning process, a comprehensive Colab Tutorial is additionally made available for convenient access via this link: https://colab.research.google.com/drive/17s5JmVs9ABl8MpmFlhWMSslj9_d5Atfx?usp=sharing.

- **Acoustic and Industrial Ultrasound.** In industrial settings, events such as crack propagation, shocks, impacts, or other events generate Acoustic Emission (AE) signals, which can be measured via passive listening. In Ref. [221], acoustic measurements were collected on bolted joints to detect events where the bolts were untightened, which resulted in AE signals. The data set, ORION-AE, containing the time-series measurements can be accessed via https://github.com/emmanuelramasso/ORION_AE_acoustic_emission_multisensor_datasets_bolts_loosening. Stiller et al. utilizes impact based AE measurements to identify damage modes in composites under compression. Analysis software and datasets can be accessed via https://github.com/DominikStiller/tudelft-damage-identification. Active interrogation is also a popular method for detecting defects or damage in industrial structures. In Ref. [222], a CNN is used to detect cracks based on acoustic phased-array measurements. The source code and dataset can be accessed via https://github.com/iikka-v/ML-NDT. Ref. [223] provides a finite element method simulation package to simulate acoustic NDT measurements based on Pulse-echo, Through-Transmission, and Linear Scanning. The source code to generate synthetic data can be accessed via https://github.com/mmolero/SimNDT. In addition to industrial measurements, there has been a push to classify sounds found commonly in everyday life, such as cars, animal calls, construction, music, etc. Google has extracted 10-second audio clips from YouTube videos to compile AudioSet, a labeled data set with 632 distinct event classes that is accessible via http://research.google.com/audioset/index.html. In Ref. [224] New York University presents the UrbanSound8k dataset containing 8732 4-second audio clips with labels of events common in urban environments. This dataset can be accessed via https://urbansounddataset.weebly.com/urbansound8k.html.
- **Medical Ultrasound Tomography.** In Refs. [76], [225], the authors develop a three-dimensional anatomically realistic numerical phantom of the female breast and a high-fidelity three-dimensional imaging model of ring-array USCT breast ultrasound. The goal of the generated numerical breast phantoms (NBPs) and corresponding simulated measurements is to provide a dataset to 1) support the development and assessment (using objective measurement of image quality) of model-based and learned image reconstruction methods and 2) conduct virtual imaging trials to guide the design of new USCT breast

imaging systems. Compared to other acoustic NBPs in the literature, the ones in Ref. [76] are particularly relevant to the development of new learning-based USCT image reconstruction method since they 1) comprise realistic structures and acoustic properties; 2) include lesions and/or other pathologies; and 3) are representative of the stochastic variability in breast size, shape, composition, anatomy, and tissue properties observed in a specified cohort of to-be-imaged subjects. Leveraging tools developed and released by the Virtual Imaging Clinical Trials for Regulatory Evaluation (VICTRE) project [226], [227] of the Food and Drug Administration (FDA), the NBPs in Ref. [76] correspond to the four different levels of breast density defined according to the American College of Radiology's (ACR) Breast Imaging Reporting and Data System (BI-RADS) [228]: A) Breast is almost entirely fat, B) Breast has scattered areas of fibroglandular density, C) Breast is heterogeneously dense, and D) Breast is extremely dense. Each NBP is a 3D voxelized map consisting of ten tissue types: fat, skin, glandular, nipple, ligament (connective tissue), muscle, terminal duct lobular unit, duct, artery, and vein. In the framework of the authors, large ensembles of stochastic NBPs with realistic variability in breast volume, shape, fraction of glandular tissue, ligament orientation, tissue anatomy, can be generated by controlling input parameters and selecting the random seed number. A variety of lesions (e.g., circumscribed or spiculated masses) can also be inserted at physiologically plausible locations. Tissue-specific acoustic properties (density, SOS, and AA) are then stochastically assigned to each tissue structure within physiological ranges and acoustic heterogeneity within fatty and glandular tissues is also modeled as spatially correlated random fields. Realization of these numerical phantoms and corresponding simulated measurements can be downloaded from Refs. [229]–[231], and additional NBPs can be generated using the open-source software in Ref. [232]. [233] presents a large-scale, anatomically realistic ultrasound dataset designed to benchmark neural solvers for wave equations. Featuring over 16 million simulations across diverse breast phantoms, it enables evaluation of neural operators in both forward and inverse tasks under clinically relevant conditions. The dataset addresses scalability, realism, and generalization gaps, and is publicly available to support reproducible research in neural wave-based imaging. Last but not least, [234] introduces the first large-scale open dataset specifically designed for limited-view prostate USCT. It provides over 280,000 paired samples of realistic 2D speed-of-sound phantoms and corresponding full-waveform ultrasound data, derived from anatomically accurate 3D prostate models based on clinical MRI/CT and expert annotations. This dataset addresses a critical gap in prostate cancer imaging research, enabling development and benchmarking of neural inversion methods under realistic limited-angle conditions. Baseline experiments show that while deep learning significantly outperforms traditional physics-based methods in both speed and accuracy, there remains room for improvement before achieving clinical-grade resolution.

Appendix E
List of Acronyms

For the convenience of the reader, this appendix provides a list of acronyms used throughout the manuscript. Each term is defined below to ensure clarity and consistency.

ADMM	Alternating Direction Method of Multipliers
AE	Autoencoder
AI	Artificial Intelligence
CNN	Convolutional Neural Network
CT	Computed Tomography
CWI	Computational Wave Imaging
EFWI	Elastic Full Waveform Inversion
FCN	Fully Convolutional Network
FNO	Fourier Neural Operator
FWI	Full Waveform Inversion
FWIGAN	Full Waveform Inversion Generative Adversarial Network
GAN	Generative Adversarial Network
KL	Kullback-Leibler
MAE	Mean Absolute Error
MAP	Maximum A Posteriori
MCMC	Markov Chain Monte Carlo
ML	Machine Learning
ML-NDT	Machine Learning for Nondestructive Testing
MRI	Magnetic Resonance Imaging
MSE	Mean Squared Error
NDT	Nondestructive Testing
OOD	Out of Distribution
PDE	Partial Differential Equation
PINN	Physics-Informed Neural Network
PPP	Plug-and-Play Prior
PPP-CWI	Plug-and-Play Prior for Computational Wave Imaging
SDE	Stochastic Differential Equation
SNR	Signal-to-Noise Ratio
SOS	Speed of Sound
SSIM	Structural Similarity Index
SSL	Self-Supervised Learning
TV	Total Variation
UPFWI	Unsupervised Physics-Informed Full Waveform Inversion
UQ	Uncertainty Quantification
USCT	Ultrasound Computed Tomography
VAE	Variational Autoencoder

References

[1] M. Araya-Polo, J. Jennings, A. Adler, and T. Dahlke, "Deep-learning tomography," *The Leading Edge*, vol. 37, no. 1, pp. 58–66, 2018.

[2] X. Yu and J. Ma, "Deep learning for geophysics: Current and future trends," *Reviews of Geophysics*, vol. 59, p. e2021RG000742, 2021.

[3] Y. Lin, J. Theiler, and B. Wohlberg, "Physics-guided data-driven seismic inversion: Recent progress and future opportunities in full waveform inversion," *IEEE Signal Processing Magazine*, vol. 40, pp. 115–133, 2023.

[4] X. Wang, J. Li, D. Wang, X. Huang, L. Liang, Z. Tang, Z. Fan, and Y. Liu, "Sparse ultrasonic guided wave imaging with compressive sensing and deep learning," *Mechanical Systems and Signal Processing*, vol. 178, p. 109346, 2022.

[5] S. Ryu, S.-H. Park, and K.-Y. Jhang, "Plastic properties estimation of aluminum alloys using machine learning of ultrasonic and eddy current data," *NDT & E International*, vol. 137, p. 102857, 2023.

[6] J. Rao, F. Yang, H. Mo, S. Kollmannsberger, and E. Rank, "Quantitative reconstruction of defects in multi-layered bonded composites using fully convolutional network-based ultrasonic inversion," *Journal of Sound and Vibration*, vol. 542, p. 117418, 2023.

[7] X. Liu and M. Almekkawy, "Ultrasound computed tomography using physical-informed neural network," in *2021 IEEE International Ultrasonics Symposium (IUS)*, 2021, pp. 1–4.

[8] A. Stanziola, S. Arridge, B. T. Cox, and B. E. Treeby, "A learned Born series for highly-scattering media," *JASA Express Letters*, vol. 3, no. 5, 2023.

[9] L. Lozenski, H. Wang, F. Li, M. Anastasio, B. Wohlberg, Y. Lin, and U. Villa, "Learned full waveform inversion incorporating task information for ultrasound computed tomography," *IEEE Transactions on Computational Imaging*, vol. 10, pp. 69–82, 2024.

[10] Y. Feng, Y. Chen, P. Jin, S. Feng, and Y. Lin, "Auto-linear phenomenon in subsurface imaging," in *The Forty-first International Conference on Machine Learning (ICML)*, 2024.

[11] P. Jin, X. Zhang, Y. Chen, S. Huang, Z. Liu, and Y. Lin, "Unsupervised learning of full-waveform inversion: Connecting CNN and partial differential equation in a loop," in *The Tenth International Conference on Learning Representations (ICLR)*, 2022.

[12] Y. Chen, X. Dai, D. Chen, M. Liu, L. Yuan, Z. Liu, and Y. Lin, "Image as first-order norm+linear autoregression: Unveiling mathematical invariance," *arXiv preprint*, 2023.

[13] G. Yao, N. da Silva, M. Warner, D. Wu, and C. Yang, "Tackling cycle skipping in full-waveform inversion with intermediate data," *Geophysics*, vol. 84, no. 3, pp. R411–R427, 2019.

[14] J. Virieux and S. Operto, "An overview of full-waveform inversion in exploration geophysics," *Geophysics*, vol. 74, no. 6, pp. WCC1–WCC26, 2009.

[15] J. Tromp, "Seismic wavefield imaging of earths interior across scales," *Nature Review Earth and Environment*, vol. 1, pp. 40–53, 2020.

[16] N. Ruiter, M. Zapf, T. Hopp, and H. Gemmeke, *Ultrasound Tomography*, J. Mamou and M. Oelze, Eds. Springer, 2023.

[17] R. Sigrist, J. Liau, A. E. Kaffas, M. Chammas, and J. Willmann, "Ultrasound Elastography: review of techniques and clinical applications," *Theranostics*, vol. 7, pp. 1303–1329, 2017.

[18] W. A. Mulder and R.-E. Plessix, "A comparison between one-way and two-way wave-equation migration," *Geophysics*, vol. 69, no. 6, pp. 1491–1504, 2004.

[19] Y. Liu and M. K. Sen, "A new time–space domain high-order finite-difference method for the acoustic wave equation," *Journal of computational Physics*, vol. 228, no. 23, pp. 8779–8806, 2009.

[20] A. R. Levander, "Fourth-order finite-difference p-sv seismograms," *Geophysics*, vol. 53, no. 11, pp. 1425–1436, 1988.

[21] T. Alkhalifah, "An acoustic wave equation for anisotropic media," *Geophysics*, vol. 65, no. 4, pp. 1239–1250, 2000.

[22] J. O. Blanch, J. O. Robertsson, and W. W. Symes, "Modeling of a constant q; methodology and algorithm for an efficient and optimally inexpensive viscoelastic technique," *Geophysics*, vol. 60, no. 1, pp. 176–184, 1995.

[23] J. O. Blanch and W. W. Symes, "Efficient iterative viscoacoustic linearized inversion," in *SEG Technical Program Expanded Abstracts 1995*, 1995, pp. 627–630.

[24] E. Duveneck, P. Milcik, P. M. Bakker, and C. Perkins, "Acoustic vti wave equations and their application for anisotropic reverse-time migration," in *SEG technical program expanded abstracts 2008*, 2008, pp. 2186–2190.

[25] M. A. Meyers and K. K. Chawla, *Mechanical behavior of materials*. Cambridge university press, 2008.

[26] K. R. Kelly, R. W. Ward, S. Treitel, and R. M. Alford, "Synthetic seismograms: A finite-difference approach," *Geophysics*, vol. 41, no. 1, pp. 2–27, 1976.

[27] P. Moczo, J. O. Robertsson, and L. Eisner, "The finite-difference time-domain method for modeling of seismic wave propagation," *Advances in geophysics*, vol. 48, pp. 421–516, 2007.

[28] J. Virieux, "SH-wave propagation in heterogeneous media: Velocity-stress finite-difference method," *Geophysics*, vol. 49, no. 11, pp. 1933–1942, 1984.

[29] ——, "P-SV wave propagation in heterogeneous media: Velocity-stress finite-difference method," *Geophysics*, vol. 51, no. 4, pp. 889–901, 1986.

[30] R. W. Graves, "Simulating seismic wave propagation in 3D elastic media using staggered-grid finite differences," *Bulletin of the seismological society of America*, vol. 86, no. 4, pp. 1091–1106, 1996.

[31] R. L. Kuhlemeyer and J. Lysmer, "Finite element method accuracy for wave propagation problems," *Journal of the Soil Mechanics and Foundations Division*, vol. 99, no. 5, pp. 421–427, 1973.

[32] J. D. De Basabe and M. K. Sen, "New developments in the finite-element method for seismic modeling," *The Leading Edge*, vol. 28, no. 5, pp. 562–567, 2009.

[33] D. Komatitsch, G. Erlebacher, D. Göddeke, and D. Michéa, "High-order finite-element seismic wave propagation modeling with mpi on a large gpu cluster," *Journal of computational physics*, vol. 229, no. 20, pp. 7692–7714, 2010.

[34] D. D. Kosloff and E. Baysal, "Forward modeling by a fourier method," *Geophysics*, vol. 47, no. 10, pp. 1402–1412, 1982.

[35] B. Fornberg, "The pseudospectral method; accurate representation of interfaces in elastic wave calculations," *Geophysics*, vol. 53, no. 5, pp. 625–637, 1988.

[36] M. Tabei, T. D. Mast, and R. C. Waag, "A k-space method for coupled first-order acoustic propagation equations," *The Journal of the Acoustical Society of America*, vol. 111, no. 1, pp. 53–63, 2002.

[37] B. T. Cox, S. Kara, S. R. Arridge, and P. C. Beard, "k-space propagation models for acoustically heterogeneous media: Application to biomedical photoacoustics," *The Journal of the Acoustical Society of America*, vol. 121, no. 6, pp. 3453–3464, 2007.

[38] K. Firouzi, B. Cox, B. Treeby, and N. Saffari, "A first-order k-space model for elastic wave propagation in heterogeneous media," *The Journal of the Acoustical Society of America*, vol. 132, no. 3, pp. 1271–1283, 2012.

[39] D. Komatitsch and J. Tromp, "Spectral-element simulations of global seismic wave propagation I. validation," *Geophysical Journal International*, vol. 149, no. 2, pp. 390–412, 2002.

[40] ——, "Spectral-element simulations of global seismic wave propagation II. three-dimensional models, oceans, rotation and self-gravitation," *Geophysical Journal International*, vol. 150, no. 1, pp. 303–318, 2002.

[41] D. Komatitsch, S. Tsuboi, J. Tromp, A. Levander, and G. Nolet, "The spectral-element method in seismology," *Geophysical Monograph-American Geophysical Union*, vol. 157, p. 205, 2005.

[42] P. Kudela, A. Żak, M. Krawczuk, and W. Ostachowicz, "Modelling of wave propagation in composite plates using the time domain spectral element method," *Journal of Sound and Vibration*, vol. 302, no. 4-5, pp. 728–745, 2007.

[43] Y. Lin and L. Huang, "Ultrasound waveform tomography with a modified total-variation regularization scheme," in *Medical Imaging 2013: Ultrasonic Imaging, Tomography, and Therapy*, vol. 8675, 2013, pp. 379–387.

[44] ——, "Ultrasound waveform tomography with a spatially variant regularization scheme," in *Medical Imaging 2014: Ultrasonic Imaging and Tomography*, vol. 9040, 2014, pp. 421–427.

[45] ——, "Acoustic- and elastic-waveform inversion using a modified Total-Variation regularization scheme," *Geophysical Journal International*, vol. 200, pp. 489–502, 2015.

[46] ——, "Quantifying subsurface geophysical properties changes using double-difference seismic-waveform inversion with a modified total-variation regularization scheme," *Geophysical Journal International*, vol. 203, no. 3, pp. 2125–2149, 11 2015.

[47] L. Rudin, S. Osher, and E. Fatemi, "Nonlinear Total Variation based noise removal algorithms," *Physica D.*, vol. 60, pp. 259–268, 1992.

[48] H. Aghamiry, A. Gholami, and S. Operto, "Full waveform inversion by proximal newton method using adaptive regularization," *Geophysical Journal International*, vol. 224, pp. 169–180, 2020.

[49] M. Kalita, V. Kazei, Y. Choi, and T. Alkhalifah, "Regularized full-waveform inversion with automated salt flooding," *Geophysics*, vol. 84, no. 4, pp. R569–R582, 2019.

[50] K. Aghazade and A. Gholami, "Robust acoustic and elastic full waveform inversion by adaptive tikhonov-tv regularization," 2025. [Online]. Available: https://arxiv.org/abs/2505.04022

[51] Y. Wu and Y. Lin, "InversionNet: An efficient and accurate data-driven full waveform inversion," *IEEE Transactions on Computational Imaging*, vol. 6, pp. 419–433, 2019.

[52] F. Yang and J. Ma, "Deep-learning inversion: A next-generation seismic velocity model building method," *Geophysics*, vol. 84, no. 4, pp. R583–R599, 2019.

[53] J. Rao, F. Yang, H. Mo, S. Kollmannsberger, and E. Rank, "Quantitative reconstruction of defects in multi-layered bonded composites using fully convolutional network-based ultrasonic inversion," *Journal of Sound and Vibration*, vol. 542, p. 117418, 2023.

[54] L. Azevedo, "Model reduction in geostatistical seismic inversion with functional data analysis," *Geophysics*, vol. 87, no. 1, pp. M1–M11, 2022.

[55] O. Ronneberger, P. Fischer, and T. Brox, "U-net: Convolutional networks for biomedical image segmentation," in *Medical image computing and computer-assisted intervention–MICCAI 2015*, 2015, pp. 234–241.

[56] H. Sun, Y. Sun, R. Nammourand, C. Rivera, P. Williamson, and L. Demanet, "Learning with real data without real labels: a strategy for extrapolated full-waveform inversion with field data," *Geophysical Journal International*, vol. 235, p. 17611777, 2023.

[57] Y. Li, M. Karrenbach, and J. Ajo-Franklin, *Distributed acoustic sensing in geophysics: Methods and applications*. John Wiley & Sons, 2022, vol. 268.

[58] R. Rojas-Gómez, J. Yang, Y. Lin, J. Theiler, and B. Wohlberg, "Physics-consistent data-driven waveform inversion with adaptive data augmentation," *IEEE Geoscience and Remote Sensing Letters*, vol. 19, pp. 1–5, 2022.

[59] B. Sun and T. Alkhalifah, "ML-misfit: A neural network formulation of the misfit function for full-waveform inversion," *Frontiers in Earth Science*, vol. 10, p. 1011825, 2022.

[60] S. Feng, P. Jin, X. Zhang, Y. Chen, D. Alumbaugh, M. Commer, and Y. Lin, "Extremely weak supervision inversion of multiphysical properties," in *Second International Meeting for Applied Geoscience & Energy*. Society of Exploration Geophysicists and American Association of Petroleum, 2022, pp. 1785–1789.

[61] A. Cai, H. Qiu, and F. Niu, "Semi-supervised surface wave tomography with wasserstein cycle-consistent GAN: method and application to southern california plate boundary region," *Journal of Geophysical Research: Solid Earth*, vol. 127, no. 3, p. e2021JB023598, 2022.

[62] O. M. Saad, R. Harsuko, and T. Alkhalifah, "SiameseFWI: a deep learning network for enhanced full waveform inversion," *Journal of Geophysical Research: Machine Learning and Computation*, vol. 1, no. 3, p. e2024JH000227, 2024.

[63] M. Wang, S. Xu, and H. Zhou, "Self-supervised learning for low frequency extension of seismic data," in *SEG International Exposition and Annual Meeting*, 2020.

[64] S. Cheng, Y. Wang, Q. Zhang, R. Harsuko, and T. Alkhalifah, "A self-supervised learning framework for seismic low-frequency extrapolation," *Journal of Geophysical Research: Machine Learning and Computation*, vol. 1, no. 3, p. e2024JH000157, 2024.

[65] N. Cui, T. Lei, and W. Zhang, "Low-frequency reconstruction for full waveform inversion by unsupervised learning," *Earth and Space Science*, vol. 11, no. 11, p. e2024EA003565, 2024.

[66] J. Sun, K. Innanen, T. Zhang, and D. Trad, "Implicit seismic full waveform inversion with deep neural representation," *Journal of Geophysical Research: Solid Earth*, vol. 128, p. e2022JB025964, 2023.

[67] Q. He and Y. Wang, "Reparameterized full-waveform inversion using deep neural networks," *Geophysics*, vol. 86, no. 1, pp. V1–V13, 2021.

[68] A. Jia, J. Sun, B. Du, and Y. Lin, "Seismic full waveform inversion with uncertainty analysis using unsupervised variational deep learning," *IEEE Transactions on Geoscience and Remote Sensing*, vol. 63, pp. 1–16, 2025.

[69] Y. Jiang, J. Ma, J. Ning, J. Li, H. Wu, and T. Bao, "One-fit-all transformer for multimodal geophysical inversion: Method and application," *Journal of Geophysical Research: Machine Learning and Computation*, vol. 2, no. 1, p. e2024JH000432, 2025.

[70] M. Zhu, S. Feng, Y. Lin, and L. Lu, "Fourier-DeepONet: Fourier-enhanced deep operator networks for full waveform inversion with improved accuracy, generalizability, and robustness," *Computer Methods in Applied Mechanics and Engineering*, vol. 416, p. 116300, 2023.

[71] L. Lu, P. Jin, G. Pang, Z. Zhang, and G. E. Karniadakis, "Learning nonlinear operators via DeepONet based on the universal approximation theorem of operators," *Nature Machine Intelligence*, vol. 3, pp. 218–229, 2021.

[72] G. Wen, Z. Li, K. Azizzadenesheli, A. Anandkumar, and S. M. Benson, "U-FNOan enhanced fourier neural operator-based deep-learning model for multiphase flow," *Advances in Water Resources*, vol. 163, p. 104180, 2022.

[73] Q. Zeng, S. Feng, B. Wohlberg, and Y. Lin, "InversionNet3D: Efficient and scalable learning for 3-D full-waveform inversion," *IEEE Transactions on Geoscience and Remote Sensing*, vol. 60, pp. 1–16, 2022.

[74] Y. Yang, X. Zhang, Q. Guan, and Y. Lin, "Making invisible visible: Data-driven seismic inversion with spatio-temporally constrained data augmentation," *IEEE Transactions on Geoscience and Remote Sensing*, vol. 60, 2022.

[75] R. W. Donaldson and J. He, "Instantaneous ultrasound computed tomography using deep convolutional neural networks," in *Health Monitoring of Structural and Biological Systems XV*, vol. 11593. SPIE, 2021, pp. 396–405.

[76] F. Li, U. Villa, S. Park, and M. A. Anastasio, "3-D stochastic numerical breast phantoms for enabling virtual imaging trials of ultrasound computed tomography," *IEEE Transactions on Ultrasonics, Ferroelectrics, and Frequency Control*, vol. 69, no. 1, pp. 135–146, 2022.

[77] G. Jeong, F. Li, U. Villa, and M. A. Anastasio, "A deep-learning-based image reconstruction method for USCT that employs multimodality inputs," in *Medical Imaging 2023: Ultrasonic Imaging and Tomography*, C. Boehm and N. Bottenus, Eds., vol. 12470, 2023, p. 124700M.

[78] G. Jeong, F. Li, T. Mitcham, N. Duric, U. Villa, and M. A. Anastasio, "Investigating the use of traveltime and reflection tomography for deep learning-based sound-speed estimation in ultrasound computed tomography," *IEEE Transactions on Ultrasonics, Ferroelectrics, and Frequency Control*, vol. early access, 2024.

[79] A. Rachman, T. Zhang, and C. Ratnayake, "Applications of machine learning in pipeline integrity management: A state-of-the-art review," *International journal of pressure vessels and piping*, vol. 193, p. 104471, 2021.

[80] C.-C. Sergio, P. D. Wilcox, and A. J. Croxford, "Deep learning in automated ultrasonic NDE developments, axioms and opportunities," *NDT & E International*, vol. 131, p. 102703, 2022.

[81] Z. Zhang and Y. Lin, "Data-driven seismic waveform inversion: A study on the robustness and generalization," *IEEE Transactions on Geoscience and Remote sensing*, vol. 58, no. 10, pp. 6900–6913, 2020.

[82] S. Feng, Y. Lin, and B. Wohlberg, "Multiscale data-driven seismic full-waveform inversion with field data study," *IEEE Transactions on Geoscience and Remote Sensing*, vol. 60, pp. 1–14, 2021.

[83] K. H. Jin, M. McCann, E. Froustey, and M. Unser, "Deep Convolutional Neural Network for Inverse Problems in Imaging," *IEEE Transactions on Image Processing*, vol. 26, no. 9, pp. 4509–4522, 2017.

[84] M. Rasht-Behesht, C. Huber, K. Shukla, and G. Em Karniadakis, "Physics-informed neural networks (PINNs) for wave propagation and full waveform inversions," *Journal of Geophysical Research: Solid Earth*, vol. 127, p. e2021JB023120, 2022.

[85] Y. Ren, X. Xu, S. Yang, L. Nie, and Y. Chen, "A physics-based neural-network way to perform seismic full waveform inversion," *IEEE Access*, vol. 8, pp. 112 266 – 112 277, 2020.

[86] N. Gupta, "Solving forward and inverse problems for seismic imaging using invertible neural networks," Virginia Tech, Tech. Rep., 2023.

[87] B. Liu, P. Jiang, Q. Wang, Y. Ren, S. Yang, and A. Cohn, "Physics-driven self-supervised learning system for seismic velocity inversion," *Geophysics*, vol. 88, no. 2, pp. R145–R161, 2023.

[88] F. Yang and J. Ma, "FWIGAN: Full-waveform inversion via a physics-informed generative adversarial network," *Journal of Geophysical Research: Solid Earth*, vol. 128, no. 4, p. e2022JB025493, 2023.

[89] A. Dhara and M. Sen, "Elastic full-waveform inversion using a physics-guided deep convolutional encoderdecoder," *IEEE Transactions on Geoscience and Remote Sensing*, vol. 61, 2023.

[90] M. Raissi, P. Perdikaris, and G. Karniadakis, "Physics-informed neural networks: A deep learning framework for solving forward and inverse problems involving nonlinear partial differential equations," *Journal of Computational Physics*, vol. 378, pp. 686 – 707, 2019.

[91] A. Dhara and M. Sen, "Physics-guided deep autoencoder to overcome the need for a starting model in full-waveform inversion," *The Leading Edge*, vol. 41, pp. 375–381, 2022.

[92] W. Zhu, K. Xu, E. Darve, B. Biondi, and G. Beroza, "Integrating deep neural networks with full-waveform inversion: Reparameterization, regularization, and uncertainty quantification," *Geophysics*, vol. 87, no. 1, pp. R93–R109, 2022.

[93] D. Ulyanov, A. Vedaldi, and V. Lempitsky, "Deep image prior," in *Proceedings of the IEEE conference on computer vision and pattern recognition*, 2018, pp. 9446–9454.

[94] Y. Wu and G. A. McMechan, "Parametric convolutional neural network-domain full-waveform inversion," *Geophysics*, vol. 84, no. 6, pp. R881–R896, 2019.

[95] B. Zhang and L. Wang, "Progressive plug and play full waveform inversion with multitask learning," *Scientific Reports*, vol. 15, no. 19805, 2025.

[96] S. V. Venkatakrishnan, C. A. Bouman, and B. Wohlberg, "Plug-and-play priors for model based reconstruction," in *IEEE Global Conf. Signal Process. and Inf. Process. (GlobalSIP)*, 2013, pp. 945–948.

[97] S. Sreehari, S. V. Venkatakrishnan, B. Wohlberg, G. T. Buzzard, L. F. Drummy, J. P. Simmons, and C. A. Bouman, "Plug-and-play priors for bright field electron tomography and sparse interpolation," *IEEE Trans. Comp. Imag.*, vol. 2, no. 4, pp. 408–423, Dec. 2016.

[98] U. Kamilov, C. A. Bouman, G. T. Buzzard, and B. Wohlberg, "Plug-and-play methods for integrating physical and learned models in computational imaging," *IEEE Signal Processing Magazine*, vol. 40, no. 1, pp. 85–97, Jan. 2023.

[99] K. Dabov, A. Foi, V. Katkovnik, and K. Egiazarian, "Image denoising by sparse 3-D transform-domain collaborative filtering," *IEEE Transactions on Image Processing*, vol. 16, no. 8, pp. 2080–2095, 2007.

[100] K. Zhang, W. Zuo, Y. Chen, D. Meng, and L. Zhang, "Beyond a Gaussian denoiser: Residual learning of deep CNN for image denoising," *IEEE Transactions on Image Processing*, vol. 26, no. 7, pp. 3142–3155, 2017.

[101] N. Parikh, S. Boyd *et al.*, "Proximal algorithms," *Foundations and trends in Optimization*, vol. 1, no. 3, pp. 127–239, 2014.

[102] R. Glowinski and A. Marroco, "Sur l'approximation, par elements finis d'ordre un, et la resolution, par penalisation-dualite d'une classe de problemes de dirichlet non lineaires," *ESAIM: Mathematical Modelling and Numerical Analysis-Modélisation Mathématique et Analyse Numérique*, vol. 9, no. R2, pp. 41–76, 1975.

[103] D. Gabay and B. Mercier, "A dual algorithm for the solution of nonlinear variational problems via finite element approximation," *Computers & Mathematics with Applications*, vol. 2, no. 1, pp. 17–40, 1976.

[104] S. Boyd, N. Parikh, E. Chu, B. Peleato, and J. Eckstein, "Distributed optimization and statistical learning via the alternating direction method of multipliers," *Foundations and Trends in Machine Learning*, vol. 3, no. 1, 2011.

[105] A. Beck, *First-Order Methods in Optimization*, ser. MOS-SIAM Series on Optimization. SIAM, 2017.

[106] S. H. Chan, X. Wang, and O. A. Elgendy, "Plug-and-play ADMM for image restoration: Fixed-point convergence and applications," *IEEE Trans. Comp. Imag.*, vol. 3, no. 1, pp. 84–98, Mar. 2017.

[107] E. Ryu, J. Liu, S. Wang, X. Chen, Z. Wang, and W. Yin, "Plug-and-play methods provably converge with properly trained denoisers," in *Proceedings of the 36th International Conference on Machine Learning*, K. Chaudhuri and R. Salakhutdinov, Eds., vol. 97. PMLR, Jun. 2019, pp. 5546–5557. [Online]. Available: https://proceedings.mlr.press/v97/ryu19a.html

[108] K. Zhang, Y. Li, W. Zuo, L. Zhang, L. Van Gool, and R. Timofte, "Plug-and-Play image restoration with deep denoiser prior," *IEEE Transactions on Pattern Analysis and Machine Intelligence*, vol. 44, no. 10, pp. 6360–6376, 2022.

[109] H. Aghamiry, A. Gholami, and S. Operto, "Full waveform inversion by proximal newton method using adaptive regularization," *Geophysical Journal International*, vol. 224, 2020.

[110] H. Fu, L. Yang, and X. Miao, "An efficient plug-and-play regularization method for full waveform inversion," *Journal of Geophysics and Engineering*, vol. 20, no. 6, pp. 1140–1149, 2023.

[111] M. Izzatullah, T. Alkhalifah, J. Romero, M. Corrales, N. Luiken, and M. Ravasi, "Plug-and-Play stein variational gradient descent for bayesian post-stack seismic inversion," in *84th EAGE Annual Conference & Exhibition*, 2023, p. 15.

[112] N. Tagasovska and D. Lopez-Paz, "Single-model uncertainties for deep learning," in *Advances in Neural Information Processing Systems 33*, 2019.

[113] A. Tarantola, *Inverse Problem Theory and Methods for Model Parameter Estimation*. Philadelphia, PA: SIAM, 2005.

[114] J. Kaipio and E. Somersalo, *Statistical and Computational Inverse Problems*, ser. Applied Mathematical Sciences. New York: Springer-Verlag, 2005, vol. 160.

[115] A. M. Stuart, "Inverse problems: A Bayesian perspective," *Acta Numerica*, vol. 19, pp. 451–559, 2010.

[116] J. T. Oden, R. M. Moser, and O. Ghattas, "Computer predictions with quantified uncertainty, Parts I & II," *SIAM News*, vol. 43, no. 9&10, 2010.

[117] L. Biegler, G. Biros, O. Ghattas, Y. Marzouk, M. Heinkenschloss, D. Keyes, B. Mallick, L. Tenorio, B. van Bloemen Waanders, and K. Willcox, Eds., *Large-scale Inverse Problems and Quantification of Uncertainty*. Wiley, 2011.

[118] J. Martin, L. C. Wilcox, C. Burstedde, and O. Ghattas, "A stochastic Newton MCMC method for large-scale statistical inverse problems with application to seismic inversion," *SIAM Journal on Scientific Computing*, vol. 34, no. 3, pp. A1460–A1487, 2012.

[119] T. Bui-Thanh, O. Ghattas, J. Martin, and G. Stadler, "A computational framework for infinite-dimensional Bayesian inverse problems Part I: The linearized case, with application to global seismic inversion," *SIAM Journal on Scientific Computing*, vol. 35, no. 6, pp. A2494–A2523, 2013.

[120] I. E. Ulrich, C. Boehm, A. Zunino, and A. Fichtner, "Analyzing resolution and model uncertainties for ultrasound computed tomography using Hessian information," in *Medical Imaging 2022: Ultrasonic Imaging and Tomography*, N. Bottenus and N. V. Ruiter, Eds., vol. 12038. International Society for Optics and Photonics, 2022, p. 120380A. [Online]. Available: https://doi.org/10.1117/12.2608546

[121] O. Bates, L. Guasch, G. Strong, T. C. Robins, O. Calderon-Agudo, C. Cueto, J. Cudeiro, and M. Tang, "A probabilistic approach to tomography and adjoint state methods, with an application to full waveform inversion in medical ultrasound," *Inverse Problems*, vol. 38, no. 4, p. 045008, 2022.

[122] D. M. Blei, A. Kucukelbir, and J. D. McAuliffe, "Variational inference: A review for statisticians," *Journal of the American Statistical Association*, vol. 112, no. 518, pp. 859–877, 2017.

[123] X. Zhang and A. Curtis, "Variational full-waveform inversion," *Geophysical Journal International*, vol. 222, no. 1, pp. 406–411, 04 2020. [Online]. Available: https://doi.org/10.1093/gji/ggaa170

[124] D. Rezende and S. Mohamed, "Variational inference with normalizing flows," in *International conference on machine learning*, 2015, pp. 1530–1538.

[125] G. Papamakarios, E. Nalisnick, D. J. Rezende, S. Mohamed, and B. Lakshminarayanan, "Normalizing flows for probabilistic modeling and inference," *Journal of Machine Learning Research*, vol. 22, no. 57, pp. 1–64, 2021.

[126] H. Sun and K. L. Bouman, "Deep probabilistic imaging: Uncertainty quantification and multi-modal solution characterization for computational imaging," in *Proceedings of the AAAI Conference on Artificial Intelligence*, vol. 35, no. 3, 2021, pp. 2628–2637.

[127] Y. Liu, X. Zhang, I. Tsvankin, and Y. Lin, "Enhanced prediction accuracy with uncertainty quantification in monitoring co2 sequestration using convolutional neural networks," *arXiv preprint arXiv:2212.04567*, 2023.

[128] E. Schankee Um, D. Alumbaugh, M. Commer, S. Feng, E. Gasperikova, Y. Li, Y. Lin, and S. Samarasinghe, "Deep-learning multiphysics network for imaging CO_2 saturation and estimating uncertainty in geological carbon storage," *Geophysical Prospecting*, vol. 72, no. Machine learning applications in geophysical exploration and monitoring, pp. 183–198, 2023.

[129] A. Yablokov, Y. Lugovtsova, and A. Serdyukov, "Uncertainty quantification of multimodal surface wave inversion using artificial neural networks," *Geophysics*, vol. 88, no. 2, pp. 1MA–Y5, 2023.

[130] G. Rizzuti, A. Siahkoohi, P. Witte, and F. Herrmann, "Parameterizing uncertainty by deep invertible networks: An application to reservoir characterization," in *SEG International Exposition and Annual Meeting*, 2020.

[131] A. Siahkoohi, G. Rizzuti, and F. Herrmann, "Deep Bayesian inference for seismic imaging with tasks," *Geophysics*, vol. 87, pp. 1SO–V558, 2022.

[132] F. Wang, X. Huang, and T. Alkhalifah, "A prior regularized full waveform inversion using generative diffusion models," *IEEE Transactions on Geoscience and Remote Sensing*, vol. 61, pp. 1–11, 2023.

[133] J. Yang, H. Wang, Y. Sheng, Y. Lin, and L. Yang, "Edgeo: A physics-guided generative ai toolkit for geophysical monitoring on edge devices," in *The Design Automation Conference (DAC)*, 2024.

[134] L. Mosser, O. Dubrule, and M. J. Blunt, "Stochastic seismic waveform inversion using generative adversarial networks as a geological prior," *Mathematical Geosciences*, vol. 52, no. 1, pp. 53–79, 2020.

[135] J. Yang, Y. Lin, and W. Jiang, "DiGiT: a diffusion-based modular geophysical toolkit platform a case study on on-device paired geophysical training data generation," *arXiv preprint*, 2024.

[136] D. Kingma and M. Welling, "Auto-encoding variational bayes," in *The International Conference on Learning Representations (ICLR)*, 2014.

[137] I. Goodfellow, J. Pouget-Abadie, M. Mirza, B. Xu, D. Warde-Farley, S. Ozair, A. Courville, and Y. Bengio, "Generative adversarial networks," in *The Advances in neural information processing systems (NeurIPS)*, 2014.

[138] N. Kodali, J. Abernethy, J. Hays, and Z. Kira, "On convergence and stability of GANs," *arXiv preprint arXiv:1705.07215*, 2017.

[139] A. Srivastava, L. Valkov, C. Russell, M. U. Gutmann, and C. Sutton, "Veegan: Reducing mode collapse in GANs using implicit variational

learning," *Advances in neural information processing systems*, vol. 30, 2017.

[140] Y. Yacoby, W. Pan, and F. Doshi-Velez, "Failure modes of variational autoencoders and their effects on downstream tasks," *arXiv preprint arXiv:2007.07124*, 2020.

[141] R. M. Neal *et al.*, "MCMC using hamiltonian dynamics," *Handbook of markov chain monte carlo*, vol. 2, no. 11, p. 2, 2011.

[142] J. Sohl-Dickstein, E. Weiss, N. Maheswaranathan, and S. Ganguli, "Deep unsupervised learning using nonequilibrium thermodynamics," in *The International Conference on Machine Learning (ICML)*, 2015.

[143] J. Ho, A. Jain, and P. Abbeel, "Denoising diffusion probabilistic models," in *The Advances in neural information processing systems (NeurIPS)*, 2020.

[144] Y. Song, L. Shen, L. Xing, and S. Ermon, "Solving inverse problems in medical imaging with score-based generative models," in *The Tenth International Conference on Learning Representations (ICLR)*, 2022.

[145] Y. Song, J. Sohl-Dickstein, D. P. Kingma, A. Kumar, S. Ermon, and B. Poole, "Score-based generative modeling through stochastic differential equations," in *International Conference on Learning Representations*, 2021. [Online]. Available: https://openreview.net/forum?id=PxTIG12RRHS

[146] T. Buscheck, K. Mansoor, X. Yang, H. Wainwright, and S. Carroll, "Downhole pressure and chemical monitoring for CO_2 and brine leak detection in aquifers above a CO_2 storage reservoir," *International Journal Greenhouse Gas Control*, vol. 91, p. 102812, 2019.

[147] X. Yang, T. Buscheck, K. Mansoor, Z. Wang, K. Gao, L. Huang, H. Wainwright, and S. Carroll, "Assessment of geophysical monitoring methods for detection of brine and CO_2 leakage in drinking water aquifers," *International Journal Greenhouse Gas Control*, vol. 90, p. 102803, 2019.

[148] Z. Zhou, Y. Lin, Z. Zhang, Y. Wu, Z. Wang, R. Dilmore, and G. Guthrie, "A data-driven CO_2 leakage detection using seismic data and spatial-temporal densely connected convolutional neural networks," *International Journal of Greenhouse Gas Control*, vol. 90, p. 102790, 2019.

[149] Z. Zhong, A. Y. Sun, and X. Wu, "Inversion of time-lapse seismic reservoir monitoring data using CycleGAN: A deep learning-based approach for estimating dynamic reservoir property changes," *Journal of Geophysical Research: Solid Earth*, vol. 125, no. 3, p. e2019JB018408, 2020.

[150] Z. X. Leong, T. Zhu, and A. Y. Sun, "Estimating CO_2 saturation maps from seismic data using deep convolutional neural networks," in *Second International Meeting for Applied Geoscience & Energy*. Society of Exploration Geophysicists and American Association of Petroleum, 2022, pp. 510–514.

[151] E. Schankee Um, D. Alumbaugh, Y. Lin, and S. Feng, "Real-time deep-learning inversion of seismic full waveform data for CO_2 saturation and uncertainty in geological carbon storage monitoring," *Geophysical Prospecting*, vol. 72, no. Machine learning applications in geophysical exploration and monitoring, pp. 199–212, 2023.

[152] X. Wang, M. Lin, J. Li, J. Tong, X. Huang, L. Liang, Z. Fan, and Y. Liu, "Ultrasonic guided wave imaging with deep learning: Applications in corrosion mapping," *Mechanical Systems and Signal Processing*, vol. 169, p. 108761, 2022.

[153] M. Rudolph, B. Wandt, and B. Rosenhahn, "Same same but DifferNet: Semi-supervised defect detection with normalizing flows," *Proceedings of the IEEE/CVF Winter Conference on Applications of Computer Vision*, p. 19071916, 2021.

[154] K. Shukla, P. Clark, B. James, D. Sparkman, and G. Karniadakis, "Physics-informed neural network for ultrasound nondestructive quantification of surface breaking cracks," *Journal of Nondestructive Evaluation*, vol. 39, pp. 1–20, 2020.

[155] N. Luiken and M. Ravasi, "A deep learning-based approach to increase efficiency in the acquisition of ultrasonic non-destructive testing datasets," *Proceedings of the IEEE/CVF Conference on Computer Vision and Pattern Recognition*, pp. 3094–3102, 2023.

[156] J. Greenhall, D. K. Zerkle, E. S. Davis, R. Broilo, and C. Pantea, "Measuring Thermal Profiles in High Explosives using Neural Networks," *arXiv*, Oct. 2023. [Online]. Available: http://arxiv.org/abs/2310.12260

[157] T. D. McGee, *Principles and Methods of Temperature Measurement*. John Wiley & Sons, May 1988, google-Books-ID: qfmS7g4JzjwC.

[158] G. Gaussorgues and S. Chomet, *Infrared Thermography*. Springer Science & Business Media, Dec. 1993, google-Books-ID: FRQOi-HeCXgMC.

[159] J. Lu, K. Wakai, S. Takahashi, and S. Shimizu, "Acoustic computer tomographic pyrometry for two-dimensional measurement of gases taking into account the effect of refraction of sound wave paths," *Measurement Science and Technology*, vol. 11, no. 6, pp. 692–697, Jun. 2000. [Online]. Available: https://iopscience.iop.org/article/10.1088/0957-0233/11/6/312

[160] K. Kudo, K. Mizutani, T. Akagami, and R. Murayama, "Temperature distribution in a rectangular space measured by a small number of transducers and reconstructed from reflected sounds," *Japanese Journal of Applied Physics*, vol. 42, no. Part 1, No. 5B, pp. 3189–3193, May 2003. [Online]. Available: https://iopscience.iop.org/article/10.1143/JJAP.42.3189

[161] K. Mizutani, S. Kawabe, I. Saito, and H. Masuyama, "Measurement of temperature distribution using acoustic reflector array," *Japanese Journal of Applied Physics*, vol. 45, no. 5B, pp. 4516–4520, May 2006. [Online]. Available: https://iopscience.iop.org/article/10.1143/JJAP.45.4516

[162] N. Modliski, P. Madejski, T. Janda, K. Szczepanek, and W. Kordylewski, "A validation of computational fluid dynamics temperature distribution prediction in a pulverized coal boiler with acoustic temperature measurement," *Energy*, vol. 92, pp. 77–86, Dec. 2015. [Online]. Available: https://www.sciencedirect.com/science/article/pii/S036054421500746X

[163] S. Zhang, G. Shen, L. An, and Y. Niu, "Online monitoring of the two-dimensional temperature field in a boiler furnace based on acoustic computed tomography," *Applied Thermal Engineering*, vol. 75, pp. 958–966, Jan. 2015. [Online]. Available: https://www.sciencedirect.com/science/article/pii/S1359431114009673

[164] Y. Yu, Q. Xiong, Z.-S. Ye, X. Liu, Q. Li, and K. Wang, "A review on acoustic reconstruction of temperature profiles: From time measurement to reconstruction algorithm," *IEEE Transactions on Instrumentation and Measurement*, vol. 71, pp. 1–24, 2022. [Online]. Available: https://ieeexplore.ieee.org/document/9872057/

[165] J. Schreiman, J. Gisvold, J. F. Greenleaf, and R. Bahn, "Ultrasound transmission computed tomography of the breast." *Radiology*, vol. 150, no. 2, pp. 523–530, 1984.

[166] R. G. Pratt, L. Huang, N. Duric, and P. Littrup, "Sound-speed and attenuation imaging of breast tissue using waveform tomography of transmission ultrasound data," in *Medical Imaging 2007: Physics of Medical Imaging*, vol. 6510. International Society for Optics and Photonics, 2007, p. 65104S.

[167] N. Duric, P. Littrup, L. Poulo, A. Babkin, R. Pevzner, E. Holsapple, O. Rama, and C. Glide, "Detection of breast cancer with ultrasound tomography: First results with the computed ultrasound risk evaluation (cure) prototype," *Medical physics*, vol. 34, no. 2, pp. 773–785, 2007.

[168] C. Li, N. Duric, P. Littrup, and L. Huang, "In vivo breast sound-speed imaging with ultrasound tomography," *Ultrasound in medicine & biology*, vol. 35, no. 10, pp. 1615–1628, 2009.

[169] K. Wang, T. Matthews, F. Anis, C. Li, N. Duric, and M. A. Anastasio, "Waveform inversion with source encoding for breast sound speed reconstruction in ultrasound computed tomography," *IEEE transactions on ultrasonics, ferroelectrics, and frequency control*, vol. 62, no. 3, pp. 475–493, 2015.

[170] J. F. Greenleaf, S. Johnson, R. C. Bahn, and B. Rajagopalan, "Quantitative cross-sectional imaging of ultrasound parameters." in *Ultrason Symp Proc*, 1977.

[171] P. L. Carson, C. R. Meyer, A. L. Scherzinger, and T. V. Oughton, "Breast imaging in coronal planes with simultaneous pulse echo and transmission ultrasound," *Science*, vol. 214, no. 4525, pp. 1141–1143, 1981.

[172] M. P. André, H. S. Janée, P. J. Martin, G. P. Otto, B. A. Spivey, and D. A. Palmer, "High-speed data acquisition in a diffraction tomography system employing large-scale toroidal arrays," *International Journal of Imaging Systems and Technology*, vol. 8, no. 1, pp. 137–147, 1997.

[173] K. Nam, J. A. Zagzebski, and T. J. Hall, "Quantitative assessment of in vivo breast masses using ultrasound attenuation and backscatter," *Ultrasonic imaging*, vol. 35, no. 2, pp. 146–161, 2013.

[174] G. Sandhu, C. Li, O. Roy, S. Schmidt, and N. Duric, "Frequency domain ultrasound waveform tomography: breast imaging using a ring transducer," *Physics in Medicine & Biology*, vol. 60, no. 14, p. 5381, 2015.

[175] B. Malik, J. Klock, J. Wiskin, and M. Lenox, "Objective breast tissue image classification using quantitative transmission ultrasound tomography," *Scientific reports*, vol. 6, p. 38857, 2016.

[176] N. Duric, P. Littrup, and C. Kuzmiak, "Breast ultrasound tomography," *Breast Imaging*, vol. 6, 2018.

[177] U. Taskin and K. W. van Dongen, "3D redatuming for breast ultrasound," in *Medical Imaging 2020: Physics of Medical Imaging*, vol.

11312. International Society for Optics and Photonics, 2020, p. 113125H.

[178] N. Duric, M. Sak, S. Fan, R. M. Pfeiffer, P. J. Littrup, M. S. Simon, D. H. Gorski, H. Ali, K. S. Purrington, R. F. Brem *et al.*, "Using whole breast ultrasound tomography to improve breast cancer risk assessment: a novel risk factor based on the quantitative tissue property of sound speed," *Journal of clinical medicine*, vol. 9, no. 2, p. 367, 2020.

[179] J. Wiskin, B. Malik, D. Borup, N. Pirshafiey, and J. Klock, "Full wave 3D inverse scattering transmission ultrasound tomography in the presence of high contrast," *Scientific Reports*, vol. 10, no. 1, pp. 1–14, 2020.

[180] A. Javaherian, F. Lucka, and B. T. Cox, "Refraction-corrected ray-based inversion for three-dimensional ultrasound tomography of the breast," *Inverse Problems*, vol. 36, no. 12, p. 125010, 2020.

[181] N. V. Ruiter, M. Zapf, T. Hopp, R. Dapp, E. Kretzek, M. Birk, B. Kohout, and H. Gemmeke, "3D ultrasound computer tomography of the breast: A new era?" *European Journal of Radiology*, vol. 81, pp. S133–S134, 2012.

[182] N. Duric, P. Littrup, O. Roy, S. Schmidt, C. Li, L. Bey-Knight, and X. Chen, "Breast imaging with ultrasound tomography: Initial results with softvue," in *2013 IEEE International Ultrasonics Symposium (IUS)*. IEEE, 2013, pp. 382–385.

[183] Z. Zhang, L. Huang, and Y. Lin, "Efficient implementation of ultrasound waveform tomography using source encoding," in *Medical Imaging 2012: Ultrasonic Imaging, Tomography, and Therapy*, vol. 8320. SPIE, 2012, pp. 22–31.

[184] F. Lucka, M. Pérez-Liva, B. E. Treeby, and B. T. Cox, "High resolution 3D ultrasonic breast imaging by time-domain full waveform inversion," *Inverse Problems*, vol. 38, no. 2, p. 025008, 2021.

[185] Y. Fan, H. Wang, H. Gemmeke, T. Hopp, and J. Hesser, "Model-data-driven image reconstruction with neural networks for ultrasound computed tomography breast imaging," *Neurocomputing*, vol. 467, pp. 10–21, 2022. [Online]. Available: https://www.sciencedirect.com/science/article/pii/S092523122101393X

[186] S. Bhadra, V. A. Kelkar, F. J. Brooks, and M. A. Anastasio, "On hallucinations in tomographic image reconstruction," *IEEE Transactions on Medical Imaging*, pp. 1–1, 2021.

[187] J. Poudel, L. A. Forte, and M. A. Anastasio, "Compensation of 3D-2D model mismatch in ultrasound computed tomography with the aid of convolutional neural networks (Conference Presentation)," in *Medical Imaging 2019: Ultrasonic Imaging and Tomography*, B. C. Byram and N. V. Ruiter, Eds., vol. 10955, 2019, p. 1095507. [Online]. Available: https://doi.org/10.1117/12.2512966

[188] F. Li, U. Villa, and M. A. Anastasio, "A learning-based method for compensating 3d-2d model mismatch in ring-array ultrasound computed tomography," in *Medical Imaging 2024: Ultrasonic Imaging and Tomography*, vol. 12932. SPIE, 2024, pp. 328–334.

[189] Y. Feng, Y. Chen, S. Feng, P. Jin, Z. Liu, and Y. Lin, "An intriguing property of geophysics inversion," in *The Thirty-ninth International Conference on Machine Learning (ICML)*, 2022.

[190] R. G. Pratt, "Seismic waveform inversion in the frequency domain, part 1: Theory and verification in a physical scale model," *Geophysics*, vol. 64, no. 3, pp. 888–901, 1999.

[191] M. Warner and L. Guasch, "Adaptive waveform inversion: Theory," *GEOPHYSICS*, vol. 81, no. 6, pp. R429–R445, 2016.

[192] Y. Yang, B. Engquist, J. Sun, and B. F. Hamfeldt, "Application of optimal transport and the quadratic wasserstein metric to full-waveform inversion," *Geophysics*, vol. 83, no. 1, pp. R43–R62, 2018.

[193] F. Yang and J. Ma, "Wasserstein distance-based full-waveform inversion with a regularizer powered by learned gradient," *IEEE Transactions on Geoscience and Remote Sensing*, vol. 61, pp. 1–13, 2023.

[194] W. Hu, Y. Jin, X. Wu, and J. Chen, "Progressive transfer learning for low-frequency data prediction in full-waveform inversion," *Geophysics*, vol. 86, pp. 1JA – X4, 2021.

[195] Y. Jin, W. Hu, S. Wang, Y. Zi, X. Wu, and J. Chen, "Efficient progressive transfer learning for full-waveform inversion with extrapolated low-frequency reflection seismic data," *IEEE Transactions on Geoscience and Remote Sensing*, vol. 80, 2021.

[196] H. Sun and L. Demanet, "Extrapolated full-waveform inversion with deep learning," *Geophysics*, vol. 85, pp. 1MJ – Z13, 2020.

[197] C. Bunks, F. Saleck, S. Zaleski, and G. Chavent, "Multiscale seismic waveform inversion," *Geophysics*, vol. 60, no. 5, pp. 1457–1473, 1995.

[198] C. Deng, Y. Feng, S. Feng, P. Jin, X. Zhang, Q. Zeng, and Y. Lin, "**OpenFWI**: Benchmark seismic datasets for machine learning-based full waveform inversion," in *Advances in Neural Information Processing Systems 35 (NeurIPS 2022) Datasets and Benchmarks Track*, 2022.

[199] S. Chakraborty, R. Tomsett, R. Raghavendra, D. Harborne, M. Alzantot, F. Cerutti, M. Srivastava, A. Preece, S. Julier, R. M. Rao, T. D. Kelley, D. Braines, M. Sensoy, C. J. Willis, and P. Gurram, "Interpretability of deep learning models: A survey of results," in *2017 IEEE SmartWorld, Ubiquitous Intelligence & Computing, Advanced & Trusted Computed, Scalable Computing & Communications, Cloud & Big Data Computing, Internet of People and Smart City Innovation*, 2017.

[200] X. Li, H. Xiong, X. Li, X. Wu, X. Zhang, J. Liu, J. Bian, and D. Dou, "Interpretable deep learning: Interpretation, interpretability, trustworthiness, and beyond," *arXiv preprint*, 2021.

[201] X. Zhang, V. A. Kelkar, J. Granstedt, H. Li, and M. A. Anastasio, "Impact of deep learning-based image super-resolution on binary signal detection," *Journal of Medical Imaging*, vol. 8, no. 6, pp. 065 501–065 501, 2021.

[202] K. Li, W. Zhou, H. Li, and M. A. Anastasio, "Assessing the impact of deep neural network-based image denoising on binary signal detection tasks," *IEEE transactions on medical imaging*, vol. 40, no. 9, pp. 2295–2305, 2021.

[203] K. Li, U. Villa, H. Li, and M. Anastasio, "Application of learned ideal observers for estimating task-based performance bounds for computed imaging systems," *Journal of Medical Imaging*, vol. 11, no. 2, p. 026002, 2024. [Online]. Available: https://doi.org/10.1117/1.JMI.11.2.026002

[204] H. H. Barrett, J. Yao, J. P. Rolland, and K. J. Myers, "Model observers for assessment of image quality." *Proceedings of the National Academy of Sciences*, vol. 90, no. 21, pp. 9758–9765, 1993.

[205] O. Christianson, J. J. Chen, Z. Yang, G. Saiprasad, A. Dima, J. J. Filliben, A. Peskin, C. Trimble, E. L. Siegel, and E. Samei, "An improved index of image quality for task-based performance of ct iterative reconstruction across three commercial implementations," *Radiology*, vol. 275, no. 3, pp. 725–734, 2015.

[206] J. Adler, S. Lunz, O. Verdier, C.-B. Schönlieb, and O. Öktem, "Task adapted reconstruction for inverse problems," *Inverse Problems*, vol. 38, no. 7, p. 075006, 2022.

[207] X. He and S. Park, "Model observers in medical imaging research," *Theranostics*, vol. 3, no. 10, p. 774, 2013.

[208] O. Agudo, "Acoustic full-waveform inversion in geophysical and medical imaging," Ph.D. dissertation, Imperial College London, 2018.

[209] M. Felice and Z. Fan, "Sizing of flaws using ultrasonic bulk wave testing: A review," *Ultrasonics*, vol. 88, pp. 26–42, 2018.

[210] G. Ongie, A. Jalal, C. Metzler, R. Baraniuk, A. Dimakis, and R. Willett, "Deep learning techniques for inverse problems in imaging," *IEEE Journal on Selected Areas in Information Theory*, vol. 1, pp. 39 – 56, 2020.

[211] A. Adler, M. Araya-Polo, and T. Poggio, "Deep learning for seismic inverse problems: Toward the acceleration of geophysical analysis workflows," *IEEE Signal Processing Magazine*, vol. 38, pp. 89–119, 2021.

[212] G. Wang, J. C. Ye, and B. De Man, "Deep learning for tomographic image reconstruction," *Nature Machine Intelligence*, vol. 2, pp. 737–748, 2020.

[213] J. Willard, X. Jia, S. Xu, M. Steinbach, and V. Kumar, "Integrating scientific knowledge with machine learning for engineering and environmental systems," *arXiv preprint*, 2020.

[214] G. Karniadakis, I. Kevrekidis, L. Lu, P. Perdikaris, S. Wang, and L. Yang, "Physics-informed machine learning," *Nature Reviews Physics*, vol. 3, pp. 422–440, 2021.

[215] S. Cuomo, V. Schiano Di Cola, F. Giampaolo, G. Rozza, M. Raissi, and F. Piccialli, "Scientific machine learning through physicsinformed neural networks: Where we are and whats next," *Journal of Scientific Computing*, vol. 92, 2022.

[216] C. Banerjee, K. Nguyen, C. Fookes, and G. Karniadakis, "Physics-informed computer vision: A review and perspectives," *arXiv preprint arXiv:2305.18035*, 2023.

[217] U. Kamilov, C. Bouman, G. Buzzard, and B. Wohlberg, "Plug-and-play methods for integrating physical and learned models in computational imaging: Theory, algorithms, and applications," *IEEE Signal Processing Magazine*, vol. 40, pp. 85–97, 2023.

[218] S. Operto, A. Gholami, H. Aghamiry, G. Guo, S. Beller, K. Aghazade, F. Mamfoumbi, L. Combe, and A. Ribodetti, "Extending the search space of full-waveform inversion beyond the single-scattering born approximation: A tutorial review," *GEOPHYSICS*, vol. 88, no. 6, pp. R671–R702, 2023.

[219] G. Schuster, Y. Chen, and S. Feng, "Review of physics-informed machine learning inversion of geophysical data," *Geophysics*, vol. 89, 2024.

[220] S. Feng, H. Wang, C. Deng, Y. Feng, Y. Liu, M. Zhu, P. Jin, Y. Chen, and Y. Lin, "$\mathbf{E}^{\mathbf{FWI}}$: Multi-parameter benchmark datasets for elastic full waveform inversion of geophysical properties," in *Advances in Neural Information Processing Systems 35 (NeurIPS 2022) Datasets and Benchmarks Track*, 2023.

[221] B. Verdin, G. Chevallier, and E. Ramasso, "ORION-AE: Multisensor acoustic emission datasets reflecting supervised untightening of bolts in a jointed vibrating structure," 2021. [Online]. Available: https://doi.org/10.7910/DVN/FBRDU0

[222] I. Virkkunen, T. Koskinen, O. Jessen-Juhler, and J. Rinta-Aho, "Augmented ultrasonic data for machine learning," 2019.

[223] M. Molero-Armenta, U. Iturrarán-Viveros, S. Aparicio, and M. Hernández, "Optimized opencl implementation of the elastodynamic finite integration technique for viscoelastic media," *Computer Physics Communications*, vol. 185, no. 10, pp. 2683–2696, 2014. [Online]. Available: https://www.sciencedirect.com/science/article/pii/S0010465514001702

[224] J. Salamon, C. Jacoby, and J. P. Bello, "A dataset and taxonomy for urban sound research," in *Proceedings of the 22nd ACM International Conference on Multimedia*, ser. MM '14, 2014, p. 10411044. [Online]. Available: https://doi.org/10.1145/2647868.2655045

[225] F. Li, U. Villa, N. Duric, and M. A. Anastasio, "A forward model incorporating elevation-focused transducer properties for 3d full-waveform inversion in ultrasound computed tomography," *IEEE Transactions on Ultrasonics, Ferroelectrics, and Frequency Control*, pp. 1–1, 2023.

[226] A. Badano, C. G. Graff, A. Badal, D. Sharma, R. Zeng, F. W. Samuelson, S. J. Glick, and K. J. Myers, "Evaluation of digital breast tomosynthesis as replacement of full-field digital mammography using an in silico imaging trial," *JAMA network open*, vol. 1, no. 7, pp. e185 474–e185 474, 2018.

[227] A. Badano, "In silico imaging clinical trials: cheaper, faster, better, safer, and more scalable," *Trials*, vol. 22, no. 1, pp. 1–7, 2021.

[228] A. C. of Radiology, C. J. D'Orsi *et al.*, *ACR BI-RADS Atlas: Breast Imaging Reporting and Data System; Mammography, Ultrasound, Magnetic Resonance Imaging, Follow-up and Outcome Monitoring, Data Dictionary*. ACR, American College of Radiology, 2013.

[229] F. Li, U. Villa, S. Park, and M. Anastasio, "3D Acoustic Numerical Breast Phantoms," 2021. [Online]. Available: https://doi.org/10.7910/DVN/KBYQQ7

[230] ——, "2D Acoustic Numerical Breast Phantoms and USCT Measurement Data," 2021. [Online]. Available: https://doi.org/10.7910/DVN/CUFVKE

[231] F. Li and U. Villa, "3D Numerical Breast Phantoms and Ring-Array USCT measurements (3 rings)," 2023. [Online]. Available: https://doi.org/10.7910/DVN/8JVLAE

[232] F. Li, U. Villa, S. Park, and M. Anastasio, "usct-breast-phantom: A python library to generate anatomically and physiologically realistic numerical breast phantoms for usct virtual imaging studies," 2021. [Online]. Available: https://doi.org/10.5281/zenodo.5173070

[233] Z. Zeng, Y. Zheng, H. Hu, Z. Dong, Y. Zheng, X. Liu, J. Wang, Z. Shi, L. Zhang, Y. Li, and H. Sun, "Openwaves: A large-scale anatomically realistic ultrasound-CT dataset for benchmarking neural wave equation solvers," 2025. [Online]. Available: https://openreview.net/forum?id=u14Y236LwX

[234] H. Wang, Y. Wu, Y. Feng, P. Jin, S. Feng, L. Zhang, J. Wiskin, B. Turkbey, P. A. Pinto, B. J. Wood, S. Luo, Y. Chen, E. Boctor, and Y. Lin, "Openpros: A large-scale dataset for limited view prostate ultrasound computed tomography," 2025. [Online]. Available: https://arxiv.org/abs/2505.12261

[235] H. Wang, J. Lin, X. Dong, S. Lu, Y. Li, and B. Yang, "Seismic velocity inversion transformer," *Geophysics*, vol. 88, no. 4, pp. R513–R533, 2023.

[236] V. Kazei, O. Ovcharenko, P. Plotnitskii, D. Peter, X. Zhang, and T. Alkhalifah, "Mapping full seismic waveforms to vertical velocity profiles by deep learning," *Geophysics*, vol. 86, no. 5, pp. R711–R721, 2021.

[237] B. Wu, D. Meng, and H. Zhao, "Semi-supervised learning for seismic impedance inversion using generative adversarial networks," *Remote Sensing*, vol. 13, no. 5, p. 909, 2021.

[238] W. Hu, Y. Jin, X. Wu, and J. Chen, "Physics-guided self-supervised learning for low frequency data prediction in fwi," in *SEG Technical Program Expanded Abstracts 2020*. Society of Exploration Geophysicists, 2020, pp. 875–879.

[239] Y. Wu, G. A. McMechan, and Y. Wang, "CNN-based gradient-free multiparameter reflection full-waveform inversion," in *First International Meeting for Applied Geoscience & Energy*. Society of Exploration Geophysicists, 2021, pp. 1369–1373.

[240] J. Vamaraju and M. K. Sen, "Unsupervised physics-based neural networks for seismic migration," *Interpretation*, vol. 7, no. 3, pp. SE189–SE200, 2019.

[241] S. Vedula, O. Senouf, A. M. Bronstein, O. V. Michailovich, and M. Zibulevsky, "Towards CT-quality ultrasound imaging using deep learning," *arXiv preprint*, 2017.

[242] M. Feigin, D. Freedman, and B. W. Anthony, "A deep learning framework for single-sided sound speed inversion in medical ultrasound," *IEEE Transactions on Biomedical Engineering*, vol. 67, no. 4, pp. 1142–1151, 2019.

[243] W. Zhao, H. Wang, H. Gemmeke, K. W. Van Dongen, T. Hopp, and J. Hesser, "Ultrasound transmission tomography image reconstruction with a fully convolutional neural network," *Physics in Medicine & Biology*, vol. 65, no. 23, p. 235021, 2020.

[244] J. Tong, M. Lin, X. Wang, J. Li, J. Ren, L. Liang, and Y. Liu, "Deep learning inversion with supervision: A rapid and cascaded imaging technique," *Ultrasonics*, vol. 122, p. 106686, 2022.

[245] Z. Liu, J. Wang, M. Ding, and M. Yuchi, "Deep learning ultrasound computed tomography with sparse transmissions," in *2021 IEEE International Ultrasonics Symposium (IUS)*. IEEE, 2021, pp. 1–4.

[246] J. Zhang, Q. He, C. Wang, H. Liao, and J. Luo, "A general framework for inverse problem solving using self-supervised deep learning: validations in ultrasound and photoacoustic image reconstruction," in *2021 IEEE International Ultrasonics Symposium (IUS)*. IEEE, 2021, pp. 1–4.

[247] J. Zhang, Q. He, Y. Xiao, H. Zheng, C. Wang, and J. Luo, "Self-supervised learning of a deep neural network for ultrafast ultrasound imaging as an inverse problem," in *2020 IEEE International Ultrasonics Symposium (IUS)*. IEEE, 2020, pp. 1–4.

[248] X. Dai, Y. Lei, T. Wang, M. Axente, D. Xu, P. Patel, A. B. Jani, W. J. Curran, T. Liu, and X. Yang, "Self-supervised learning for accelerated 3D high-resolution ultrasound imaging," *Medical Physics*, vol. 48, no. 7, pp. 3916–3926, 2021.

[249] X. Liu and M. Almekkawy, "Ultrasound computed tomography using physical-informed neural network," in *2021 IEEE International Ultrasonics Symposium (IUS)*. IEEE, 2021, pp. 1–4.

[250] Y. Fan, H. Wang, H. Gemmeke, T. Hopp, and J. Hesser, "Model-data-driven image reconstruction with neural networks for ultrasound computed tomography breast imaging," *Neurocomputing*, vol. 467, pp. 10–21, 2022.

[251] T. Lähivaara, L. Kärkkäinen, J. M. Huttunen, and J. S. Hesthaven, "Deep convolutional neural networks for estimating porous material parameters with ultrasound tomography," *The Journal of the Acoustical Society of America*, vol. 143, no. 2, pp. 1148–1158, 2018.

[252] X. Hong, L. Huang, S. Gong, and G. Xiao, "Shedding damage detection of metal underwater pipeline external anticorrosive coating by ultrasonic imaging based on HOG + SVM," *Journal of Marine Science and Engineering*, vol. 9(4), p. 364, 2021.

[253] N. Prakash, D. Nieberl, M. Mayer, and A. Schuster, "Learning defects from aircraft ndt data," *NDT & E International*, vol. 138, p. 102885, 2023.

[254] H. Song and Y. Yang, "Super-resolution visualization of subwavelength defects via deep learning-enhanced ultrasonic beamforming: A proof-of-principle study," *NDT & E International*, vol. 116, p. 102344, 2020.

[255] O. Siljama, T. Koskinen, O. Jessen-Juhler, and I. Virkkunen, "Automated flaw detection in multi-channel phased array ultrasonic data using machine learning," *Journal of Nondestructive Evaluation*, vol. 40, p. 67, 2021.

[256] D. Sen, A. Aghazadeh, A. Mousavi, S. Nagarajaiah, R. Baraniuk, and A. Dabak, "Data-driven semi-supervised and supervised learning algorithms for health monitoring of pipes," *Mechanical Systems and Signal Processing*, vol. 131, pp. 524–537, 2019.

[257] S. Jiang, R. He, G. Chen, Y. Zhu, J. Shi, K. Liu, and Y. Chang, "Semi-supervised health assessment of pipeline systems based on optical fiber monitoring," *Reliability Engineering & System Safety*, vol. 230, p. 108932, 2023.

[258] E. Bouzenad, Abd, M. Mountassir, S. Yaacoubi, F. Dahmene, M. Koabaz, B. Buchheit, and W. Ke, "A semi-supervised based k-means algorithm for optimal guided waves structural health monitoring: A case study," *Inventions*, vol. 4, p. 17, 2019.

[259] S. Akcay, A. Atapour-Abarghouei, and T. Breckon, "Ganomaly: Semi-supervised anomaly detection via adversarial training," *Asian Conference on Computer Vision*, pp. 622–637, 2018.

[260] K. Virupakshappa and E. Oruklu, "Unsupervised machine learning for ultrasonic flaw detection using gaussian mixture modeling, k-means clustering and mean shift clustering," *IEEE International Ultrasonics Symposium (IUS)*, vol. 91, pp. 647–649, 2019.

[261] I. Kraljevski, F. Duckhorn, M. Barth, C. Tschoepe, F. Schubert, and M. Wolff, "Autoencoder-based ultrasonic NDT of adhesive bonds," *2021 IEEE Sensors*, vol. 978, p. 4, 2021.

[262] B. Wang and J. Saniie, "Massive ultrasonic data compression using wavelet packet transformation optimized by convolutional autoencoders," *IEEE Transactions on Neural Networks and Learning Systems*, vol. 34, pp. 1395–1405, 2021.

[263] M. Rautela, J. Senthilnath, and E. Monaco, "Delamination prediction in composite panels using unsupervised-feature learning methods with wavelet-enhanced guided wave representations," *Compos. Struct*, vol. 291, p. 115579, 2022.

[264] S. Sawant, A. Sethi, S. Banerjee, and S. Tallur, "Unsupervised learning framework for temperature compensated damage identification and localization in ultrasonic guided wave shm with transfer learning," *Ultrasonics*, vol. 130, p. 106931, 2023.

TABLE IV
PAPER SUMMARY

Reference		Pure ML Methods				Hybrid Methods			
		Supervised	**Semi-Supervised**	**Self-Supervised**	**Unsupervised/ Unlabeled**	**Simulations/ Measurements-Driven**	**Physics Aware**	**Parameterized Solution**	**Plug & Play**
Seismic	Wu and Lin [51]	✓				✓			
	Araya-Polo et al. [1]	✓				✓			
	Renan et al. [58]	✓				✓			
	Wang et al. [235]	✓				✓			
	Kazei et al. [236]	✓				✓			
	Wu et al. [237]		✓				✓		
	Sun et al. [56]		✓				✓		
	Hu et al. [238]			✓			✓		
	Zhu et al. [92]				✓			✓	
	Saad et al. [62]				✓			✓	
	Wu et al. [239]			✓				✓	
	Fu et al. [110]				✓				✓
	Vamaraju et al. [240]				✓		✓		
	Rasht-Behesh et al. [84]				✓		✓		
	Izzatullah et al. [111]				✓				✓
	Zhang and Wang [95]				✓				✓
Medical Ultrasound	Lozenski et al. [9]	✓				✓			
	Vedula et al. [241]	✓				✓			
	Feigin et al. [242]	✓				✓			
	Zhao et al. [243]	✓				✓			
	Tong et al. [244]	✓				✓			
	Liu et al. [245]		✓				✓		
	Zhang et al. [246]			✓		✓			
	Zhang et al. [247]			✓		✓			
	Dai et al. [248]			✓			✓		
	Dai et al. [249]				✓		✓		
	Fan et al. [250]	✓						✓	
Acoustic/ Ultrasonic NDT	Lahivaara et al. [251]	✓				✓			
	Wang et al. [152]	✓				✓			
	Rao et al. [6]	✓				✓			
	Hong et al. [252]	✓				✓			
	Prakash et al. [253]	✓				✓			
	Song et al. [254]	✓				✓	✓	✓	
	Siljama et al. [255]	✓				✓	✓		
	Rudolph et al. [153]		✓			✓			
	Sen et al. [256]		✓			✓	✓	✓	
	Jiang et al. [257]		✓			✓			
	Bouzenad et al. [258]		✓			✓	✓		
	Akcay et al. [259]		✓			✓			
	Luiken et al. [155]			✓		✓	✓	✓	
	Shukla et al. [154]				✓	✓	✓	✓	
	Virupakshappa et al. [260]				✓	✓	✓		
	Kraljevski et al. [261]				✓	✓	✓		
	Wang et al. [262]				✓	✓	✓		
	Rautela et al. [263]				✓	✓	✓	✓	
	Sawant et al. [264]				✓	✓	✓		